The Dissertation Committee for Cari Michelle Anderson Certifies that this is the approved version of the following Dissertation:

Investigating Molecular Effects on Membrane Structure, Dynamics and Function

Committee:

Lauren J. Webb, Supervisor

Ron Elber

Carlos R. Baiz

Livia Schiavinato Eberlin

Vernita Gordon

Investigating Molecular Effects on Membrane Structure, Dynamics and Function

by

Cari Michelle Anderson

Dissertation

Presented to the Faculty of the Graduate School of

The University of Texas at Austin

in Partial Fulfillment

of the Requirements

for the Degree of

Doctor of Philosophy

The University of Texas at Austin

May 2019

Dedication

This is dedicated to my parents, Gary and Patty Anderson, for their unconditional love, encouragement and support in everything that I have accomplished in life. I am forever grateful for you both. Thank you both for everything. I love you Mom and Dad.

Acknowledgements

There are a number of people deserving of acknowledgements. First and foremost I would like to thank my advisor, Lauren J. Webb. Thank you for accepting me into the Webb Group in the fall of 2013 and for your constant guidance and support since. You have influenced the way that I view science and the true impact it has on the world. Thank you for constantly helping me to see the excitement of new findings, and constantly pushing me to think through problems completely. My graduate work would not be what it is, without the successful and insightful collaboration with Dr. Ron Elber, Alfredo Cardenas, and Arman Fathizadeh. It was an honor and pleasure to be able to work with you all on all of our projects.

I would like to thank the entire Webb Group for their constant support, insightful conversations and endless sharing of animal pictures to get through the tough days. I was lucky enough to join a group made up of fantastic individuals to work with. Elisa Novelli, thank you for being my friend and lab mate from day one. From our coffee breaks to margarita happy hours, this time in graduate school wouldn't have been the same without you. Thank you Whitney Fies for being not only a great lab mate, but also a great friend, and fellow dog lover. Jeremy First- thank you for the constant cynical humor and the reminder that life could always be worse; but really, thank you for good laughs, games of chess and your happy hour enthusiasm. Rebika Shrestha, thank you for introducing me to this research and teaching me everything you knew before you graduated. Working with you and learning from you brought me so much joy. I wouldn't be where I am today without your guidance at the very beginning.

My Ph.D. would not be possible without the love and support of my entire family. Mom and Dad, thank you for pushing me to be my very best in everything I do and

believing in me when I didn't believe in myself. Thank you for teaching me from a young age to persevere through each and every obstacle that I face and for instilling the confidence in me that I can achieve anything I set my mind to. A special thank you to my Dad- thank you for raising me a Longhorn, it has made my time here the University of Texas that much more special, Hook 'em! When it came time to move to Austin, it was much easier knowing that my siblings were all in Texas, very close by. In particular, my sister Casey; thank you for being my best friend and always ready to chat or simply to indulge in some needed (and always deserved) retail therapy. Eric and Holly, thank you for your encouragement and always being there whenever I needed. I love you both!

While in graduate school I was fortunate enough to meet Michael Azzaro who has provided me with unconditional love and encouragement. Thank you for being there during the highest highs and the lowest lows and always putting a smile on my face. Exploring Austin, cheering on the Longhorns and visiting all of the local breweries with you have been my favorite past time activities during graduate school. Thank you for always wanting to get out and have a good time with Rex and I!

Last, and certainly not least, a big thanks to my pup, Rex. Thank you for helping me make our very first apartment a true home here in Austin, reminding me of the good in the world, loving me unconditionally and for truly being the very best pup. There is no better way to end a long day in lab than coming home to a wagging tail and unconditional love. Thank you for reminding me to be patient, stay positive and to greet everyday with a smile and a nice stroll around the neighborhood. I will love you forever Rex.

Abstract

Investigating Molecular Effects on Membrane Structure, Dynamics and Function

Cari Michelle Anderson, PhD

The University of Texas at Austin, 2019

Supervisor: Lauren J. Webb

Biological membranes are heterogeneous structures with complex electrostatic profiles arising from lipids, sterols, membrane proteins, and water molecules. We investigated the effect of cholesterol and its derivative 6-ketocholestanol (6-kc) on membrane electrostatics by directly measuring the dipole electric field ($\vec{F}_d$) within lipid bilayers containing cholesterol or 6-kc at concentrations of 0−40 mol% through the vibrational Stark effect (VSE). We found that adding low concentrations of cholesterol, up to ~10 mol %, increases $\vec{F}_d$, while adding more cholesterol up to 40 mol% lowers $\vec{F}_d$. In contrast, we measured a monotonic increase in $\vec{F}_d$ as 6-kc concentration increased. We proposed that this membrane electric field is affected by multiple factors: the polarity of the sterol molecules, the reorientation of the phospholipid dipole due to sterol, and the impact of the sterol on hydrogen bonding with surface water. We used molecular dynamics simulations to examine the distribution of phospholipids, sterol, and helix in bilayers containing these sterols. At low concentrations, we observed clustering of sterols near the vibrational probe whereas at high concentrations, we observed spatial correlation between the positions of the sterol molecules. This work

demonstrated how a one-atom difference in a sterol changes the physicochemical and electric field properties of the bilayer.

Additionally, we set out to understand how a small molecule interacts with the lipid bilayer differently based on its charge. Our laboratory had previously reported that tryptophan permeated through a phosphatidylcholine lipid bilayer membrane at a faster rate when it was positively charged (Trp+) than when negatively charged (Trp−), which corresponded to a lower potential of mean force (PMF) barrier determined through simulations. In the work described here, we demonstrated that Trp+ partitions into the lipid bilayer membrane to a greater degree than Trp− by interacting with the ester linkage of a phosphatidylcholine lipid, where it is stabilized by the electron withdrawing glycerol functional group. These results are in agreement with tryptophan's known role as an anchor for transmembrane proteins, though the tendency for binding of a positively charged tryptophan is surprising. We discussed the implications of our results on the mechanisms of unassisted permeation and penetration of small molecules within and across lipid bilayer membranes based on molecular charge, shape, and molecular interactions within the bilayer structure.

Table of Contents

List of Tables

List of Figures

Chapter 1: Introduction

The cell membrane is vital for separating the cell from its environment, regulating input and exit of nutrients and waste, and providing a structure for cell adhesion and motility life, but it is one of the least understood parts of the cell due to its variety of functions and extreme molecular complexity. Lipids, sterols and membrane proteins, which spontaneously organize into structural scaffolds, are the main components of a cell membrane. This spontaneous organization is not random, but what is remarkable is that almost all of the interactions between these thousands of molecules are non-covalent and electrostatic in nature. These electrostatic interactions are the driving force between the structure and function of cell membranes.

In the work described in this dissertation, we have used experimental physical chemistry techniques paired with molecular dynamics simulations and calculations to investigate electrostatic interactions that play a role in both structure and function of lipid bilayer membranes. We have been particularly interested in understanding the role of molecular complexity in the structure, dynamics, and function of the lipid bilayer membrane. We have done this by starting with simple model vesicles, and systematically adding relevant molecular components to understand their effect on the membrane. After directly measuring the dipole field and characterizing the spontaneously formed structure that led to the observed field, we explored the most basic form of function of cell membranes: unassisted permeation of small molecules.

1.1 Membrane Dipole Field

The 2D structure of the lipid bilayer membrane, along with ordered water molecules at the lipid-water interface, organizes charge to create a system-wide electrostatic field that traverses the lipid bilayer. The electrostatic environment in a lipid

bilayer membrane can be broken down into three components: the transmembrane field, the surface field, and the dipole field (Figure 1.1). The transmembrane field, which arises from the difference in ion concentration on either side of the bilayer, has been well studied and understood to have a magnitude of 0.1-1 MV/cm in relevant physiological systems. The surface field, which is due to the potential difference between the membrane−water interface and the bulk aqueous region, is also well studied and known to be on the order of 0.01 MV/cm.[1-2] Lastly, the dipole field has been studied extensively with a variety of indirect measurements[3-5] and estimated to be on the order of 1-10 MV/cm.[1-2]

The dipole field arises from the arrangement of lipid dipole moments and water molecule dipole moments at the lipid-water interface. There are approximately 8-12 water molecules per lipid associated with the lipid bilayer. Due to the arrangement of all of these dipole moments, a large electrostatic field arises. Because of its magnitude, the dipole potential is believed to influence many aspects of membrane biological functions, such as ion-transport rates across lipid membranes;[6-10] membrane fusion;[11] redox reaction kinetics;[12] partitioning and translocation of small macromolecules, such as Na^+-K^+-ATPase and phospholipase A_2;[13-16] and insertion and folding of membrane peptides like mitochondrial amphipathic signal peptide p25 and simian immunodeficiency viral fusion peptide.[17]

Due to it being completely embedded in the interior of the aliphatic core of the lipid membrane, it has been a challenge to measure directly and accurately. Using methodology previously developed in our laboratory, we have extensively studied the membrane dipole field, which propagates from the interior of the lipid bilayer to the lipid head group-water interface, using vibrational Stark effect spectroscopy paired with molecular dynamics simulations.[18-19]

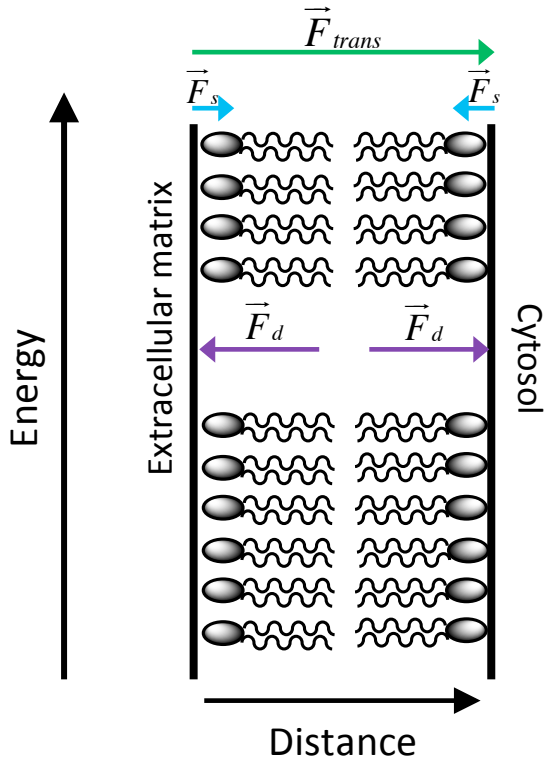

Figure 1.1: Diagram of the three components of the electrostatic field that traverses lipid membranes. The transmembrane field ($\vec{F}_{trans}$) traverses the length of the lipid bilayer. The surface field ($\vec{F}_s$) is located at the head group-water interface. The dipole field ($\vec{F}_d$) is embedded in the interior of the lipid bilayer extending from the center of the lipid bilayer to the head group-water interface.

1.2 Vibrational Stark Effect

Molecular vibrations are sensitive to the electric field around them. When a diatomic molecule, such as a nitrile, is excited its bond length increases due to its anharmonicity. If an external electric field is applied parallel or anti-parallel to the bond vector, therefore stabilizing or destabilizing the bond respectively, the energy required to for the transition from the ground vibrational to the excited vibrational state will change.

This phenomenon is known as the vibrational Stark effect (VSE) and given in equation 1-1.[20-21]

$$\Delta E = hc\Delta v_{obs} = -\Delta\vec{\mu} \cdot \vec{F} \qquad \text{(Equation 1-1)}$$

where ΔE is the change in absorption energy, h Plank's constant, c is the speed of light, Δv_{obs} is the change in vibrational frequency, $\Delta\vec{\mu}$ is the difference dipole moment and $\vec{F}$ is the external electric field. We can measure ΔE spectroscopically by obtaining the FTIR spectrum of the vibrational oscillator in the presence and absence of an electric field, $\vec{F}$. The difference dipole moment, $\Delta\vec{\mu}$, or Stark tuning rate, is a measure in the response of the oscillator to the applied electric field. A large Stark tuning rate means that the oscillator will exhibit a greater frequency shift in the presence of an electric field. For example, a Stark tuning rate of 1 cm^{-1} / (MV/cm) would mean that in the presence of a field of 1 MV/cm, the oscillator's absorption frequency would shift 1 cm^{-1}.

VSE spectroscopy has been used to describe the local electrostatic environment in biological systems, such as proteins[22] and nucleic acids and the Webb laboratory has used this tool and model membrane systems to directly probe the membrane dipole field. To apply VSE spectroscopy to membrane systems, the Webb laboratory previously designed a transmembrane peptide that traverses the length of a DMPC lipid bilayer, which contained one unnatural amino acid, *p*-cyanophenylalanine (*p*-CN-Phe).[18-19] *p*-CN-Phe contains a nitrile group on the phenylalanine side chain, which was used as the vibrational reporter of the local electrostatic environment. The location of the nitrile within the lipid bilayer was controlled by where *p*-CN-Phe was on the transmembrane peptide. A nitrile group was used as the local electrostatic probe because it has a large Stark tuning rate, is a relatively small oscillator resulting in very small, if any, perturbation to the biological system, and the nitrile vibration is in a clean area of the infrared spectrum.[23-24]

1.3 CELL PENETRATING PEPTIDES

Membranes are dynamic structures that act as barriers that selectively admit and exclude certain molecules based on the needs of the cell. Understanding the mechanism of unassisted small molecule transport across a lipid bilayer membrane in the absence of protein machinery that has evolved to transport particular atoms or molecules across the bilayer is particularly important for several reasons.

Cell penetrating peptides (CPPs) are a specific class of peptides that are typically composed of 10-30 amino acids and carry a large positive charge.[25-29] CPPs have the ability to interact with and penetrate through the lipid bilayer, and then drag across large cargo that is typically not able to penetrate through a cell membrane. CPPs can be a segment of a larger protein, for example the TAT peptide, which is a segment of the HIV virus[30] that is responsible for getting the membrane-insoluble protein into the cell, or exploited as a short peptide sequence attached to foreign material for drug delivery purposes.

To better understand the molecular level interactions that lead to cell penetration, we used our model vesicle system and the simplest form of a peptide: the single amino acid tryptophan. By changing the pH of the solution, we were able to control the charge of the molecule. The pK_a values for the C- and N-terminal ends of tryptophan are 2.8 and 9.3, respectively. Therefore, in a solution at pH 2.4 or 10.3, tryptophan will carry and positive or negative charge, respectively. We exploited this protonation and deprotonation of the amino acid to determine how only the charge of the molecule affects permeation, while not changing the chemical make up or structure of the molecule. Along with only changing the charge of the biologically relevant molecule, tryptophan was an ideal choice because of its fluorescent side chain.

1.4 TRYPTOPHAN FLUORESCENCE AND FLUORESCENCE QUENCHING

Tryptophan (Trp) is a naturally occurring amino acid with distinguishing spectroscopic character. The side chain on Trp is an indole ring, which is fluorescent in the UV region, making Trp easy to identify and quantify in solution using fluorescence spectroscopy. For this reason, it is commonly used as a natural fluorophore in biophysics.

The fluorescence emission energy of Trp is sensitive to its environment, which is a property that has been exploited in biological systems to determine the extent of hydration of its local environment.[31-33] When Trp is exposed to a hydrophobic environment such as the aliphatic core of a lipid bilayer or buried in the hydrophobic core of a protein, the fluorescence emission is blue-shifted (i.e. shorter wavelengths) due a destabilization of the excited state. In a hydrophilic environment, such as water, the increased reaction field from the high dielectric medium stabilizes Trp's excited state, decreasing the energy to the excited state transition, resulting in a red-shifted (i.e. longer wavelengths) emission spectrum. Normalized fluorescence emission spectra of Trp in hexanes, high purity water and buffers used for our experiments are shown in Figure 5.1 in Chapter 5.

Fluorescence quenching is a technique frequently used to determine the proximity of Trp to the center of the lipid bilayer. Bromine (Br) acts as a dynamic quencher that promotes intersystem crossing to a triplet state. Due to the slow emission from a triplet state, Trp's fluorescence is quenched when in close proximity to Br.[34] In previous studies, this property has been used to determine peptide and protein insertion depth within the membrane by changing the position of the Br along the fatty acid tail of the lipid and then measuring the extent of Trp fluorescence quenching based on its proximity to the Br.[35-37] Incorporating brominated lipids (Br-PC) into our lipid bilayer vesicles in small concentrations (about 10-30 mol%), we can determine the depth at which Trp partitions

within the lipid bilayer. Comparing the fluorescence emission spectra of Trp in lipid vesicles with and without Br-PC lipids, and determining the amount of fluorescence that is quenched at various depths, we can determine the spot at which Trp is located.

1.5 Outline of the Dissertation

The following chapters in this dissertation will report the work that we have done using small unilamellar vesicles as a model system for membranes to investigate the structure, function and dynamics briefly introduced. An overall theme is to understand the interactions that lead to the observed structure and function of a membrane at a molecular level. Chapter 2 thoroughly describes the materials and methods for creating our model system and characterizing it. In Chapter 3, the argument for using vesicles as a model system and a new electrochemical characterization technique is described in detail. The results show that we can use electrochemistry to determine the size of vesicles in solution and then determine the concentration of lipid vesicles by encapsulating an electrochemically active species. Chapter 4 details how the sterols cholesterol and 6-ketocholestanol affect the dipole field and the 2D membrane structure differently. In Chapter 5 we look at the dynamics of the lipid bilayer and determine how the charge of a single amino acid, Trp, affects the rate and extent of partitioning in a phosphatidylcholine lipid bilayer. Finally in Chapter 6, we report how the arrangement of the head group dipole altered the degree of partitioning of charged tryptophan in the lipid bilayer.

1.6 References

1. Cevc, G. Membrane Electrostatics. *Biochim. Biophys. Acta, Rev. Biomembr.* **1990,** *1031*, 311-382.

2. Honig, B. H.; Hubbell, W. L.; Flewelling, R. F. Electrostatic Interactions in Membranes and Proteins. *Annu. Rev. of Biophys. Biophys. Chem.* **1986,** *15*, 163-193.

3. Efimova, S. S.; Ostroumova, O. S. Effect of Dipole Modifiers on the Magnitude of the Dipole Potential of Sterol-Containing Bilayers. *Langmuir* **2012,** *28*, 9908-9914.

4. Haldar, S.; Kanaparthi, R. K.; Samanta, A.; Chattopadhyay, A. Differential Effect of Cholesterol and its Biosynthetic Precursors on Membrane Dipole Potential. *Biophys. J.* **2012,** *102*, 1561-1569.

5. Starke-Peterkovic, T.; Turner, N.; Vitha, M. F.; Waller, M. P.; Hibbs, D. E.; Clarke, R. J. Cholesterol Effect on the Dipole Potential of Lipid Membranes. *Biophys. J.* **2006,** *90*, 4060-70.

6. Schamberger, J.; Clarke, R. J., Hydrophobic Ion Hydration and the Magnitude of the Dipole Potential. *Biophys. J.* **2002,** *82*, 3081-3088.

7. Duffin, R. L.; Garrett, M. P.; Busath, D. D. Modulation of Lipid Bilayer Interfacial Dipole Potential by Phloretin, RH421, and 6-Ketocholestanol as Probed by Gramicidin Channel Conductance. *Langmuir* **2003,** *19*, 3561-3561.

8. Phillips, L. R.; Cole, C. D.; Hendershot, R. J.; Cotten, M.; Cross, T. A.; Busath, D. D. Noncontact Dipole Effects on Channel Permeation. III. Anomalous Proton Conductance Effects in Gramicidin. *Biophys. J.* **1999,** *77*, 2492-2501.

9. Hladky, S. B. The Energy Barriers to Ion Transport by Nonactin Across Thin Lipid Membranes. *Biochim. Biophys. Acta, Biomembr.* **1974,** *352*, 71-85.

10. Bala, S.; Kombrabail, M. H.; Prabhananda, B. S. Effect of Phloretin on Ionophore Mediated Electroneutral Transmembrane Translocations of H+, K+ and Na+ in Phospholipid Vesicles. *Biochim. Biophys. Acta, Biomembr.* **2001,** *1510*, 258-269.

11. Cladera, J.; Martin, I.; Ruysschaert, J.-M.; O'Shea, P. Characterization of the Sequence of Interactions of the Fusion Domain of the Simian Immunodeficiency Virus with Membranes: Role of the Membrane Dipole Potential. *J. Biol. Chem.* **1999,** *274*, 29951-29959.

12. Alakoskela, J. I.; Kinnunen, P. K. Control of a Redox Reaction on Lipid Bilayer Surfaces by Membrane Dipole Potential. *Biophys. J.* **2001,** *80*, 294-304.

13. Maggio, B. Modulation of Phospholipase A2 by Electrostatic Fields and Dipole Potential of Glycosphingolipids in Monolayers. *J. Lipid Res.* **1999,** *40*, 930-939.

14. Alakoskela, J.-M. I.; Söderlund, T.; Holopainen, J. M.; Kinnunen, P. K. J. Dipole Potential and Head-Group Spacing Are Determinants for the Membrane Partitioning of Pregnanolone. *Mol. Pharmacol.* **2004,** *66*, 161-168.

15. Cladera, J.; O'Shea, P. Intramembrane Molecular Dipoles Affect the Membrane Insertion and Folding of a Model Amphiphilic Peptide. *Biophys. J.* **1998,** *74*, 2434-2442.

16. Starke-Peterkovic, T.; Turner, N.; Else, P. L.; Clarke, R. J. Electric Field Strength of Membrane Lipids from Vertebrate Species: Membrane Lipid Composition and Na+-K+-ATPase Molecular Activity. *Am. J. of Physiol. Regul. Integr. Comp. Physiol.* **2005,** *288*, R663-R670.

17. Buzón, V.; Cladera, J. Effect of Cholesterol on the Interaction of the HIV GP41 Fusion Peptide with Model Membranes. Importance of the Membrane Dipole Potential. *Biochemistry* **2006,** *45*, 15768-15775.

18. Shrestha, R.; Cardenas, A. E.; Elber, R.; Webb, L. J. Measurement of the Membrane Dipole Electric Field in DMPC Vesicles Using Vibrational Shifts of p-Cyanophenylalanine and Molecular Dynamics Simulations. *J. Phys. Chem. B* **2015,** *119*, 2869-2876.

19. Hu, W.; Webb, L. J. Direct Measurement of the Membrane Dipole Field in Bicelles Using Vibrational Stark Effect Spectroscopy. *J. Phys. Chem. Lett.* **2011,** *2*, 1925-1930.

20. Fried, S. D.; Boxer, S. G. Measuring Electric Fields and Noncovalent Interactions Using the Vibrational Stark Effect. *Acc. Chem. Res.* **2015,** *48*, 998-1006.

21. Chattopadhyay, A.; Boxer, S. G. Vibrational Stark Effect Spectroscopy. *J. Am. Chem. Soc.* **1995,** *117*, 1449-1450.

22. Park, E. S.; Andrews, S. S.; Hu, R. B.; Boxer, S. G. Vibrational Stark Spectroscopy in Proteins: A Probe and Calibration for Electrostatic Fields. *J. Phys. Chem. B* **1999,** *103*, 9813-9817.

23. Andrews, S. S.; Boxer, S. G. Vibrational Stark Effects of Nitriles I. Methods and Experimental Results. *J. Phys. Chem. A* **2000,** *104*, 11853-11863.

24. Andrews, S. S.; Boxer, S. G. Vibrational Stark Effects of Nitriles II. Physical Origins of Stark Effects from Experiment and Perturbation Models. *J. Phys. Chem. A* **2002,** *106*, 469-477.

25. Yesylevskyy, S.; Marrink, S.-J.; Mark, A. E. Alternative Mechanisms for the Interaction of the Cell-Penetrating Peptides Penetratin and the TAT Peptide with Lipid Bilayers. *Biophys. J.* **2009,** *97*, 40-49.

26. Vivès, E.; Schmidt, J.; Pèlegrin, A. Cell-penetrating and Cell-Targeting Peptides in Drug Delivery. *Biochim. Biophys. Acta, Rev. Cancer* **2008,** *1786*, 126-138.

27. Huang, K.; García, Angel E. Free Energy of Translocating an Arginine-Rich Cell-Penetrating Peptide across a Lipid Bilayer Suggests Pore Formation. *Biophys. J.* **2013,** *104*, 412-420.

28. Herce, H. D.; Garcia, A. E.; Litt, J.; Kane, R. S.; Martin, P.; Enrique, N.; Rebolledo, A.; Milesi, V. Arginine-Rich Peptides Destabilize the Plasma Membrane,

Consistent with a Pore Formation Translocation Mechanism of Cell-Penetrating Peptides. *Biophys. J.* **2009,** *97*, 1917-1925.

29. Herce, H. D.; Garcia, A. E. Cell Penetrating Peptides: How Do They Do It? *J. Biol. Phys.* **2007,** *33*, 345-356.

30. Ciobanasu, C.; Siebrasse, J. P.; Kubitscheck, U. Cell-Penetrating HIV1 TAT Peptides Can Generate Pores in Model Membranes. *Biophys. J.* **2010,** *99*, 153-162.

31. Vivian, J. T.; Callis, P. R. Mechanisms of Tryptophan Fluorescence Shifts in Proteins. *Biophys. J.* **2001,** *80*, 2093-2109.

32. Gable, J. E.; Schlamadinger, D. E.; Cogen, A. L.; Gallo, R. L.; Kim, J. E. Fluorescence and UV Resonance Raman Study of Peptide-Vesicle Interactions of Human Cathelicidin LL-37 and its F6W and F17W Mutants. *Biochemistry* **2009,** *48*, 11264-11272.

33. Lakowicz, J. R. *Principles of Fluorescence Spectroscopy*; Springer: New York, 2006; pp 205-235.

34. Lakowicz, J. R. *Principles of Fluorescence Spectroscopy*; Springer: New York, 2006; pp 331-351.

35. Pfefferkorn, C. M.; Walker, R. L.; He, Y.; Gruschus, J. M.; Lee, J. C. Tryptophan Probes Reveal Residue-Specific Phospholipid Interactions of Apolipoprotein C-III. *Biochim. Biophys. Acta, Biomembr.* **2015,** *1848*, 2821-2828.

36. Soni, Smita P.; Adu-Gyamfi, E.; Yong, Sylvia S.; Jee, Clara S.; Stahelin, Robert V. The Ebola Virus Matrix Protein Deeply Penetrates the Plasma Membrane: An Important Step in Viral Egress. *Biophys. J.* **2013,** *104*, 1940-1949.

37. Mishra, V. K.; Palgunachari, M. N. Interaction of Model Class A1, Class A2, and Class Y Amphipathic Helical Peptides with Membranes. *Biochemistry* **1996,** *35*, 11210-11220.

Chapter 2: Materials and Methods

2.1 Publication Note

Portions of the methods outlined in this section were adapted from the following publications:

1. Lebegue, E.; **Anderson, C. M.**; Dick, J. E.; Webb, L. J.; Bard, A. Electrochemical Detection of Single Phospholipid Vesicle Collisions at a Pt Ultramicroelectrode. *Langmuir* **2015,** *31*, 11734-11739.

2. Shrestha, R.; **Anderson, C. M.**; Cardenas, A. E.; Elber, R.; Webb, L. J. Direct Measurement of the Effect of Cholesterol and 6-Ketocholestanol on Membrane Dipole Field Using Vibrational Stark Effect Spectroscopy Coupled with Molecular Dynamics Simulations. *J. Phys. Chem. B* **2017,** *121,* 3424-3436.

3. **Anderson, C. M.**; Cardenas, A. E.; Elber, R.; Webb, L. J. Preferential Equilibrium Partitioning of Positively Charged Tryptophan into Phosphocholine Bilayer Membranes. *J. Phys. Chem. B* **2019,** *123,* 170-179.

4. Cardenas, A. E.; **Anderson, C. M.**; Elber, R.; Webb, L. J. Partition of Positively and Negatively Charged Tryptophan Ions in Membranes with Inverted Phospholipid Heads: Simulations and Experiments. *J. Phys. Chem. B* **2019,** *123,* 3272-3281.

2.2 Materials

1,2-dimyristoyl-sn-glycero-3-phosphocholine (DMPC), 1,2-dioleoyl-sn-glycero-3-phosphocholine (DOPC) dissolved in chloroform, 2-((2,3-bis(oleoyloxy)propyl)dimethylammonio)ethyl ethyl phosphate (DOCPe) dissolved in chloroform and 1-palmitoyl-2-stearoyl(4,5)dibromo-sn-glycero-3-phosphocholine (Br-

PC) dissolved in chloroform were purchased from Avanti Polar Lipids, Inc. (Alabaster, AL) and used without further purification. Cholesterol and 6-ketocholestanol (6-kc) were purchased from Sigma-Aldrich (St. Louis, MO) and used without further purification.

L-Tryptophan, sodium bicarbonate ($NaHCO_3$), sodium carbonate anhydrous (Na_2CO_3) and Hepes were purchased from Sigma-Aldrich (St. Louis, MO). Sodium azide (NaN_3), citric acid monohydrate, and anhydrous sodium phosphate (Na_2HPO_4) were purchased from Fisher Scientific (Waltham, MA). All buffers were prepared using HPLC grade water purchased from Fisher Scientific (Waltham, MA). PD-10 desalting columns were purchased from GE Healthcare (Chicago, IL) and used according to the manufacturer's instructions.

When working with positively or negatively charged tryptophan, the charge of tryptophan was controlled by the pH of solution. For samples with Trp+, a buffer composed of 0.1 M citric acid and 0.1 M Na2HPO4 with 0.02% (w/v) NaN3 at pH 2.4 was used. For samples with Trp−, a buffer composed of 0.1 M NaHCO3 and 0.1 M Na2CO3 with 0.02% (w/v) NaN3 at pH 10.3 was used.

2.3 VESICLE PREPARATION

Small unilamellar vesicles (SUVs) were our model membrane system for all of the experimental work. A more detailed description of our model system is discussed in the next chapter. To create the SUVs for all of our experiments, we used two different vesicle preparation methods depending on the composition of the lipid vesicles. These two methods are described below.

Depending on the set of experiments, one of three different buffers was used for the lipid vesicle suspension. The three buffers prepared were a 0.1 M citric acid buffer (pH 2.4), 10 mM Hepes buffer (pH 7.2) and 0.1 M sodium carbonate/sodium bicarbonate

buffer (pH 10.3). All of the buffers were prepared with 0.02% (w/v) NaN_3 and HPLC grade water.

2.3.1 Sonication Method

Small unilamellar vesicles (SUVs) that contained the peptide with the nitrile probe and cholesterol or 6-ketocholestanol were prepared using the sonication method. For samples containing cholesterol, about 30 mg of DMPC powder and a correct amount of cholesterol powder and lyophilized peptide (determined as described below) were taken together in a vial and dissolved in approximately 1 mL of chloroform. For samples containing 6-kc, a stock solution of 6-kc in methanol was made, from which the correct volume was added to the lipid and peptide solution in chloroform. The sample was then vortexed for 5 min, dried under vacuum for 2 h, and then transferred into a N_2(g)-purged glove box overnight. The dried sample was then hydrated with the desired buffer, maintained at a temperature above the gel−liquid crystal transition temperature (T_m) of DMPC. This was vortex mixed for 5 min to get a homogeneous distribution of multilamellar vesicles. Small unilamellar vesicles were obtained by placing the multilamellar vesicle suspension in a sonication bath maintained at 35 °C until the milky solution (indicative of multilamellar vesicles) cleared to slightly cloudy (indicative of light scattering by residual large particles remaining in the lipid suspension). These residuals were removed by centrifugation at 12000 × g for approximately 60 min to achieve a clear vesicle solution. All samples were stored at a temperature above T_m and were stable for up to 5 days.

Sterols were added at concentrations of 0, 5, 10, 15, 20, 30, and 40 mol% and peptides were added at a concentration of 1 mM. On average, in a homogeneous distribution of 1 mM peptide results in a ratio of 33 peptides per 1000 lipids.

2.3.2 Extrusion Method

Vesicles that were used for permeation and partitioning experiments were formed using the extrusion method outlined here. Lipid films were prepared by drying appropriate aliquots of DOPC or the lipid(s) of choice in chloroform under vacuum overnight. Lipid films that were not used immediately were stored in an air-free, N_2-purged glove box for up to 1 week. Lipid films were hydrated with the appropriate amount of desired buffer to make 30 mM lipid solutions. Hydrated lipid films were vortexed for 5 min, put through a freeze-thaw cycle consisting of being immersed in a liquid nitrogen bath followed by being placed in a 40 °C water bath 12 times, and then passed through 100 nm pore polycarbonate membranes 12 times. The vesicle solutions were stored in a 25 °C water bath until used for experiments.

2.4 Characterization of Vesicles

All of our vesicle samples were rigorously characterized to determine the average size or diameter, lamellarity and shape of the vesicles. We used dynamic light scattering (DLS), ^{31}P NMR and atomic force microscopy (AFM) to characterize all vesicles. These techniques are described in detail below.

2.4.1 Dynamic Light Scattering (DLS)

The vesicle size distribution of each batch was determined using dynamic light scattering on a Malvern Zetasizer Nano ZS instrument equipped with He−Ne light source (633 nm) and photodiode detector. The vesicle size measurements were made at a temperature of 30 °C with a solution viscosity of 0.8872 cP and refractive index of 1.330.

2.4.2 ^{31}P NMR

The splitting and shifting of ^{31}P NMR spectra were used to characterize vesicles as unilamellar.[1-2] Samples for NMR spectroscopy were prepared by adding 150 μL of D_2O to 550 μL of vesicle sample in an NMR tube. ^{31}P NMR spectra were obtained at 35 °C with 202.343 MHz on a Varian INOVA-500 NMR. After collection of the ^{31}P NMR spectrum, approximately 2.4 mg of $PrCl_3 \bullet 6H_2O$ was added to the NMR tube containing the sample. Another ^{31}P NMR spectrum was obtained with the addition of $PrCl_3 \bullet 6H_2O$. The spectra were processed using Mestranova software.

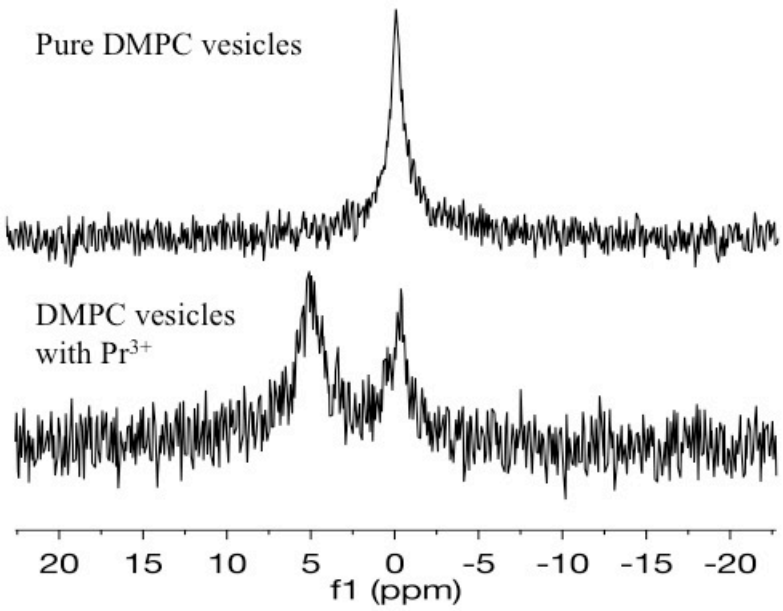

Figure 2.1: ^{31}P NMR spectra of small unilamellar vesicles composed of DMPC lipids. Top: Spectrum of phospholipid vesicles; Bottom: Spectrum of the same phospholipid vesicles after the addition of Pr^{3+} in the form of $PrCl_3 \bullet 6H_2O$

The two spectra, one without and one with $PrCl_3 \bullet 6H_2O$, were compared to determine the lamellarity of the vesicles. Representative spectra are shown in Figure 2.1 from DMPC unilamellar vesicles. 85% phosphoric acid was used as the standard to which

chemical shifts were referenced. A "wide-line" or powder-line shape due to the restricted anisotropic motion is indicative of multilamellar vesicles whereas a single well-resolved peak at about 0.1 ppm is representative of unilamellar vesicles. The ^{31}P NMR spectrum in Figure 2.1 on the top is indicative unilamellar vesicles. In Figure 2.1 on the bottom we show the ^{31}P NMR spectrum of DMPC SUVs after the addition of Pr^{3+} in the form of $PrCl_3 \bullet 6H_2O$. The peak splitting and downfield shifting of the second peak is due to the negatively charged phosphates on phospholipids in the outer layer interacting and bonding with Pr^{3+}. Typically, pure lipid bilayers are impermeable to lanthanide cations, hence Pr^{3+} only shifts the signal from the outer leaflet downfield, splitting the single narrow peak into two, where the peak from the phospholipids in the inner leaflet remains unchanged.

2.4.3 Atomic Force Microscopy (AFM)

Atomic force microscopy (AFM) was used to confirm vesicles remained spherical with a homogeneous size distribution regardless of the buffer. 5 μL of vesicle sample was deposited onto freshly cleaved mica and allowed to dry for an hour. AFM images were taken with an Asylum MFP-3D Stand Alone AFM operating in tapping-mode. General purpose, n-type silicon cantilevers with spring constant of 40 N m^{-1} and a resonance frequency of 325 kHz were used. Images were processed to remove noise along the fast-scan direction and flattened using Gwddyion software.

2.5 REFERENCES

1. Bystrov, V. F. S., Y. E.; Viktorov, A. V.; Barsukov, L. I.; Bergelson, L. D. 31P-NMR Signals From Inner and Outer Surfaces of Phospholipid Membranes. *FEBS Lett.* **1972,** *25*, 337-338.

2. Fröhlich, M.; Brecht, V.; Peschka-Süss, R. Parameters Influencing the Determination of Liposome Lamellarity by 31P-NMR. *Chem. Phys. Lipids* **2001,** *109*, 103-112.

Chapter 3: Electrochemical Detection of Vesicle Size and Concentration

3.1 Publication Note

Portions of the methods outlined in this section were adapted from the following publication:

Lebegue, E.; **Anderson, C. M.**; Dick, J. E.; Webb, L. J.; Bard, A. Electrochemical Detection of Single Phospholipid Vesicle Collisions at a Pt Ultramicroelectrode. *Langmuir* **2015,** *31*, 11734-11739. [C. M. Anderson created all of the lipid vesicle systems and characterized them with dynamic light scattering (DLS). E. Lebegue did all of the electrochemistry design and experiments.]

3.2 Introduction

Electrochemical detection of discrete soft nanoparticle collisions on ultramicroelectrodes (UMEs) has been recently reported as a method to determine the size distribution and the concentration of emulsion droplets,[1-5] vesicles,[6-7] viruses,[8] micelles,[9] and biological macromolecules.[10] The observation of these stochastic events can potentially provide information on various single nanoparticles contrary to ensemble measurements.** Especially, electrochemical detection by collisions has been extended to studying vesicles by oxidizing the contents released upon collision at a carbon UME.[6-7] There is, however, lack of agreement about the membrane opening mechanism followed by the content electrolysis on the carbon UME. Compton and co-workers proposed a "full collapse fusion" mechanism of the liposome membrane during the collision, based on the complete release and oxidation of ascorbic acid in a commercial vitamin C preparation, on a carbon UME.6 In contrast, Ewing and co-workers proposed a mechanism where the vesicle first adsorbs to the electrode surface and spreads out over the electrode, and finally the oxidation of the catecholamine content occurs.[7] Moreover, this process is

supported by previous investigations from Kasemo and co-workers about vesicles adsorption on various substrates (silicon dioxide, thiolated gold, oxidized gold) where the authors reported a rupture of vesicles adsorbed on hydrophobic surfaces (thiolated gold) and, by opposition, an adsorption of intact vesicles on more hydrophilic surfaces (oxidized gold).[11-12] In the same trend, Scholz and co-workers studied the behavior of different liposomes on the electrode surface (mainly a mercury electrode) and showed that chronoamperometric measurements are an interesting tool to probe the membrane stability and to understand the effect of its properties on vesicle fusion.[13-16] In particular, the authors were the first to study the adhesion and bursting processes of 450 nm diameter liposomes and the spreading of the lecithin on the mercury surface (0.48 mm^2) by using chronoamperometric measurements for determining the frequency of spikes and the charge densities of formed monolayers.[13-15]

To improve our understanding of vesicle interactions with an electrode surface, we herein present different vesicle behavior on a Pt UME, which serves as a hydrophilic surface for vesicle collisions. By analogy with emulsion results,[1-4] we report two techniques of vesicle detection: (1) vesicle blocking (VB), which consists of observing a blocking of solution redox species due to the single vesicle adsorption on the UME, and (2) vesicle reactor (VR), where the redox probe is encapsulated inside the vesicle and can be electrolyzed at the UME after its collision (Figure 3.1). In both cases, the redox probe chosen was potassium ferrocyanide [$K_4Fe(CN)_6$][17] because of its high solubility in water (0.5 M). Moreover, 0.5 M $K_4Fe(CN)_6$ can be easily encapsulated inside vesicles as a hydrophilic content and removed from the solution outside vesicles. Also, it is a relevant redox species for the continuous phase largely used for detection of various soft nanoparticle collisions by the blocking method.[1, 8, 10]

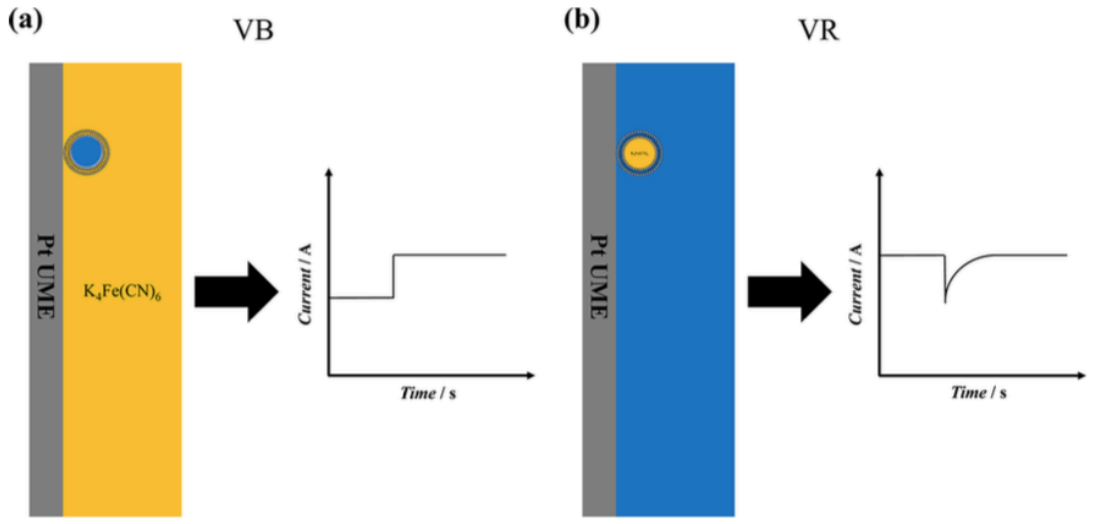

Figure 3.1: Schematic representation of the two reported vesicle collision techniques at a Pt UME where the potential applied is at +0.6 V *vs* Ag/AgCl, and the oxidation currents are plotted in the negative direction (a) Electrochemical oxidation of $Fe(CN)_6^{4-}$ in aqueous solution (negative current) is partially blocked by single vesicle blocking (VB) which produces an anodic current step. (b) Electrochemical oxidation of $Fe(CN)_6^{4-}$ encapsulated inside the vesicle reactor (VR) gives an anodic current spike.

Here we demonstrate that the BLM does not break and release the contents during vesicle collision at the Pt UME hydrophilic surface. As shown in previous studies of BLMs,[18-19] they do not allow effective electron tunneling or ion transport to cause redox reactions across them without the presence of a strong surfactant. However, cell transfection experiments show that the presence of a surfactant, such as Triton X-100 (TX100), can promote transfer across the membrane.[17, 20] Moreover, we clearly show that vesicles are adsorbed on the Pt surface (VB) after their collision, but the electron transfer cannot happen through the bilayer for electrolyzing the $Fe(CN)_6^{4-}$ content (VR). Hence, we discuss here the TX100 concentration effect in solution and also the corresponding kinetic study on the vesicle membrane permeability by detection of electrochemical collision events. Our results were in good agreement with several studies reporting the

role of TX100 surfactant on the cell membrane, which could yield fundamental insight into the transfection process.[20-24]

3.3 METHODS

30 mM DMPC lipid vesicles were prepared in either 2 mL of pure water or 2 mL of 0.5 M $K_4Fe(CN)_6$ aqueous solution, using the extrusion method described in Section 2.3.2. The final step was to pass the DMPC vesicle solution through a PD-10 desalting column with pure water to remove $K_4Fe(CN)_6$ from the bulk solution. All vesicle samples were characterized using dynamic light scattering (DLS) as described in Section 2.4.1.

3.3.1 Electrochemistry Experimental Instrumentation and Methods

The electrochemical experiments were performed using a CHI model 920C and CHI630 potentiostat (CH Instruments, Austin, TX) with a three-electrode cell placed in a faraday cage. Platinum wire was used as a counter electrode, and the reference electrode was Ag/AgCl. For all chronoamperometric i−t curves recorded, the sample interval (in sampling time) was 50 ms. Along with DLS data, nanoparticle tracking analysis (NTA) data was obtained by Nanosight. However, NTA data collection was discontinued when we found fouling of the cell window. The size distribution of vesicles was analyzed by DLS and NTA, both in agreement with 120 ± 30 nm diameter DMPC vesicles in aqueous solutions.

Platinum ultramicroelectrodes were prepared by laser pulling (Sutter Instruments) according to the general procedure performed in the Bard laboratory,[25-26] followed by mechanical polishing with Bevellers for a diameter between 1 and 2 μm. Before each experiment, the Pt UMEs were washed by dipping in piranha solution (mixture composed to 3:1 concentrated sulfuric acid to 30% hydrogen peroxide solution) for 10 s, then

dipping in water, and finally dipping successively in acetone, ethanol, and several times in water. The radius of the Pt UME was obtained using the steady-state current in cyclic voltammetry recorded in 1 mM ferrocenemethanol aqueous solution.

3.4 Evaluating Vesicle Concentration Using Vesicle Blocking Method

The electrochemical detection of collisions by the VB method is presented in Figure 3.2. The potential applied at 0.6 V corresponding to the steady-state current of the $Fe(CN)_6^{4-}$ oxidation into $Fe(CN)_6^{3-}$ at a 1.7 μm Pt UME was previously determined by cyclic voltammetry. During the chronoamperometry measurement at 0.6 V in 0.2 M $K_4Fe(CN)_6$ in the absence of DMPC vesicles, a steady-state current was reached at the Pt UME, and no current step was observed over 300 s. In contrast, after addition of DMPC vesicles encapsulating only pure water (no electroactive species), several current steps were observed due to single vesicle collisions onto the Pt UME surface, which locally block the flux of $Fe(CN)_6^{4-}$ to the electrode surface.

The experimentally observed frequency of current steps at the Pt UME with the VB method was 0.12 Hz. The vesicles concentration (C_{ves}) can be calculated from this collision frequency of vesicles onto the UME surface by equation 3-1, based on a diffusion-limited flux of nanoparticles to the electrode surface.[27] The concentration of the pure DMPC vesicles aqueous solution before dilution is evaluated as 5.5 ± 0.2 nM, a value in good agreement with the concentration determined by NTA at 3.1 ± 0.2 nM, suggesting that diffusion is the dominant process compared with migration effects.[28] A small contribution of mass transfer of the vesicles to the electrode surface by electrophoretic migration cannot be ruled out; however, because the concentration of potassium ferrocyanide is 0.2 M, it likely carries most of the current, making diffusion the predominate form of mass transfer.[8]

$$C_{ves} = \frac{f_{ves}}{4D_{ves}r_e N_A} \qquad \text{(Equation 3-1)}$$

where f_{ves} is the collision frequency by diffusion of the vesicles to the UME, D_{ves} is the diffusion coefficient of a spherical vesicle, r_e is the radius of the working electrode, and N_A is Avogadro's number. The diffusion coefficient (D_{ves}) can be estimated by the Stokes-Einstein relation (equation 3-2)[29]

$$D_{ves} = \frac{k_B T}{6\pi\eta r_{ves}} \qquad \text{(Equation 3-2)}$$

where k_B is Boltzmann's constant, T is temperature, η is the viscosity of the continuous phase at 25 °C and r_{ves} is the hydrodynamic radius of a vesicle. From the equation, the diffusion coefficient of a 113 nm diameter vesicle (determined by DLS) is 4.3 x 10^{-8} cm^2 s^{-1}, matching well with the value estimated from NTA data at 4.1 x 10^{-8} cm^2 s^{-1}.

The current steps shown in Figure 3.2 are related to the single vesicle collisions at the Pt UME surface. In most cases, we observed a current decrease in the shape of a stair step, indicating that most of the vesicles stick on the Pt surface after collision and only in rare cases they quickly leave the UME after collision, showing a current increase in the shape of a stair step. Because of these observations, we assume that the probability of the adsorbate sticking to the electrode is nearly 1. Therefore, the VB electrochemical method is a relevant technique to detect nanometer-sized vesicles at a Pt UME and can give some interesting information such as the vesicles solution concentration and also information on the vesicle's adhesion on the Pt surface. The sharpness of the steps (rise time 0.25 s) suggests that any vesicle distortion or spreading either occurs very quickly or, more likely, that the vesicle maintains its essentially spherical shape.

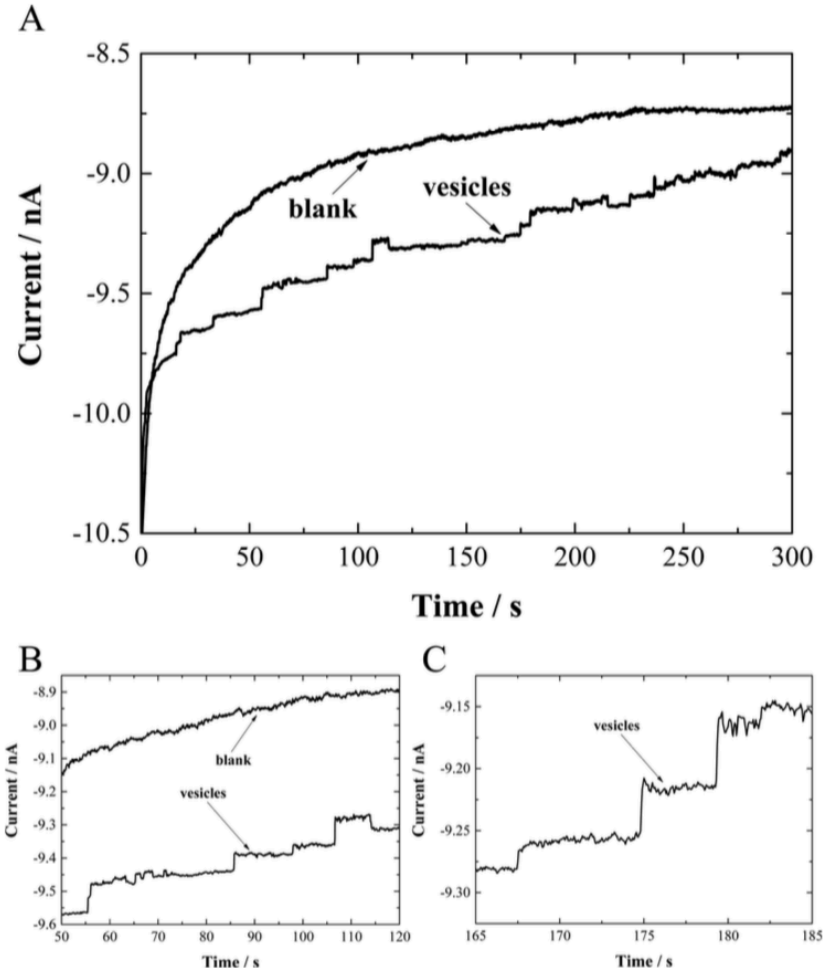

Figure 3.2: (A) The i−t curve for collision experiments by vesicles blocking method recorded at +0.6 V vs Ag/AgCl on 1.7 μm Pt UME in 2 mL of 0.2 M $K_4Fe(CN)_6$ aqueous solution in the absence (blank) and in the presence (vesicles) of 5 μL of DMPC vesicles aqueous solution. (B) and (C) are enlarged portions of the initial figure (A).

3.5 Evaluating Vesicle Size Distribution Using Vesicle Reactor Method

The electrochemical detection of collisions by vesicle reactor method is presented in Figure 3.3. The main observation in Figure 3.3 was the absence of current spikes in the chronoamperometric i−t curve recorded in the presence of DMPC vesicles without surfactant. Indeed, this curve showed a similar shape to the one recorded in potassium

phosphate buffer (KPB) aqueous solution (in the absence of vesicles solution) with the same trend to reach the steady-state current. This result shows no oxidation of the vesicles content occurred during each collision, suggesting no lipid bilayer collapse against the Pt UME. According to the VB method applied to redox DMPC vesicles, we can affirm that vesicles irreversibly adsorb onto the Pt UME, but the VR technique presented in Figure 3.3 clearly demonstrated that electron transfer does not occur through the BLM because electron tunneling and ion transfer are not facile through such a thick barrier.[18-19, 30] Thus, in agreement with previous studies about the vesicle adsorption on various substrates,[11-12] DMPC vesicles seem to remain intact during their collision on the Pt UME hydrophilic surface.

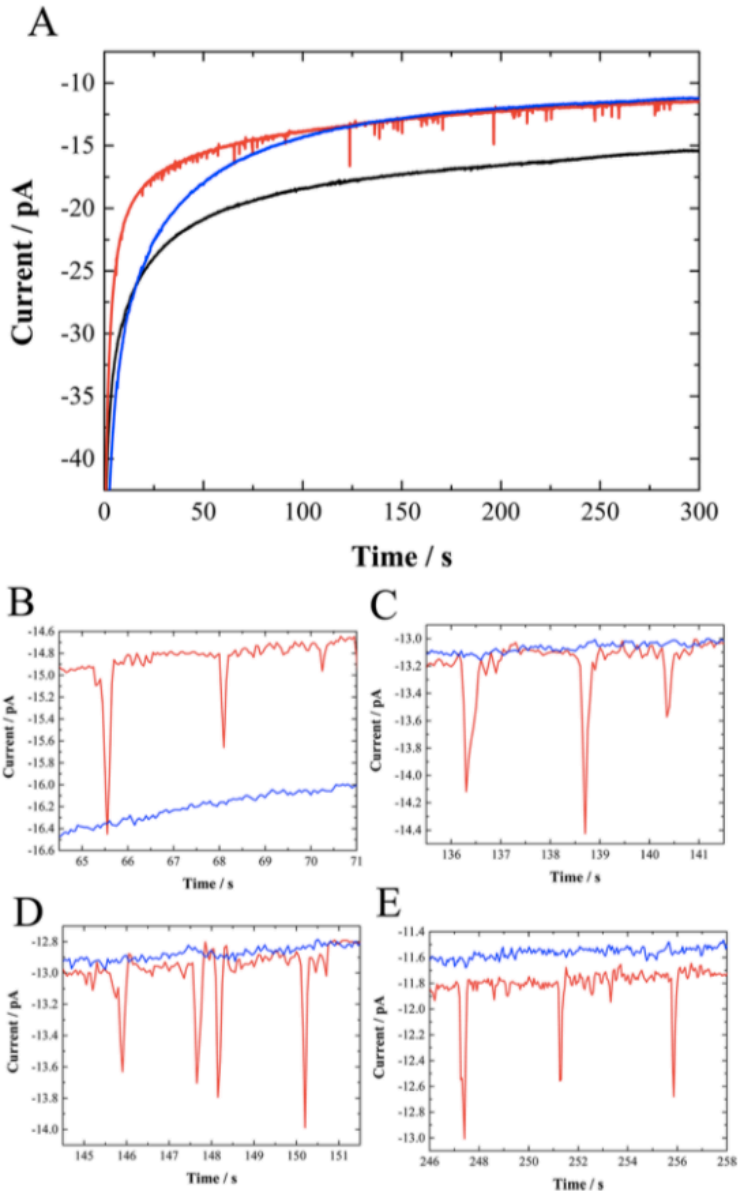

Figure 3.3: The i−t curve for collision experiments by vesicles reactor method recorded at +0.6 V vs Ag/AgCl on 1.7 µm Pt UME in 2 mL of 0.1 M KPB aqueous solution at pH 7 in the absence (black) and in the presence of 20 µL of redox DMPC vesicles aqueous solution with (red) and without (blue) addition of 0.2 mM Triton X-100 surfactant. (B−E) are enlarged portions of the initial figure (A).

In this case, to increase the membrane permeability, the use of a surfactant was required. The i−t curve recorded immediately after addition of an appropriate concentration of TX100 (vide infra, Figure 3.4) showed several current spikes over 300 s (Figure 3.3) with a frequency estimated at 0.28 Hz. Note the narrow shape of these current spikes detected at Pt UME, which are clearly different than those observed in previous studies.[6-7] Indeed, contrary to the expected "blip" shape (Figure 3.1), here the current spikes present a symmetrical and sharp shape for a time ranging between 0.2 and 0.5 s. This result indicates that mechanism occurring during single vesicle collisions at Pt UME in the presence of an appropriate concentration of TX100 is probably different to those reported by Compton and Ewing at a carbon UME.[6-7] Moreover, this short time observed for current spikes suggests a quick releasing of the content against the Pt UME in a rapid electrolysis process. Thus, the electrolysis mechanism of the DMPC vesicles content during the collision at the Pt ultramicroelectrode surface in the presence of surfactant seems more complicated than a simple releasing process and probably requires additional studies to improve the understanding.

As previously shown in the VB technique, the vesicles concentration (C_{ves}) can be calculated by using eqs 1 and 2 based on 120 nm diameter vesicles (determined by DLS and NTA data). Hence, the concentration of the pure redox DMPC vesicles aqueous solution before dilution is evaluated at 4.4 ± 0.1 nM, a value close to that determined by NTA at 3.3 ± 0.2 nM and also in good agreement with the vesicles concentration determined by the VB method (Figure 3.2). This result indicates again that migration effects are less significant than diffusion, which is expected because very little faradaic current is flowing during VR experiments.[28]

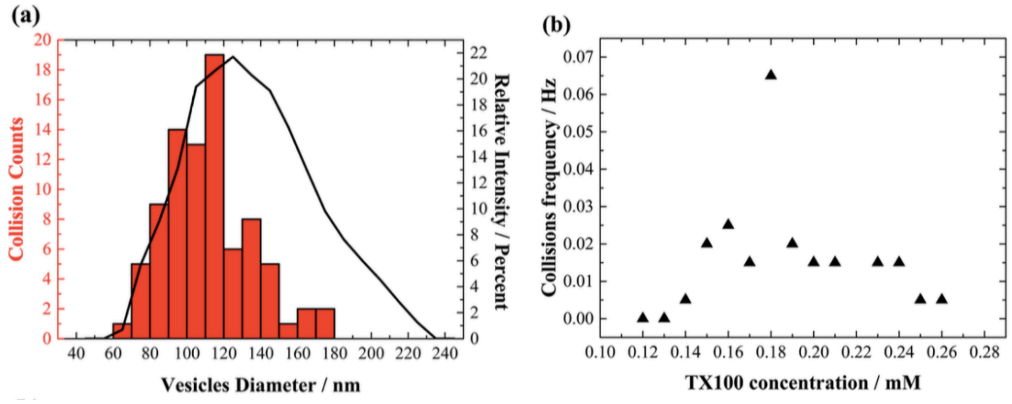

Figure 3.4: (a) Size distributions from DLS data (black line) and from charge data by integrating current spikes of i−t curve recorded at +0.6 V vs Ag/AgCl on 1.7 µm Pt UME in 2 mL of 0.1 M KPB aqueous solution at pH 7 in the presence of 20 µL of DMPC vesicles aqueous solution and 0.2 mM TX100 surfactant (red bar). (b) Collisions frequency determined from i−t curves of collision experiments by vesicles reactor method recorded at +0.6 V vs Ag/AgCl on 1.0 µm Pt UME in 2 mL of 0.1 M KPB aqueous solution at pH 7 in the presence of 10 µL of redox DMPC vesicles aqueous solution after addition of small TX100 concentrations every 5 min. The unusual single unique maximum point was seen in three trials where it varied over a range of 0.05 mM.

Moreover, to confirm that current spikes are due to oxidation of $Fe(CN)_6^{4-}$ contained inside the vesicle during its collision, we can estimate the diameter of each vesicle from the charge obtained by calculating the charge passed during the collision, which corresponds to the amount of ferrocyanide oxidized and using Faraday's law. Here, we assume that the initial concentration of ferrocyanide introduced into the vesicle solutions before extrusion is the same in each vesicle (i.e., an attoliter aliquot of the original solution), and we also assume that the electrode consumes all of the contents of the vesicle. In addition, we considered the cutoff for a "signal" (current spike) when the spike was at least three times the background noise in current. A background experiment without redox species inside DMPC vesicles showed no current spike.

Thus, the vesicle diameter (d_{ves}) can be calculated by equation 3-3:

$$d_{ves} = 2^3 \sqrt{\frac{3Q}{4\pi n_e F C_{redox}}} \qquad \text{(Equation 3-3)}$$

where Q is the measured charge, n_e is the number of electrons transferred during the electrolysis, n_e =1, F is Faraday's constant, and C_{redox} is the concentration of redox species encapsulated in the vesicles, C_{redox} = 0.5 M.

The overlay presented in Figure 3.4a showed that the size distributions from DLS data and calculated data were quite similar. Indeed, the DLS data indicated that the peak diameter is 120 ± 30 nm while the calculated data gave 116 ± 63 nm as mean diameter from the corresponding average charge estimated at 0.079 pC. According to this result, the previous assumptions about the complete electrolysis and the expected concentration of ferrocyanide encapsulated inside vesicles (0.5 M) can be validated and, in addition, that showed the TX100 surfactant does not act on the size distribution of vesicles (nor on the consumed charge) during their collision.

As expected, the VR technique confirmed its efficiency to determine the size distribution of nanometer-sized vesicles and was also relevant to approximate the vesicles concentration in solution. Nevertheless, this last technique provided clear evidence observation of current spikes form these vesicles on a Pt UME necessitated a surfactant, such as TX100, in a controlled concentration. Indeed, TX100 is one of the most widely used nonionic surfactants to permeate the living cell membrane for transfection.[20, 23] In fact, the transfection process consists to the opening of pores or holes in the BLM to allow the hydrophilic species adsorption/desorption of the vesicle content without damaging the membrane.[23] The study of TX100 surfactant concentration effect on the redox DMPC vesicle collisions frequency by detection of corresponding current spikes on Pt UME is presented in Figure 3.4b to determine the appropriate TX100 concentration to use.

Figure 3.4b shows the evolution of the collisions frequency versus the TX100 concentration added every 5 min in the redox DMPC vesicles aqueous solution by recording a chronoamperometric i−t curve (VR method) after each new addition. Especially, a chronoamperometric i−t curve like the one presented in Figure 3.3 is recorded on 300 s every 5 min (after each new addition of TX-100) on a fresh and clean Pt UME, and the collisions frequency (number of collisions during 300 s) is reported in Figure 3.4b for each TX-100 concentration added. The collisions frequency began at 0 Hz for TX100 concentrations below 0.14 mM and increased until the appropriate TX100 concentration at 0.18 mM provided a maximum frequency value of 0.065 Hz. These concentration values are in good agreement with the previous work of Koley and Bard reporting the TX100 concentration effects on membrane permeability of a single HeLa cell, where the TX100 critical micelle concentration (CMC) was evaluated at 0.17 mM.21 According to their study, if the TX100 concentration is above this CMC (>0.18 mM), the cell membrane is irreversibly damaged. Indeed, above 0.18 mM in Figure 3.4b, the collisions frequency quickly decreased, and after 0.25 mM TX100 almost no current spike was detected, suggesting the fatal breaking of the vesicles lipid bilayer. Unfortunately, the concentration of ferrocyanide released in solution following the prospective collapsing of all vesicles is too low (~7 μM) for inducing a significant difference on the background steady state current in 0.1 M KPB aqueous solution. Several experiments have been performed concerning the TX100 concentration effect on single vesicle collisions, and in all cases the collisions frequency curves versus the TX100 concentration have presented the same trend observed in Figure 3.4b with a rapid increase at the appropriate TX100 concentration value around 0.20 ± 0.03 mM. Moreover, all chronoamperometric i−t curves recorded in these conditions showed the same shape and size of current spikes confirming that surfactant does not disturb the

electrolyzed content (integrated charge). Here, the TX100 effect on the vesicles BLM permeability could be explained by a process that involves the more facile release of the ferrocyanide content only during vesicle collision.

Finally, our study showed for the first time that a concentration around 0.20 ± 0.03 mM of TX100 surfactant (dependent on the reaction time) in solution is essential and efficient to detect DMPC vesicles reactor collision events at the Pt UME hydrophilic surface.

3.6 CONCLUSION

In summary, we investigated vesicle behavior composed of a phospholipid bilayer membrane on a Pt ultramicroelectrode surface by two electrochemical detection methods involving discrete collision events. For the first time, we have shown that the vesicle blocking method is a useful technique for observing the vesicle adhesion on the Pt UME surface and also to evaluate the vesicle concentration in solution. Furthermore, our results have confirmed that the vesicle reactor method can be used to determine the vesicle size distribution, but the addition of a surfactant like Triton X-100 is necessary to oxidize the DMPC vesicle content. Indeed, in the absence of surfactant, the BLM does not allow passage of the contents to the UME for electrolysis during the vesicle collision on the Pt UME and is also too thick for allowing electron transfer across the BLM. Therefore, we have shown that the required Triton X-100 concentration is about 0.20 ± 0.03 mM depending on the DMPC vesicle concentration in solution and under these conditions the BLM is permeable to hydrophilic species such as potassium ferrocyanide. Finally, we have suggested a transfection mechanism from the surfactant to explain the current spikes occurring during vesicles reactor collisions at Pt ultramicroelectrode, but this assumption

should be checked by extending this study to other surfactants commonly used for cell transfection and probably also to other encapsulated hydrophilic electroactive species.

3.8 REFERENCES

1. Kim, B.-K.; Boika, A.; Kim, J.; Dick, J. E.; Bard, A. J. Characterizing Emulsions by Observation of Single Droplet Collisions—Attoliter Electrochemical Reactors. *J. Am. Chem. Soc.* **2014,** *136*, 4849-4852.

2. Dick, J. E.; Renault, C.; Kim, B.-K.; Bard, A. J. Electrogenerated Chemiluminescence of Common Organic Luminophores in Water Using an Emulsion System. *J. Am. Chem. Soc.* **2014,** *136*, 13546-13549.

3. Dick, J. E.; Renault, C.; Kim, B.-K.; Bard, A. J. Simultaneous Detection of Single Attoliter Droplet Collisions by Electrochemical and Electrogenerated Chemiluminescent Responses. *Angew. Chem., Int. Ed.* **2014,** *53*, 11859-11862.

4. Kim, B.-K.; Kim, J.; Bard, A. J. Electrochemistry of a Single Attoliter Emulsion Droplet in Collisions. *J. Am. Chem. Soc.* **2015,** *137*, 2343-2349.

5. Cheng, W.; Compton, R. G. Oxygen Reduction Mediated by Single Nanodroplets Containing Attomoles of Vitamin B12: Electrocatalytic Nano-Impacts Method. *Angew. Chem., Int. Ed.* **2015,** *54*, 7082-7085.

6. Cheng, W.; Compton, R. G. Investigation of Single-Drug-Encapsulating Liposomes Using the Nano-Impact Method. *Angew. Chem., Int. Ed.* **2014,** *53*, 13928-13930.

7. Dunevall, J.; Fathali, H.; Najafinobar, N.; Lovric, J.; Wigström, J.; Cans, A.-S.; Ewing, A. G. Characterizing the Catecholamine Content of Single Mammalian Vesicles by Collision–Adsorption Events at an Electrode. *J. Am. Chem. Soc.* **2015,** *137*, 4344-4346.

8. Dick, J. E.; Hilterbrand, A. T.; Boika, A.; Upton, J. W.; Bard, A. J. Electrochemical Detection of a Single Cytomegalovirus at an Ultramicroelectrode and Its Antibody Anchoring. *Proc. Natl. Acad. Sci. U. S. A.* **2015,** *112*, 5303.

9. Toh, H. S.; Compton, R. G. Electrochemical Detection of Single Micelles Through 'Nano-Impacts'. *Chemical Science* **2015,** *6*, 5053-5058.

10. Dick, J. E.; Renault, C.; Bard, A. J. Observation of Single-Protein and DNA Macromolecule Collisions on Ultramicroelectrodes. *J. Am. Chem. Soc.* **2015,** *137*, 8376-8379.

11. Keller, C. A.; Kasemo, B. Surface Specific Kinetics of Lipid Vesicle Adsorption Measured with a Quartz Crystal Microbalance. *Biophys. J.* **1998,** *75*, 1397-1402.

12. Dimitrievski, K.; Kasemo, B. Simulations of Lipid Vesicle Adsorption for Different Lipid Mixtures. *Langmuir* **2008,** *24*, 4077-4091.

13. Hellberg, D.; Scholz, F.; Schauer, F.; Weitschies, W. Bursting and Spreading of Liposomes on the Surface of a Static Mercury Drop Electrode. *Electrochem. Commun.* **2002,** *4*, 305-309.

14. Hellberg, D.; Scholz, F.; Schubert, F.; Lovrić, M.; Omanović, D.; Hernández, V. A.; Thede, R. Kinetics of Liposome Adhesion on a Mercury Electrode. *J. Phys. Chem. B* **2005,** *109*, 14715-14726.

15. Agmo Hernández, V.; Scholz, F. Kinetics of the Adhesion of DMPC Liposomes on a Mercury Electrode. Effect of Lamellarity, Phase Composition, Size and Curvature of Liposomes, and Presence of the Pore Forming Peptide Mastoparan X. *Langmuir* **2006,** *22*, 10723-10731.

16. Agmo Hernández, V.; Niessen, J.; Harnisch, F.; Block, S.; Greinacher, A.; Kroemer, H. K.; Helm, C. A.; Scholz, F. The Adhesion and Spreading of Thrombocyte Vesicles on Electrode Surfaces. *Bioelectrochemistry* **2008,** *74*, 210-216.

17. Kannuck, R. M.; Bellama, J. M.; Durst, R. A. Measurement of Liposome-Released Ferrocyanide by a Dual-Function Polymer Modified Electrode. *Anal. Chem.* **1988,** *60*, 142-147.

18. Young, R. C.; Feldberg, S. W. Photoinitiated Mediated Transport of H3O+ and/or OH- Across Glycerol Monooleate Bilayers Doped with Magnesium Octaethylporphyrin. *Biophys. J.* **1979,** *27*, 237-255.

19. Feldberg, S. W.; Armen, G. H.; Bell, J. A.; Chang, C. K.; Wang, C. B. Electron Transport Across Glycerol Monooleate Bilayer Lipid Membranes Facilitated by Magnesium Etiochlorin. *Biophys. J.* **1981,** *34*, 149-163.

20. Koley, D.; Bard, A. J. Triton X-100 Concentration Effects on Membrane Permeability of a Single HeLa Cell by Scanning Electrochemical Microscopy (SECM). *Proc. Natl. Acad. Sci. U. S. A.* **2010,** *107*, 16783.

21. Fontaine, P.; Fauré, M. C.; Muller, F.; Poujade, M.; Micha, J.-S.; Rieutord, F.; Goldmann, M. Unexpected Stability of Phospholipid Langmuir Monolayers Deposited on Triton X-100 Aqueous Solutions. *Langmuir* **2007,** *23*, 12959-12965.

22. le Maire, M.; Champeil, P.; Møller, J. V. Interaction of Membrane Proteins and Lipids with Solubilizing Detergents. *Biochim. Biophys. Acta, Biomembr.* **2000,** *1508*, 86-111.

23. Gennuso, F.; Fernetti, C.; Tirolo, C.; Testa, N.; Episcopo, F.; Caniglia, S.; Morale, M. C.; Ostrow, J. D.; Pascolo, L.; Tiribelli, C.; Marchetti, B. Bilirubin Protects Astrocytes from its own Toxicity by Inducing Up-Regulation and Translocation of

Multidrug Resistance-Associated Protein 1 (Mrp1). *Proc. Natl. Acad. Sci. U. S. A.* **2004,** *101*, 2470.

24. Lanyi, J. K. Influence of Electron Transport on the Interaction Between Membrane Lipids and Triton X-100 in Halobacterium Cutirubrum. *Biochemistry* **1973,** *12*, 1433-1438.

25. Kim, J.; Izadyar, A.; Nioradze, N.; Amemiya, S. Nanoscale Mechanism of Molecular Transport through the Nuclear Pore Complex As Studied by Scanning Electrochemical Microscopy. *J. Am. Chem. Soc.* **2013,** *135*, 2321-2329.

26. Kim, J.; Kim, B.-K.; Cho, S. K.; Bard, A. J. Tunneling Ultramicroelectrode: Nanoelectrodes and Nanoparticle Collisions. *J. Am. Chem. Soc.* **2014,** *136*, 8173-8176.

27. Kwon, S. J.; Zhou, H.; Fan, F.-R. F.; Vorobyev, V.; Zhang, B.; Bard, A. J. Stochastic Electrochemistry with Electrocatalytic Nanoparticles at Inert Ultramicroelectrodes—Theory and Experiments. *Phys. Chem. Chem. Phys.* **2011,** *13*, 5394-5402.

28. Boika, A.; Thorgaard, S. N.; Bard, A. J. Monitoring the Electrophoretic Migration and Adsorption of Single Insulating Nanoparticles at Ultramicroelectrodes. *J. Phys. Chem. B* **2013,** *117*, 4371-4380.

29. Einstein, A. Über die von der molekularkinetischen Theorie der Wärme geforderte Bewegung von in ruhenden Flüssigkeiten suspendierten Teilchen. *Ann. Phys.* **1905,** *322*, 549.

30. Kučerka, N.; Kiselev, M. A.; Balgavý, P. Determination of Bilayer Thickness and Lipid Surface Area in Unilamellar Dimyristoylphosphatidylcholine Vesicles from Small-Angle Neutron Scattering Curves: A Comparison of Evaluation Methods. *Eur. Biophys. J.* **2004,** *33*, 328-334.

Chapter 4: Effect of Cholesterol and 6-Ketocholestanol on Membrane Dipole Field

4.1 Publication Note

Portions of the methods outlined in this section were adapted from the following publication:

Shrestha, R.; **Anderson, C. M.**; Cardenas, A. E.; Elber, R.; Webb, L. J. Direct Measurement of the Effect of Cholesterol and 6-Ketocholestanol on Membrane Dipole Field Using Vibrational Stark Effect Spectroscopy Coupled with Molecular Dynamics Simulations. *J. Phys. Chem. B* **2017,** *121,* 3424-3436. [C. M. Anderson performed all experiments with 6-ketocholestanol including vesicle preparation, characterization and CD and FTIR spectroscopies. R. Shrestha performed all experiments with cholesterol. A. E. Cardenas performed all of the molecular dynamics simulations.]

4.2 Introduction

Cholesterol and its derivatives, such as 6-ketocholestanol (6- kc), ergosterol, and 7-dehydrocholesterol, have various physicochemical effects on lipid membranes stemming from excluded volume, steric, and electrostatic factors that collectively modify bilayer structure, fluidity, and function. Of these, the sterols' effect on the membrane dipole electric potential (V_d) is the least understood.[1-3] The dipole electric potential is perpendicular to the plane of the membrane and is the result of the anisotropic orientation of molecular dipole moments of charged moieties in the head group region of the lipid distributed between the lipid−water interface and the hydrocarbon interior of the membrane. The potential generated from these accumulated dipole moments, largely from the zwitterionic lipid head groups and from water molecules that are hydrogen bound to it, propagates a few nanometers through the low dielectric hydrophobic interior

of a membrane, resulting in a large electrostatic dipole electric field that a variety of experimental and computational techniques have estimated to be ~1−10 MV/cm.

In recent years, the effect of cholesterol on membrane dipole potential has been a subject of great interest. A substantial amount of experimental and computational research has focused on this subject, but the results of these efforts have occasionally been contradictory. Several experimental[3] and computational[4-7] results show that cholesterol increases the electric potential inside a membrane, but in contrast, additional studies have concluded that cholesterol also decreases the membrane electric potential.[3, 8] Researchers have proposed several hypotheses: (1) cholesterol increases the dipole potential by altering the strength and orientation of dipole moments associated with lipid head groups;[4] (2) cholesterol increases the dipole potential by increasing the volume of lipid headgroup, which in turn reorganizes the presence of water dipole moments at the membrane interface;[9] or (3) the dipole moment of cholesterol itself adds incrementally to the magnitude of the electric potential dropped across the bilayer.[3] These hypotheses have been proposed based on the results of a variety of indirect experimental techniques such as atomic force microscopy,[10] ion-transport rates,[11] ratiometric fluorescence measurements,[2, 12] and conductance method;[1] or computationally through MD simulations[5, 8, 13] applied on lipid bilayers with different amounts of cholesterol.

In this work we used vibrational Stark effect (VSE) spectroscopy to measure the electrostatic field inside a lipid bilayer containing different amounts of sterol molecules using a combined experimental and computational methodology that was developed and described previously in our laboratory.[14-15] In earlier work in our laboratory with DMPC vesicles, we placed a nitrile oscillator into the bilayer interior by intercalating an α-helical transmembrane peptide containing an unnatural amino acid, *p*-cyanophenylalanine (*p*-CN-Phe).[15] The nitrile molecule served as an excellent VSE probe, as is described

extensively in earlier publications.[14-18] The nitrile on *p*-CN-Phe is a good reporter of the local electrostatic environment because it has a large Stark tuning rate (or difference dipole moment) and the nitrile vibration is also in a clean area of the infrared spectrum. We controlled the location of nitrile inside the bilayer by changing the position of *p*-CN-Phe along the amino acid sequence of the transmembrane peptide. The four polypeptide sequences that we used in this study are given in Table 4.1 and shown schematically in Figure 4.1.[14-15] The peptide αLAX(25) places the nitrile near the lipid head group-water interface, where it was exposed to a very heterogeneous chemical environment containing charged groups and polar water molecules. At the other extreme, peptide αLAX(16) places the nitrile in a homogeneous environment near the middle of the membrane that is mainly comprised of hydrocarbon chains. We confirmed the chemical differences in the local vicinity of these probes both experimentally (through differences in vibrational absorption line widths), and computationally (through MD simulations) and determined the magnitude of the dipole electric field in a DMPC bilayer to be 8−11 MV/cm, depending on a variety of factors, such as vesicle size, probe concentration, and nitrile orientation.[15]

Peptide	Sequence
αLAX(25)	HHGGPGLALALALALALALALA**X**GPGGHH
αLAX(21)	HHGGPGLALALALALALALA**X**ALGPGGHH
αLAX(21)	HHGGPGLALALALALALA**X**ALALGPGGHH
αLAX(16)	HHGGPGLALALALAL**X**LALALALAXGPGGHH

Table 4.1: Polypeptide sequences of peptides used for VSE measurements. (**X** = *p*-cyanophenylalanine)

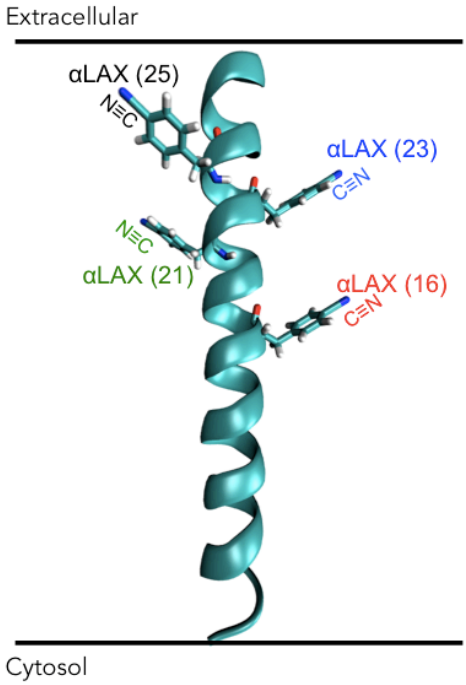

Figure 4.1: Schematic representation of transmembrane peptide used. Note that this represents 4 different peptides, each with a nitrile located at one of the four depicted locations.

In the work described in this chapter we expanded the use of VSE spectroscopy and MD simulation studies to understand the role of chemical complexity on the magnitude and function of the membrane electric field through direct measurements of the field upon addition of cholesterol and 6-kc at physiologically relevant concentrations up to 40 mol%. Experimental measurements show that cholesterol increases the electric field at lower concentrations (~10 mol%) and decreases it at higher concentrations (up to 40 mol%), while 6-kc increases the electric field monotonically through the range we investigated. We used molecular dynamics simulations to examine the lateral organization of these sterols within the lipid-αLAX(16) bilayer at the sterol concentrations of 10, 20, and 40 mol%. We also evaluated the orientations of the helix and of the nitrile probe attached to the helix from the simulations. Using our experimental

data and results from simulation studies, we demonstrated that both the chemical structure and the concentration of sterol affect the chemical environment of the bilayer, which in turn alters the membrane dipole field.

4.3 METHODS

Vesicles used for this study were prepared using the sonication method, outlined in Section 2.3.1. Vesicle samples were made in a 10 mM Hepes buffer at pH 7.2. DMPC lipids were used at a concentration of 30 mM, sterols (cholesterol or 6-kc) were added at concentrations of 0, 5, 10, 15, 20, 30 and 40 mol% and 1mM of peptides were added. On average, in a homogeneous distribution of 1 mM peptide results in a ratio of 33 peptides per 1000 lipids. All of the vesicles were characterized as 100 nm SUVs using dynamic light scattering (DLS), atomic force microscopy (AFM) and ^{31}P NMR as described in detail in Section 2.4.

4.3.1 Circular Dichroism (CD) Spectroscopy

Along with our standard characterization of the lipid vesicles, we ensured that the transmembrane peptides with the VSE probe retained α-helical character in all of the lipid/sterol/peptide vesicle systems. The secondary structure of the peptides inside the vesicles was determined by circular dichroic (CD) spectroscopy using a Jasco J-815 CD spectrometer. CD spectra were recorded using a 1 mm path length quartz cell over the range of 190−250 nm wavelength at 0.2 nm resolution, 50 nm/min scanning rate and 4 s response time and were background subtracted using 10 mM Hepes buffer as the background with Spectra Manager for Windows 95/NT Spectra Analysis software.

4.3.2 Fourier Transform Infrared (FTIR) Spectroscopy

The dipole field was measured using VSE spectroscopy. Infrared spectra of vesicle samples containing the VSE probe were recorded at room temperature (>T_m) in a sample cell composed of two sapphire windows separated by 125 μm thick PETE spacers in a Bruker Vertex 70 FTIR instrument. The sample cell was illuminated with light in the range of 2000−2500 cm^{-1} selected by a broad band-pass filter (Spectrogon, Parsippany, NJ) placed in front of the instrument's IR source. Spectra were collected with a liquid nitrogen-cooled indium antimide (InSb) detector and were composed of 3000 scans at 2.0 cm^{-1} spectral resolution. Background-subtracted spectra were fit to a single Gaussian line shape with a custom least-squares fitting program to determine the peak center, ν_{obs}, and full width at half-maximum (fwhm). Uncertainty in absorption energy was reported as the standard deviation of at least three measurements.

4.4 Comparing Cholesterol and 6-Ketocholestanol

The chemical structures of the sterols cholesterol and 6-kc are shown in Figure 4.2. Although cholesterol and 6-kc are structurally very similar, differing only by the lack of a double bond and the addition of a ketone group on the second ring on 6-kc, their effects on the membrane dipole field and membrane organization are quite different.[3, 11-12, 19-20] Due to the ketone group on 6-kc, it has been shown to sit further up in the bilayer compared to cholesterol because the additional oxygen forms hydrogen bonds with the interfacial waters and increases membrane fluidity compared to membrane with similar composition of cholesterol.[20] This is in contrast with cholesterol, which sits deeper in the bilayer under lipid head groups, which are extremely dynamic in solution and create "umbrellas" over one another due to the favorable interactions between the positively

charged phosphate groups and negatively charged choline groups on the lipid heads. This in turn makes the bilayer less fluid.

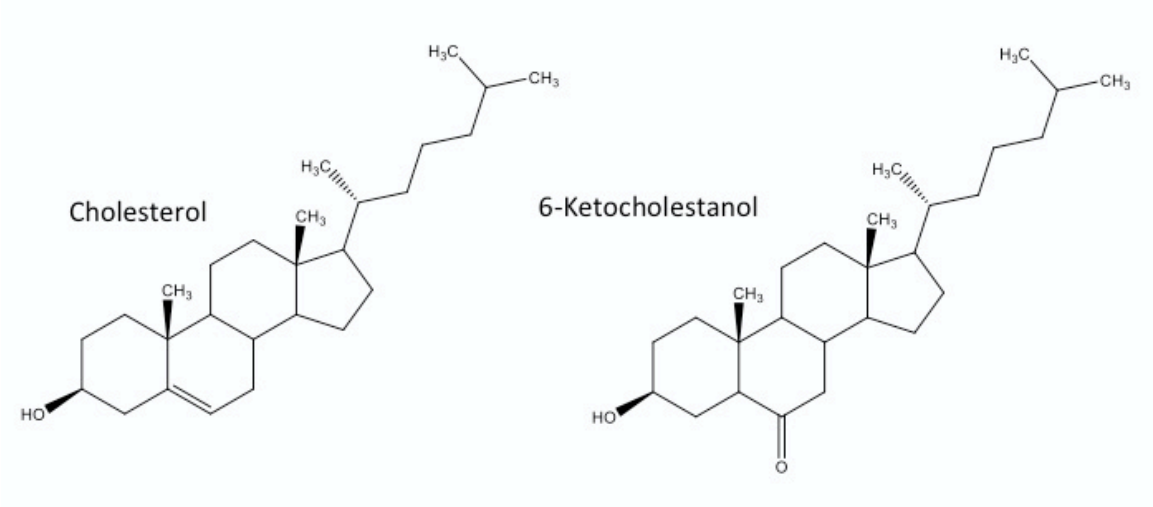

Figure 4.2: Chemical structures of sterols used in this work- cholesterol (left) and 6-ketocholestanol (6-kc, right).

4.5 CD SPECTROSCOPY

In these experiments, we moved the nitrile infrared probe through the lipid bilayer by inserting a polypeptide containing the unnaturnal amino acid *p*-CN-Phe at various locations along the sequence. The repeating leucine-alanine (LA) construct in the amino acid sequences shown in Table 4.1 are strongly hydrophobic helical peptides that are insoluble in buffer, but partitions into the self-assembling membrane bilayer during vesicle formation.[14-15] We confirmed the helical secondary structure of these nitrile-containing peptides inside vesicles containing 0−40 mol% cholesterol and 6-kc with CD spectroscopy, shown in Figure 4.3. All peptides show two minima located near 208 and 222 nm, which are characteristics of helical secondary structure. On average, a homogeneous distribution of 1 mM peptide results in a ratio of 33 peptides per 1000

lipids. Although long-range electrostatic interactions between peptides are possible at such concentrations, we did not observe any distortions in the CD spectra, demonstrating that peptides did not aggregate within the bilayer at this low concentration.

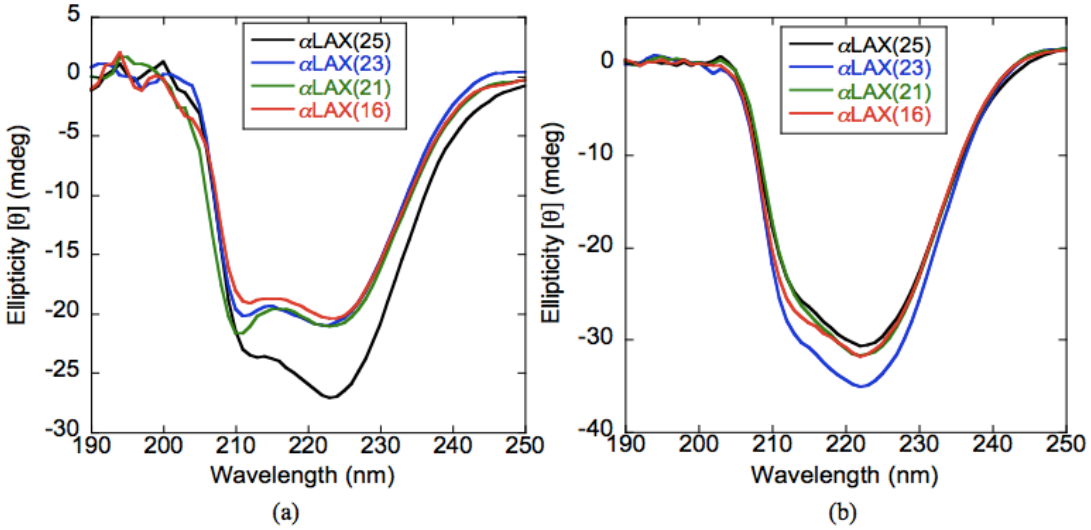

Figure 4.3: Circular dichroic (CD) spectra of 1 mM peptides: αLAX(25) (black), αLAX(23) (blue), αLAX(21) (green), and αLAX(16) (red) inserted in vesicles composed of (a) 30mM DMPC and 20 mol % cholesterol and (b) 30mM DMPC and 20 mol % 6-kc.

4.6 Fourier-Transform Infrared Spectroscopy

We used α-helical peptides containing a single *p*-CN-Phe unnatural amino acid to incorporate the nitrile oscillator at four different positions within the bilayer, beginning from the membrane-water interface with peptide αLAX(25) and progressing toward the middle of hydrophobic core with peptide αLAX(16). FTIR spectra of these systems were collected, and differences in absorption energy and fwhm were analyzed to investigate the electrostatic field across the membrane interior. The potential gradient between the lipid's charged head group and terminal alkyl chains creates an electric field that shifts the vibrational absorption energy of the nitrile oscillator between αLAX(25) and

αLAX(16).[21-22] In Figure 4.4, we show representative normalized infrared spectra of the nitrile stretching band in αLAX(25), αLAX(23), αLAX(21), and αLAX(16) placed into vesicles composed of 30 mM DMPC and 20 mol% 6-kc. In the figure, the absorption energy of the nitrile shifted by 2.8 cm^{-1} between αLAX(25) and αLAX(16). We carried out a series of infrared absorption measurements in vesicles containing 0 to 40 mol% cholesterol or 6-kc. We determined the vibrational energy shifts ($\Delta\nu_{obs}$) at each composition and the results are provided in Table 4.2 and plotted as a function of sterol concentration in Figure 4.5 for both cholesterol (black) and 6-kc (red). We see two distinct trends in values as a function of sterol mole fraction in the bilayer. As we increased the concentration of cholesterol from 0 to 10 mol% in our vesicles, $\Delta\nu_{obs}$ increased from 2.59 ±0.08 to 2.85 ± 0.03 cm^{-1} but as we increased beyond 10 mol%, $\Delta\nu_{obs}$ declined to as low as 2.37 ± 0.07 cm^{-1} for 40 mol% cholesterol. In contrast, in vesicles containing 6-kc, $\Delta\nu_{obs}$ increased monotonically from 2.6 ± 0.2 cm^{-1} to 3.03 ± 0.1 cm^{-1} with increasing concentration over the entire range examined.

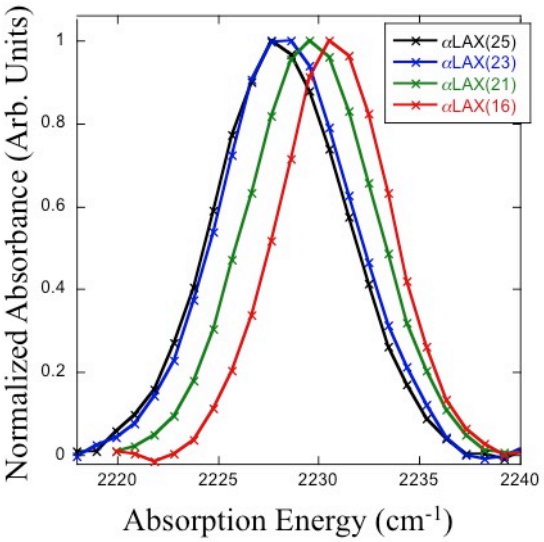

Figure 4.4: Normalized representative FTIR spectra of 1 mM peptides αLAX(25) (black), αLAX(23) (blue), αLAX(21) (green), and αLAX(16) (red) inserted in vesicles composed of 30 mM DMPC and 20 mol% 6-kc. Experimental data points are shown with "×".

Sterol (mol%)	6-ketochoelstanol/DMPC $\Delta\nu_{obs}$ (cm^{-1})	cholesterol/DMPC $\Delta\nu_{obs}$ (cm^{-1})
0	2.6 ± 0.2	2.59 ± 0.08
5	2.8 ± 0.1	2.79 ± 0.01
10	2.85 ± 0.04	2.85 ± 0.03
15	2.83 ± 0.01	2.80 ± 0.02
20	2.86 ± 0.07	2.75 ± 0.02
25		2.62 ± 0.02
30	2.9 ± 0.2	2.53 ± 0.02
40	3.03	2.37 ± 0.07

Table 4.2: Experimentally Measured Differences in Nitrile Absorption Energy ($\Delta\nu_{obs}$) when Moved from αLAX(25) to αLAX(16) for DMPC Vesicles Containing Varying Concentrations of Sterol and 1 mM Peptide

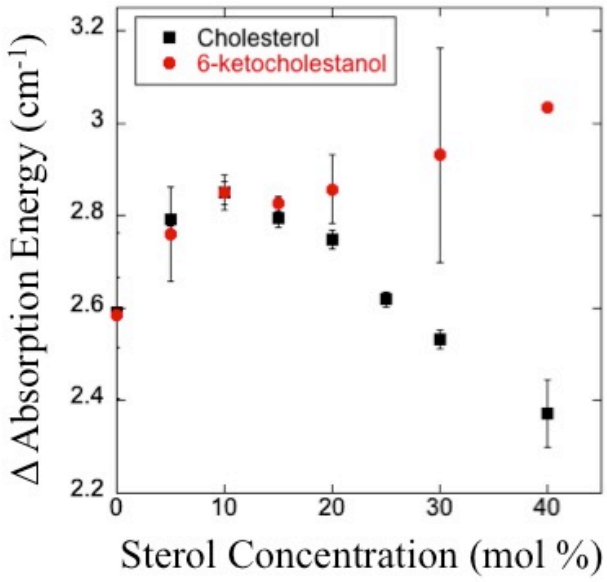

Figure 4.5: The experimentally measured differences in the absorption energy ($\Delta\nu_{obs}$) of the nitrile when moved from αLAX(25) to αLAX(16) for DMPC vesicles containing varying concentrations of sterol and 1 mM peptide plotted as a function of sterol concentration fos cholesterol (black) and 6-kc (red). Error in $\Delta\nu_{obs}$ represents one standard deviation of at least three experimental measurements.

The addition of sterol molecules to a lipid bilayer increased the heterogeneity of the system by changing the order of the lipid alkyl chains. The nitrile probe on peptide αLAX(16) places the oscillator at the ends of these alkyl tails where the system is most perturbed. The oscillator is very sensitive to the local chemical environment, which is reflected in the full width half-maximum (fwhm) values of its absorption peak. In Figure 4.6, we plot the experimental average fwhm values for the absorption peaks of nitrile attached to αLAX(16) that we placed in vesicles containing 0−40 mol% of each sterol. For cholesterol containing bilayers, the fwhm values of nitrile peaks, shown in black circles, rises monotonically with higher cholesterol concentration while the fwhm values of nitrile peaks in 6-kc containing bilayers, shown in red circles, do not exhibit any clear trend as a function of concentration, and appear to fluctuate around a value of ~6.5 cm^{-1}.

This result indicates that the hydrophobic core region of the bilayer, where the nitrile in αLAX(16) is placed, gets progressively more diverse in its chemical environment as the concentration of cholesterol is increased, but remains homogeneous as more 6-kc is added.

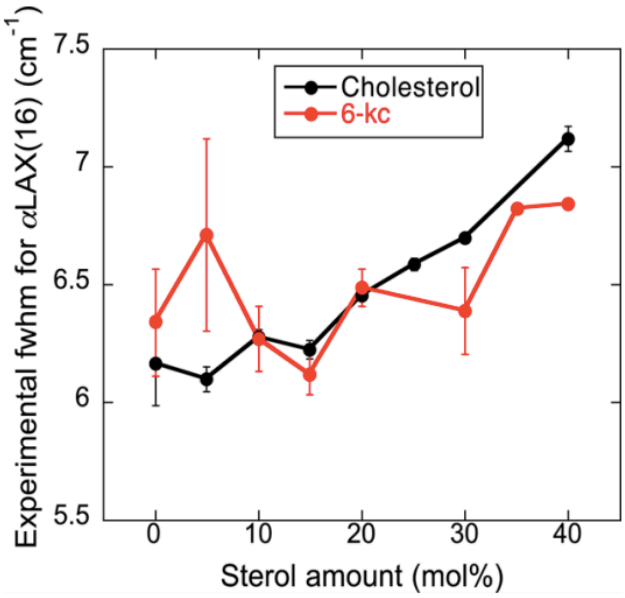

Figure 4.6: Average full width half-maximum (fwhm) values for vibrational absorption peaks of nitrile placed inside sterol-lipidαLAX(16) bilayer for two different kinds of sterol, cholesterol (black) and 6-kc (red), at different concentrations. The values were average of at least three measurements.

4.7 MD Simulations

Although the peptide sequence should put the terminal glycine repeats in the head group region of the bilayer, and although the length of the peptide sequence (28.5 Å)[14-15] was designed to be similar to the hydrophobic length of pure DMPC phospholipid bilayer (26 Å), our experimental methods provide no independent verification that the expectation of transmembrane insertion has been met. The set of CD spectra collected for αLAX(25), αLAX(23), αLAX(21), and αLAX(16) inserted into sterol-lipid bilayer shown

in Figure 4.3 demonstrate the α- helical secondary structure of the peptide but they do not provide information on the orientation of the peptide (horizontal versus vertical) with respect to the bilayer normal. The helix orientation is affected by various physicochemical properties of the lipid bilayer; for example, the hydrophobic mismatch between the helical section of the peptide and the low dielectric hydrophobic alkyl chains, and the chemical interaction between the peptide and its neighboring membrane components. In Figure 4.7, we show representative snapshots taken from the equilibrated helix-membrane simulation, computed by our collaborator Dr. Alfredo Cardenas, of (a) 10 mol% cholesterol; (b) 20 mol% cholesterol; (c) 40 mol% cholesterol; (d) 10 mol% 6-kc; (e) 20 mol% 6-kc; and (f) 40 mol% 6-kc, run for a total of 200 ns each. For the results reported here, all analyses were made from the last 100 ns of simulation data to allow the system to equilibrate. These snapshots clearly show that the peptides are indeed helical and inserted parallel to the membrane normal with some degree of tilt. We calculated the distribution of helix tilt angles from the simulation trajectories for each bilayer composition, and results are shown in Figure 4.8. For cholesterol containing bilayers, the width of the helix tilt distribution became narrower with higher mole fraction of cholesterol, whereas for 6-kc containing bilayers, the distribution widths were broader in general at all mole fractions of 6-kc. For each composition under investigation, the mean helix tilt angles were determined to be 12 ± 5°, 31 ± 5° and 20 ± 4° for 10, 20 and 40 mol% cholesterol, respectively, and 30 ± 6°, 39 ± 5° and 35 ± 4° for 10, 20 and 40 mol% 6-kc, respectively. To check the convergence of the calculation we also present computations of an ergodic measure for the tilt angle in Figure 4.8.

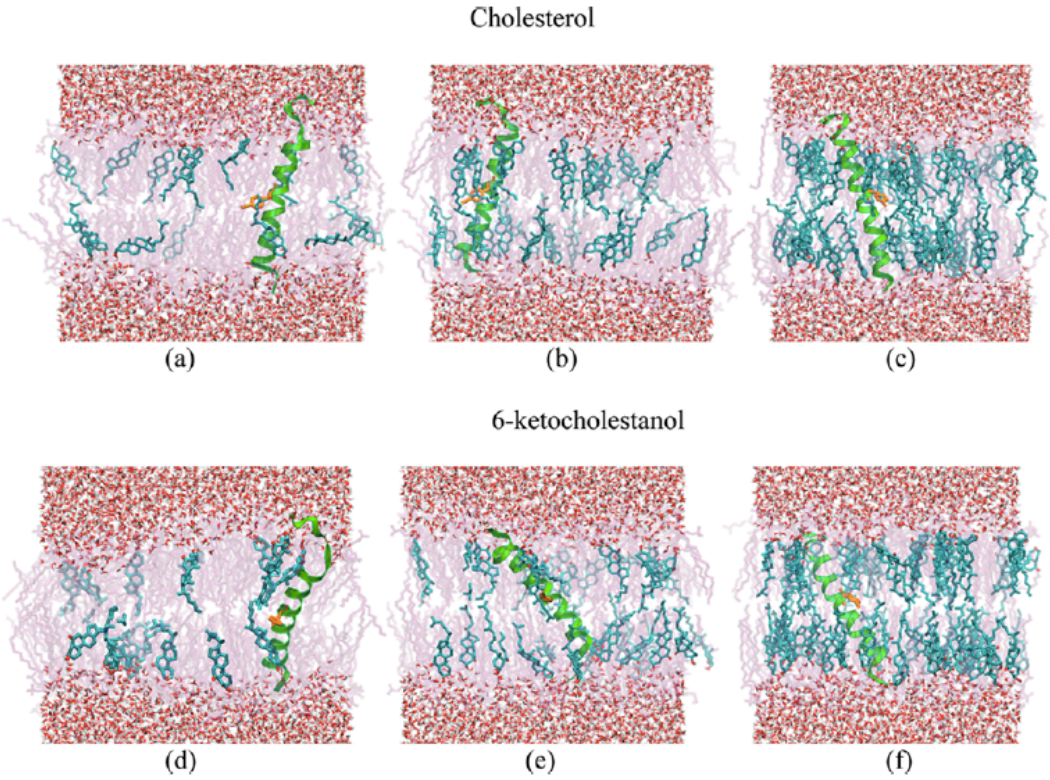

Figure 4.7: Representative snapshots taken from molecular dynamic simulations of αLAX(16) aligned vertically inside a lipid bilayer composed of DMPC molecules and (a) 10 mol% cholesterol; (b) 20 mol% cholesterol; (c) 40 mol% cholesterol; (d) 10 mol% 6-kc; (e) 20 mol% 6-kc; and (f) 40 mol% 6-kc. SPC water molecules are shown in red and gray, sterol molecules are shown in cyan, the p-CN- probe is shown in orange and DMPC phospholipids are shown in light purple. Molecular snapshots were prepared with the program VMD.

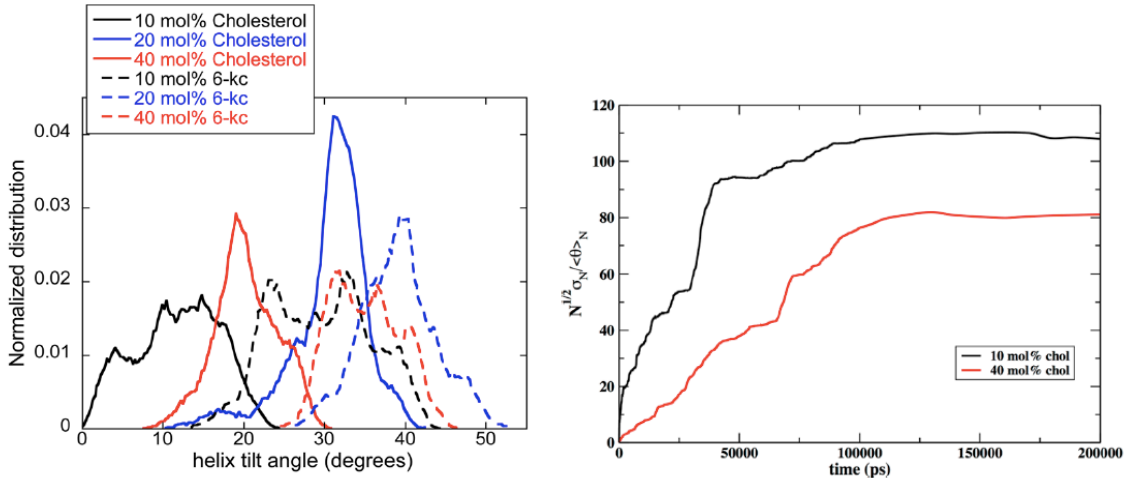

Figure 4.8: Left: Normalized distribution of the helix tilt of αLAX(16) with respect to the membrane normal obtained from MD simulation of the peptide embedded into bilayer composed of DMPC and cholesterol (solid line) and DMPC and 6-ketocholestanol (dashed line) at concentrations of 10 mol% (black), 20 mol% (blue), and 40 mol% (red). Right: Ergodic measure calculations as a function of time. We illustrate that the standard deviation of the averaged tilt angle divided by the average of the tilt angle is proportional to $N^{1/2}$. This observation suggests that the average does not drift and is consistent with uniform sampling from the normal distribution (or central limit theorem). Here the vector connecting histidine 1 and histidine 31 defines the orientation of the helix. Very similar results were obtained when all the alpha carbons of the helix were considered and the helix was overlapped with the initial configuration to determine the tilt angle. See text for more details. We have used this measure in the past for membrane simulations.

Molecular dynamics simulations allowed us to examine the lateral organization of membrane components, including peptide, phospholipids, and sterol molecules in our model sterol-lipid- αLAX(16) bilayer. In our computational model, we inserted one αLAX(16) helical peptide at each composition under investigation that are described in Table 4.3. We computed the three-dimensional radial distribution function, g(r), of the center of mass of the sterol molecules with respect to the nitrile probe attached to the

helix for bilayers containing 10 mol% and 40 mol% sterol. These results are shown in Figure 4.9.

sterol composition	# of DMPC	# of sterol	# of water	Total # atoms
10%	144	16	7150	28785
20%	128	32	6909	27790
40%	96	64	6355	21362

Table 4.3: Composition Details of the Simulations Performed for Cholesterol and 6-Ketocholestanol

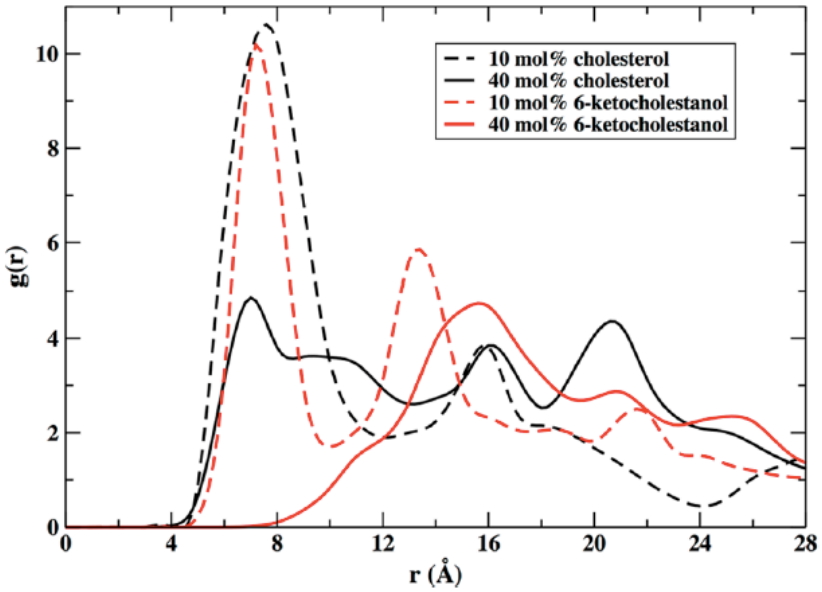

Figure 4.9: Three-dimensional radial distribution function, g(r), between the position of the probe in the helix αLAX(16) and cholesterol (black), and αLAX(16) and 6-kc (red) calculated from the MD simulation of sterol-lipid-αLAX(16) containing 10 mol% sterol (dashed lines) and 40 mol% sterol (solid lines).

The pair correlation functions, shown in Figure 4.9, report the proximity of the probe and the sterol molecules. The following observations were made: (i) at 10% content of sterol we found a first density peak at about 7−8 Å, indicating that the sterol

molecules are near the probe. The first peak of 6-kc was slightly shifted to shorter distances. We also found a second significant peak for the 6-kc molecules at about 13 Å. The second peak of the nitrile-cholesterol distribution was shifted to 16 Å and was less pronounced. The reduction in the second peak of the 10% cholesterol was geometrical and is due to the use of three-dimensional distributions. (ii) At high concentrations of sterols, 6-kc was shifting away from the probe while cholesterol molecules remained closer to the helix. The cholesterol molecules at the higher concentrations are distributed more uniformly in the membrane but the absolute number of sterol molecules in the neighborhood of the probe (the first density peak) was larger than the number determined at the low concentrations.

We also computed the sterol−sterol radial distribution function (RDF) for sterol−lipid−αLAX(16) bilayers containing 40 mol% cholesterol and 40 mol% 6-kc. In a lipid bilayer containing 40 mol% sterol, we distributed equally 64 total sterol molecules (shown in Table 4.3) among the outer and inner leaflets of the bilayer. For each layer we computed the distance between the center of mass of a reference sterol and the other 31 sterols in the same leaflet. We performed a similar calculation for the rest of the sterols in the bilayer. Figure 4.10 shows the results of the radial distribution analysis for both cholesterol and 6-ketocholestanol. We consider the distributions averaged over all sterol molecules in the leaflet (top) and the largest clusters only (bottom). The peak profile in cholesterol−cholesterol RDF plot (top, shown in black) was slightly different from the peak profile obtained for 6-kc−6-kc RDF plot (shown in red). The RDFs of the largest clusters (Figure 4.10b) had significant second and even third peaks. The most obvious observation of Figure 4.10b was the higher first peak of 6-kc compared to the cholesterol molecules, suggesting that 6-kc has stronger tendency to form short-range clusters. Taken together, the RDF results shown in Figures 4.9 and 4.10 indicate that 6-kc is attracted to

itself more than it is attracted to the probe. Cholesterol shows the opposite behavior; interactions with other cholesterol molecules are weaker compared to those with the helix. This may be due to the relative position of the two sterols. 6-Ketocholestanol is placed higher in the membrane, a position with larger mass density.

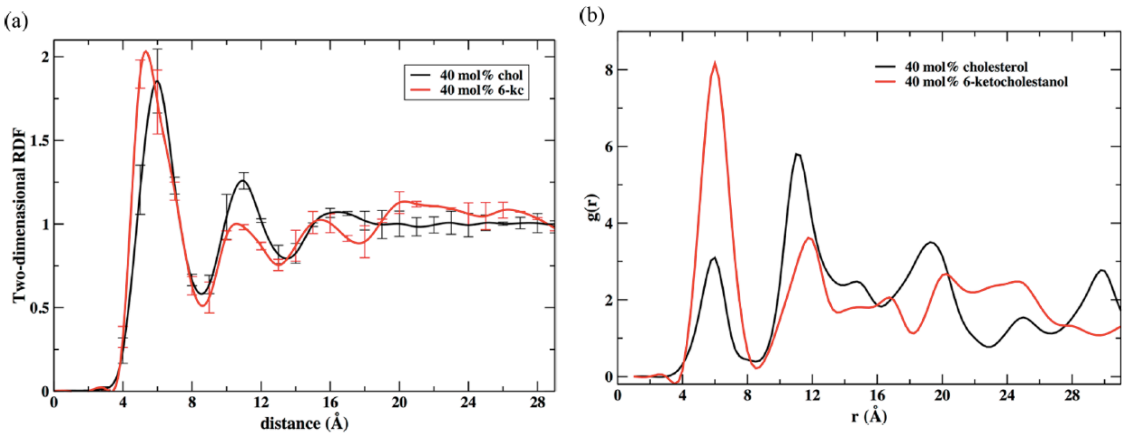

Figure 4.10: Sterol−sterol radial distribution function in the membrane plane. Left: The distribution is computed for all sterol molecules of sterol-lipid-aLAX(16) bilayers containing 40 mol% cholesterol (black) and 40 mol% 6-kc (red). Right: The distribution is computed for the largest clusters of sterol molecules. The largest cluster size for cholesterol molecules was 3, and for 6-kc it was 4. The number of molecules included in the first peak of the RDF determines the cluster size.

Pair correlation functions in the liquid phase rapidly approach a asymptotic constant value as a function of distance. They are typically flat after the first or second peaks. Here, however, we observed more structure beyond the smallest clusters of molecules in direct contact to include sterols separated by a small number of lipid molecules. When the distribution was averaged over all cholesterol molecules a more homogeneous picture was obtained. Finally, we comment that the presence of the sterol molecules, (with the exception of 40% 6-kc), does not change the orientation of the

phospholipid dipoles significantly, measured by the P−N vector with respect to the membrane normal.

The membrane−water interface is extremely heterogeneous, due in large part to a network of hydrogen bonds between phospholipid head groups, water molecules, and sterols. As sterol concentration changes, the distribution of these hydrogen bonds will change as well, altering the arrangement of dipoles at the membrane−water interface. We calculated the average number of hydrogen bonds between different hydrogen bond donor and acceptor chemical pairs in the sterol−lipid−αLAX(16) bilayer model. In Figure 4.11, we present the results for phospholipid:water (black); phospholipid:phospholipid (blue); phospholipid:sterol (green); sterol:sterol (red); and sterol:water (magenta) calculated from MD simulations of lipid bilayer containing cholesterol (solid circles) or 6-kc (open circles) plotted as a function of sterol concentration. Figure 4.11 highlights two important observations: (1) the number of hydrogen bonds between phospholipids and water were largest compared to other molecules because of the greater number of hydrogen bond donors and acceptors located at the phospholipid head group; and (2) the only significant difference between cholesterol and 6-kc in this analysis was the extent of hydrogen bonding between the sterol and the water (data shown in magenta). Because of the extra ketone functional group on 6-kc, this sterol is susceptible to significantly more hydrogen bonds to water than cholesterol (1 versus 0.6 hydrogen bonds per sterol, respectively) at all concentrations. This observation is significant because water dipoles are thought to be a major contributor to the magnitude of the electric field. We will return to this observation below.

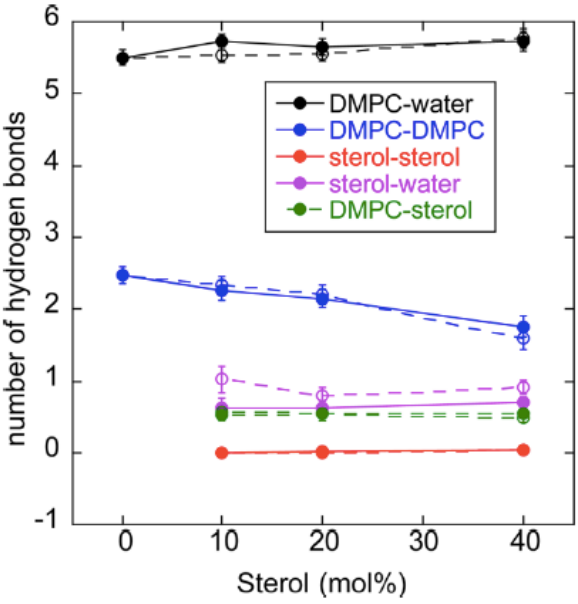

Figure 4.11: Molecular interactions in lipid bilayer containing cholesterol (solid lines) and 6-kc (dashed lines) at different concentrations. The average number of hydrogen bonds (per lipid) calculated between phospholipid:water (black); phospholipid:sterol (green); sterol:sterol (red); and sterol:water (purple). We used a distance cutoff of 2.4 Å between the donor oxygen and acceptor hydrogen atoms to define a hydrogen bond. We also consider the formation of salt bridges between phospholipid molecules. In the blue line we counted the number of salt bridges formed between choline and phosphate of two different phospholipid molecules. A salt bridge is assumed to form when the distance between a nonester oxygen of the phosphate and the carbon of the choline was less than 4 Å.

4.8 Discussion

The purpose of this work was to elucidate the effect of cholesterol and an analogue sterol, 6-ketocholestanol, on the magnitude of the membrane's electric field. In our experiments, we determined that cholesterol and 6-kc increased the membrane electric field at lower concentrations, whereas at higher concentrations, they had opposite effects; cholesterol lowered the magnitude of the field and 6-kc increased the magnitude of the field. Sterols can impact the membrane's field in two ways: (1) directly through the

inclusion of its own molecular dipole moment (~2.01 D for cholesterol and ~4 D for 6-kc)[3] into the system of ordered dipoles; or (2) indirectly by inducing changes in the membrane's physical properties including fluidity, stiffness, and packing.[4-8] We reported different organization of cholesterol and 6-kc near each other and the helix. This organization alters the electric field that the probe, which is attached to the helix, experiences when the concentration and/or type of sterol are modified.

The intercalation of cholesterol into a lipid bilayer membrane induces ordering in the alkyl chains of lipid membranes,[23-24] increasing membrane density,[25-28] decreasing fluidity,[29-30] and increasing mechanical strength.[31] One of the most widely observed impacts of cholesterol in lipid membranes is its condensing effect because of the nonideal interaction of cholesterol with phospholipids.[32] Cholesterol participates in hydrogen bonding with water molecules and other phospholipids through a polar hydroxyl group or via water bridges with adjacent phospholipids, thus anchoring itself to the membrane−aqueous interface. Molecular simulations have shown that upon incorporation of cholesterol into the pure lipid bilayer, there is a decrease in the formation of gauche rotamers in the lipid alkyl chains and a substantial reduction in the average tilt of the lipid chains with respect to the plane of the membrane bilayer.[8] These two structural effects straighten the hydrocarbon tails of the lipid, which in turn increases the packing density of the lipid molecules and condenses the area per molecule.[8, 25-26, 33] 6-kc, on the other hand, is known to increase the membrane permeability and does not impact the ordering of the alkyl tails.[34-35] The additional ketone group on the second ring structure allows 6-kc to hydrogen bond to greater number of water molecules, thus influencing hydration levels at the membrane−water interface.

With no sterol, the lipid bilayer above the transition temperature is in a fluid-like disordered phase and has a membrane electric field of 10.3 MV/cm.[15] Upon incorporation

of a small amount of sterol up to ~10 mol% into the bilayer, the membrane field increases for both sterols. At this low concentration, according to our simulations, the sterols are more concentrated near the helix while at higher concentrations their distribution is more uniform (Figure 4.9). The sterol coverage of the first solvation shell around the helix is frequently incomplete. Slightly more ordered lipid molecules replace missing sterol molecules in the helix solvation shell resulting in a stronger local electric field at the probe. As the concentration of 6-kc increases from 10 to 40 mol%, phospholipid dipole ordering increases and the electric field near the boundary of the layer increases, consistent with the experimental observation.

We considered three hypotheses for the origin of the monotonic increase in the measured and computed electric fields caused by 6-kc as a function of its concentration. The first hypothesis points to the enhanced ordering of the lipid headgroup dipole moments. The changes in the field are significant especially between the 40% 6-kc dipoles and the rest of the bilayer. The second hypothesis is the direct contribution of the additional carbonyl group of 6-kc to the electric field. Finally the third hypothesis proposes that the water molecules that are hydrogen bonded to the extra carbonyl in 6-kc cause an increase in the electric field. Indeed the water contribution shows a decrease in the electric field for cholesterol. Smaller changes are observed for 6-kc.

This phenomena is exhibited by the broad distribution of helix tilt angle of αLAX(16) shown in Figure 4.8. The helix itself is also homogeneously distributed in both bilayers, thus probing the greater electric field coming from the increased dipole density at the membrane−water interface from the phospholipid as well as the water molecules hydrogen bound to each phospholipid headgroup in bilayers. The homogeneous distribution of helix in bilayers containing both type of sterols is indicated by the similar RDF plots of helix-sterol separation shown in Figure 4.9 for 10 mol% cholesterol and 10

mol% 6-kc. Hence, at 10 mol% sterol, the elevated packing of phospholipids, sterols, and water molecules in a bilayer collectively increases the dipole density at the membrane−water interface and is directly reported by the helix, which is also homogeneously distributed throughout the bilayer.

At high sterol concentration, 40 mol%, the distribution of phospholipids, sterols, and the helix are different for cholesterol and 6-kc. In the case of cholesterol-containing bilayers, cholesterol forms small clusters distributed throughout the bilayer. The multiple prominent peaks in the RDF of sterol−sterol interactions at 40 mol% cholesterol (shown in Figure 4.10b) suggest a long-range distribucmation of such clusters. The nitrile-containing helix is distributed homogeneously among the phospholipids and these cholesterol-rich clusters. This hypothesis is supported by two of our results: (1) the RDF plot of helix-sterol at 40 mol% cholesterol in Figure 4.9; and (2) the experimental fwhm of the absorption peak of the nitrile in αLAX(16) in Figure 4.6, which is significantly larger at 40 mol% cholesterol. The greater fwhm values can be explained if the nitrile is positioned in two chemically heterogeneous domains: one enriched in phospholipids with ordered tails, and the other enriched in cholesterol. In this environment, the relative concentration of cholesterol increases in comparison to phospholipids. As cholesterol molecules displace phospholipids, the water molecules associated with those phospholipids through hydrogen bonding are displaced as well. The intrinsic dipole moment of cholesterol is 2.01 D, which is significantly smaller than the molecular dipole moment of a DMPC phospholipid (∼14 D), particularly when it is decorated with hydrogen-bound water molecules.[2] The nitrile, which is distributed among the phospholipids and cholesterol clusters, therefore directly reports the net reduction in the dipole density by the small magnitude of the absorption energy shift and thus the smaller electric field.

In the case of membranes containing high concentrations of 6-kc, the sterol segregates into larger clusters of 6-kc compared to cholesterol. The single prominent peak in the RDF plot of 40 mol% 6-kc in Figure 4.10b provides strong evidence of such cluster formation. The RDF plot of helix-sterol in Figure 4.9 clearly suggests greater separation between helix and the 6-kc clusters. Furthermore, in contrast to cholesterol, we do not observe significant differences in the fwhm of the nitrile in αLAX(16) at 40 mol% 6-kc versus 10 mol% 6-kc (Figure 4.6). This implies that the nitrile is continuously placed within the same phospholipid tail region at all concentrations of 6-kc. As the concentration of 6-kc increases, so do the magnitudes of the contributed dipole moments from the sterol (~4 D) and associated water molecules.[2] This effect is larger than that seen for cholesterol because of the extra hydrogen bond acceptor oxygen atom on 6-kc. This is verified by the quantitative hydrogen bond analysis between sterol and water molecules (Figure 4.11), in which the number of hydrogen bonds associated with 6-kc is larger than with cholesterol. This leaves the helix surrounded by phospholipids, but sequestered from 6-kc.

At mid range concentrations we show an opposite behavior of the electric field for 6-kc and cholesterol in both experiment and simulations. The electric field decreases as the concentration of cholesterol increases while it increases for 6-kc. This surprising difference between two similar sterols can be rationalized by their relative positions in the membrane. Cholesterol is placed deeper in the membrane and is unlikely to orient the water dipoles successfully. This task is conducted effectively by 6-kc, whose capacity for an additional hydrogen bond places it closer to the interface between the aqueous solution and the membrane[35] (the electric field contribution of water is similar between the two sterols). Our results shed light on sometimes conflicting results about the effect of sterols, particularly cholesterol, on membrane electrostatics. We show that the effect of

cholesterol on the electric field is divided into two regimes based on its concentration. At low concentration, the simulations results are too noisy to obtain significant signal, but experiments suggest that the electric field is increasing. At high concentration, cholesterol reduces the polar environment near the helical probe and therefore reduces the electric field. 6-kc is susceptible to forming a greater number of hydrogen bonds with water molecules compared to cholesterol, and the dipole density at the membrane−water interface increases with the increasing 6-kc mole fraction due to its larger intrinsic dipole moment.

4.9 CONCLUSION

It is well known that the noncovalent intercalation of cholesterol into biological membranes has a great impact on membrane fluidity, self-association, and function. Despite extensive experimental and theoretical investigations, there is limited agreement on how and to what extent cholesterol and other sterols, such as 6-kc, alter membrane electrostatics, largely the result of limited techniques for studying a property contained entirely within membrane interior. By addressing this with VSE spectroscopy and MD simulations, we measured changes in electric field as a function of sterol concentration and identity. We used MD simulations to identify distinct patterns of lateral organization of sterols inside the lipid bilayer especially at higher sterol concentration. Future work in this laboratory will focus on how this electrostatic field regulates significantly more complex lipid membrane mechanisms, such as binding of membrane-proteins and ion channel formations.

4.10 REFERENCES

1. Efimova, S. S.; Ostroumova, O. S. Effect of Dipole Modifiers on the Magnitude of the Dipole Potential of Sterol-Containing Bilayers. *Langmuir* **2012,** *28*, 9908-9914.

2. Haldar, S.; Kanaparthi, R. K.; Samanta, A.; Chattopadhyay, A. Differential Effect of Cholesterol and its Biosynthetic Precursors on Membrane Dipole Potential. *Biophys. J.* **2012,** *102*, 1561-1569.

3. Starke-Peterkovic, T.; Turner, N.; Vitha, M. F.; Waller, M. P.; Hibbs, D. E.; Clarke, R. J. Cholesterol Effect on the Dipole Potential of Lipid Membranes. *Biophys. J.* **2006,** *90*, 4060-4070.

4. Szabo, G. Dual Mechanism for the Action of Cholesterol on Membrane Permeability. *Nature* **1974,** *252*, 47-49.

5. Hofsäss, C.; Lindahl, E.; Edholm, O. Molecular Dynamics Simulations of Phospholipid Bilayers with Cholesterol. *Biophys. J.* **2003,** *84*, 2192-2206.

6. Chiu, S. W.; Jakobsson, E.; Scott, H. L. Combined Monte Carlo and Molecular Dynamics Simulation of Hydrated Dipalmitoyl–Phosphatidylcholine–Cholesterol Lipid Bilayers. *J. Chem. Phys.* **2001,** *114*, 5435-5443.

7. Smondyrev, A. M.; Berkowitz, M. L. Structure of Dipalmitoylphosphatidylcholine/Cholesterol Bilayer at Low and High Cholesterol Concentrations: Molecular Dynamics Simulation. *Biophys. J.* **1999,** *77*, 2075-2089.

8. Gabdoulline, R. R.; Vanderkooi, G.; Zheng, C. Comparison of the Structures of Dimyristoylphosphatidylcholine in the Presence and Absence of Cholesterol by Molecular Dynamics Simulations. *J. Phys. Chem.* **1996,** *100*, 15942-15946.

9. McIntosh, T. J.; Magid, A. D.; Simon, S. A. Cholesterol Modifies the Short-Range Repulsive Interactions Between Phosphatidylcholine Membranes. *Biochemistry* **1989,** *28*, 17-25.

10. Yang, Y.; Mayer, K. M.; Wickremasinghe, N. S.; Hafner, J. H. Probing the Lipid Membrane Dipole Potential by Atomic Force Microscopy. *Biophys. J.* **2008,** *95*, 5193-5199.

11. Franklin, J. C.; Cafiso, D. S. Internal Electrostatic Potentials in Bilayers: Measuring and Controlling Dipole Potentials in Lipid Vesicles. *Biophys. J.* **1993,** *65*, 289-299.

12. Gross, E.; Bedlack, R. S., Jr.; Loew, L. M. Dual-Wavelength Ratiometric Fluorescence Measurement of the Membrane Dipole Potential. *Biophys. J.* **1994,** *67*, 208-216.

13. Smondyrev, A. M.; Berkowitz, M. L. Effects of Oxygenated Sterol on Phospholipid Bilayer Properties: A Molecular Dynamics Simulation. *Chem. Phys. Lipids* **2001,** *112*, 31-39.

14. Hu, W.; Webb, L. J. Direct Measurement of the Membrane Dipole Field in Bicelles Using Vibrational Stark Effect Spectroscopy. *J. Phys. Chem. Lett.* **2011,** *2*, 1925-1930.

15. Shrestha, R.; Cardenas, A. E.; Elber, R.; Webb, L. J. Measurement of the Membrane Dipole Electric Field in DMPC Vesicles Using Vibrational Shifts of p-Cyanophenylalanine and Molecular Dynamics Simulations. *J. Phys. Chem. B* **2015,** *119*, 2869-2876.

16. Andrews, S. S.; Boxer, S. G. Vibrational Stark Effects of Nitriles I. Methods and Experimental Results. *J. Phys. Chem. A* **2000,** *104*, 11853-11863.

17. Andrews, S. S.; Boxer, S. G. Vibrational Stark Effects of Nitriles II. Physical Origins of Stark Effects from Experiment and Perturbation Models. *J. Phys. Chem. A* **2002,** *106*, 469-477.

18. Johansson, A. C. V.; Lindahl, E. Amino-Acid Solvation Structure in Transmembrane Helices from Molecular Dynamics Simulations. *Biophys. J.* **2006,** *91*, 4450-4463.

19. Duffin, R. L.; Garrett, M. P.; Busath, D. D. Modulation of Lipid Bilayer Interfacial Dipole Potential by Phloretin, RH421, and 6-Ketocholestanol as Probed by Gramicidin Channel Conductance. *Langmuir* **2003,** *19*, 3561-3561.

20. Simon, S. A.; McIntosh, T. J.; Magid, A. D.; Needham, D. Modulation of the Interbilayer Hydration Pressure by the Addition of Dipoles at the Hydrocarbon/Water Interface. *Biophys. J.* **1992,** *61*, 786-799.

21. Honig, B. H.; Hubbell, W. L.; Flewelling, R. F. Electrostatic Interactions in Membranes and Proteins. *Annu. Rev. Biophys. Biophys. Chem.* **1986,** *15*, 163-193.

22. Cevc, G. Membrane Electrostatics. *Biochim. Biophys. Acta, Rev. Biomembr.* **1990,** *1031*, 311-382.

23. Kučerka, N.; Nieh, M.-P.; Katsaras, J. Fluid Phase Lipid Areas and Bilayer Thicknesses of Commonly Used Phosphatidylcholines as a Function of Temperature. *Biochim. Biophys. Acta, Biomembr.* **2011,** *1808*, 2761-2771.

24. Khelashvili, G.; Pabst, G.; Harries, D. Cholesterol Orientation and Tilt Modulus in DMPC Bilayers. *J. Phys. Chem. B* **2010,** *114*, 7524-7534.

25. Róg, T.; Pasenkiewicz-Gierula, M. Cholesterol Effects on the Phosphatidylcholine Bilayer Nonpolar Region: A Molecular Simulation Study. *Biophys. J.* **2001,** *81*, 2190-2202.

26. Jedlovszky, P.; Mezei, M. Effect of Cholesterol on the Properties of Phospholipid Membranes. 1. Structural Features. *J. Phys. Chem. B* **2003,** *107*, 5311-5321.

27. Henriksen, J.; Rowat, A. C.; Brief, E.; Hsueh, Y. W.; Thewalt, J. L.; Zuckermann, M. J.; Ipsen, J. H. Universal Behavior of Membranes with Sterols. *Biophys. J.* **2006,** *90*, 1639-1649.

28. Smaby, J. M.; Momsen, M. M.; Brockman, H. L.; Brown, R. E. Phosphatidylcholine Acyl Unsaturation Modulates the Decrease in Interfacial Elasticity Induced by Cholesterol. *Biophys. J.* **1997,** *73*, 1492-1505.

29. Marsh, D. An Interacting Spin Label Study of Lateral Expansion in Dipalmitoyllecithin-Cholesterol Bilayers. *Biochim. Biophys. Acta, Biomembr.* **1974,** *363*, 373-386.

30. Kusumi, A.; Tsuda, M.; Akino, T.; Ohnishi, S.; Terayama, Y. Protein-Phospholipid-Cholesterol Interaction in the Photolysis of Invertebrate Rhodopsin. *Biochemistry* **1983,** *22*, 1165-1170.

31. Mouritsen, O. G.; Jørgensen, K. Dynamical Order and Disorder in Lipid Bilayers. *Chem. Phys. Lipids* **1994,** *73*, 3-25.

32. McConnell, H. M.; Radhakrishnan, A. Condensed Complexes of Cholesterol and Phospholipids. *Biochim. Biophys. Acta, Biomembr.* **2003,** *1610*, 159-173.

33. Rheinstädter, M. C.; Mouritsen, O. G. Small-Scale Structure in Fluid Cholesterol–Lipid Bilayers. *Curr. Opin. Colloid Interface Sci.* **2013,** *18*, 440-447.

34. Buzón, V.; Cladera, J. Effect of Cholesterol on the Interaction of the HIV GP41 Fusion Peptide with Model Membranes. Importance of the Membrane Dipole Potential. *Biochemistry* **2006,** *45*, 15768-15775.

35. Auner, B. G.; O'Neill, M. A.; Valenta, C.; Hadgraft, J. Interaction of Phloretin and 6-Ketocholestanol with DPPC-Liposomes as Phospholipid Model Membranes. *Int. J. Pharm.* **2005,** *294*, 149-155.

Chapter 5: Preferential Partitioning of Positively Charged Tryptophan in Phosphatidylcholine Lipid Bilayer

5.1 Publication Note

Portions of the methods outlined in this section were adapted from the following publication:

Anderson, C. M.; Cardenas, A. E.; Elber, R.; Webb, L. J. Preferential Equilibrium Partitioning of Positively Charged Tryptophan into Phosphocholine Bilayer Membranes. *J. Phys. Chem. B* **2019,** *123,* 170-179. [C. M. Anderson performed all experimental measurements, including vesicle formation, infrared and fluorescence spectroscopic measurements and fluorescence quenching. A. E. Cardenas performed all molecular dynamics simulations.]

5.2 Introduction

One of the most important functions of the biological lipid bilayer membrane is to act as a barrier that selectively admits and excludes certain molecules based on the needs of the cell. Understanding how this occurs in the absence of protein machinery that has evolved to transport particular atoms or molecules across the bilayer is particularly important for several reasons. First, it is hypothesized that primordial cells existed for a significant period of time before the selective macromolecular machinery that aids in these processes evolved. Understanding the mechanisms of how primitive membranes could selectively transport beneficial molecules, such as nutrients, into the cell or waste out of the cell, while at the same time excluding toxic molecules, is essential for understanding this period of cellular evolution.[1-4] Second, therapeutic molecules introduced to an organism must eventually find their way to their target, which often means crossing a cellular membrane without a dedicated protein channel.[5] While the

pharmaceutical industry has developed a range of empirical tools for guiding the design of molecules that will be effective in this regard,[6-9] understanding molecular-level mechanisms for this process would be beneficial in providing more quantitative guidance for drug design. Finally, any detailed understanding of molecular-level mechanisms of membrane behavior must include the ability to quantitatively model the membrane *a priori*, and understanding a process as simple as the transport of a molecule across that membrane must be adequately modeled by any level of theory which seeks to be acceptable to membrane researchers. For this reason, detailed investigations into the transport of small molecules across a lipid bilayer membrane are necessary. Permeability experiments and molecular dynamic (MD) simulations have been performed for a range of solute molecules through a variety of lipid bilayers to compare how charge,[10] size,[11] and hydrophobicity[12-14] of molecules affect the ability to permeate a lipid bilayer membrane.[15]

This subject is of increased recent interest, in part, because of cell penetrating peptides (CPPs),[16-20] short (15−30 amino acids) peptides that carry large positive charges and penetrate the lipid bilayer through mechanisms that are still under investigation.[17-18, 20] We have previously studied how changing the charge on the amino acid tryptophan, controlled by changing the protonation state of the backbone N and C termini through solution pH, affected the rate at which the charged amino acid permeated a zwitterionic phosphatidylcholine lipid bilayer.[21] Results from our previously published work demonstrated that positively charged tryptophan (Trp+, in which the carboxyl terminal of the tryptophan is protonated) permeated 120 nm diameter vesicles composed of 1,2-dioleoyl-sn-glycero-3-phosphocholine (DOPC) at a faster rate than the negatively charged tryptophan (Trp−, in which the N terminal of the tryptophan is unprotonated) by a factor of approximately 108. Complementary MD simulations revealed that Trp+ also

had a potential of mean force (PMF) barrier that was approximately 15 kcal mol^{-1} lower than that of Trp−. These experiments were conducted by spiking a solution of DOPC vesicles with a high concentration of the charged amino acid, then separating vesicles from solution through size exclusion chromatography over the time course of the experiment, and quantifying the amount of the charged tryptophan associated with the vesicle through fluorescence spectroscopy. We followed the association of the amino acid with the vesicle until no further changes in concentration were measured; this occurred after 4 h, but we confirmed there were no changes between 4 h and up to 1 week (at which point vesicles began to aggregate). In addition to faster interactions with the lipid vesicle, we also measured differences in the concentration of Trp+ and Trp− associated with the vesicle at equilibrium. These previous experiments were designed to test solely for permeation of the amino acid through the lipid bilayer and assumed that any tryptophan associated with the vesicle after the size exclusion column separation had been transported from outside to inside the vesicle.

Our experiments did not distinguish between tryptophan that permeated through the lipid bilayer from tryptophan that simply partitioned into the membrane and remained within the bilayer at equilibrium. However, in transmembrane proteins, tryptophan is commonly found at the membrane/water interface where it appears to serve a role of anchoring the protein within the bilayer, facilitated by the structure of the amino acid.[22-31]

Tryptophan's hydrophobic indole ring orients in a position to be buried in the hydrophobic core of the lipid bilayer, whereas the polar amide backbone favors the lipid near-surface and headgroup region of the membrane. Because of this, tryptophan residues in transmembrane proteins are commonly found at the interfacial region, usually on the extracellular side of the membrane, but rarely at the center of the bilayer.[28,32-33] This is

seen, for example, in gramicidin A (1GRM),[34] OmpF (20MF),[35] and the photosynthetic reaction center (1PRC).[36]

To determine whether charged tryptophan remains within the lipid bilayer at equilibrium or fully penetrates the membrane to the solvated vesicle interior, we focused on measuring changes in the fluorescence energy of the tryptophan side chain as a function of time from an initial triggering event. The absorption and emission energy of tryptophan is sensitive to its environment,[37-38] a property that has been used extensively to determine the extent of hydration of tryptophan in a variety of biological contexts.[39-40] As shown in Figure 5.1, when dissolved in a hydrophobic solvent, such as hexanes, the maximum of the emission energy (λ_{max}) of tryptophan is ~340 nm; this shifts to 380 nm when the amino acid is dissolved in water. The shift to lower emission energy in water versus a hydrophobic solvent is caused by the increased reaction field imposed on tryptophan in the high dielectric solvent, which stabilizes the excited state dipole moment of the molecule and lowers the transition energy.[38-39] When a solution of DOPC vesicles is spiked with tryptophan, the measurement of the fluorescence energy is a straightforward method to determine if tryptophan remains fully solvated (either outside or inside the vesicle) or is associated in some way with the more hydrophobic region of the interior of the bilayer, where the dielectric constant would be lower. As our system of vesicle-associated tryptophan is moved from one equilibrium condition to another, the fluorescence energy of the amino acid is a convenient tool for determining whether it is solvated in an aqueous or hydrophobic (i.e., lipid) environment.[37]

In order to determine where tryptophan resides within the membrane at equilibrium, it is also possible to add a fluorescence quencher to the structure of the bilayer itself by making vesicles containing 10−30 mol % of brominated DOPC lipids.[41-43] Bromine acts as a dynamic quencher for tryptophan that promotes intersystem crossing

from the initial electronic excited state to a triplet state. Due to the slow emission from a triplet state, other collisional processes occur at a faster rate, resulting in quenching of the emission.[44] In previous studies, this property has been used to determine peptide and protein insertion depth within the membrane by changing the position of the Br along the fatty acid tail of the lipid and then measuring the extent of tryptophan quenching based on its proximity to the Br.[41, 45-47]

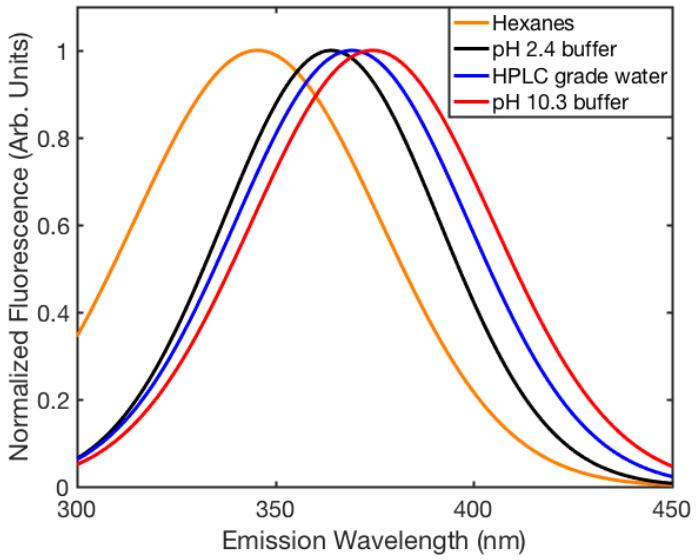

Figure 5.1: Tryptophan's emission spectra in different solvents: hexanes (orange); pH 2.4 buffer (black); HPLC grade water (blue); and pH 10.3 buffer (red).

In our previous work,[21] MD simulations and free energy calculations were performed on DOPC lipid bilayers, in which Trp+ and Trp− were moved from the fully solvated aqueous exterior to the middle of the membrane. The free energy calculations suggested that the glycerol backbone region is a favorable location for Trp+ to reside, similar to what is observed in pdb structures of tryptophan-containing transmembrane proteins. In contrast, Trp− experienced a slight decrease in free energy in moving from

bulk water to the lipid phosphate group, but was positioned near the lipid headgroup where it remained largely solvated. These calculations suggested that the lowest free energy position for Trp+ *versus* Trp− differed by at least 4 Å, a significant distance in a fluorescence quenching experiment. For those reasons, we have made DOPC vesicles that incorporated 30 mol% brominated phosphocholine lipids (Br-PC) with bromine at positions 4 and 5 along the lipid tail, shown in Figure 5.2. The extent of quenching of tryptophan fluorescence was then a direct measurement of the extent of tryptophan partitioning into the lipid bilayer at equilibrium, and the role of the tryptophan charge in this process could be easily measured. We calculated the amount of quenching at each time point to track the migration of tryptophan from the glycerol backbone region to the bulk solution. When paired with the analysis of fluorescence emission spectra of tryptophan, this is a straightforward measurement for determining the extent of tryptophan partitioning in the lipid bilayer membrane.

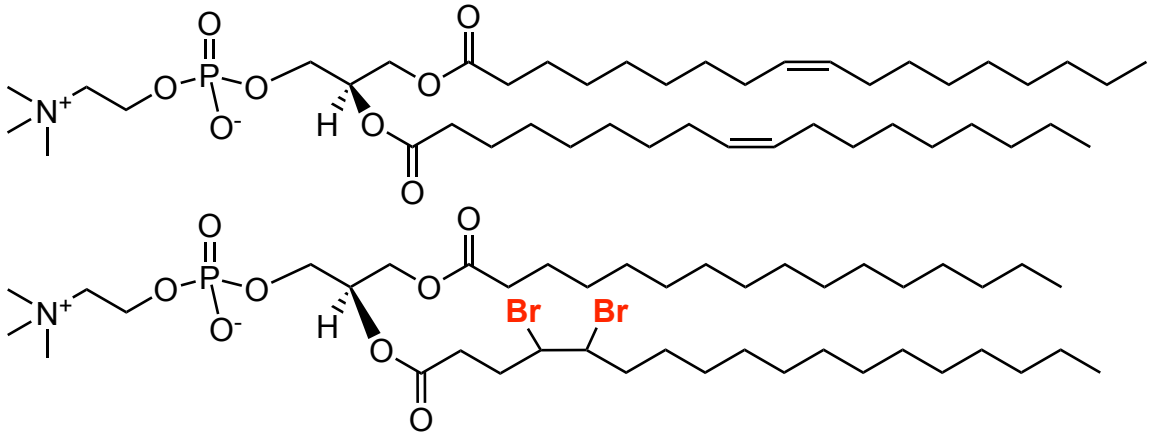

Figure 5.2: 1,2-dioleoyl-sn-glycero-3-phosphocholine (DOPC, top) and 1-palmitoyl-2-stearoyl(4,5)dibromo-sn-glycero-3-phosphocholine (Br-PC, bottom).

The work described here differentiates between permeation across the lipid bilayer and partitioning into the bilayer structure itself for both positively and negatively

charged tryptophan. Vesicles containing a fraction of Br-PC were incubated with excess Trp+ (pH 2.4) or Trp− (pH 10.3). After equilibration, vesicles were removed from the tryptophan-containing solution by size exclusion chromatography, and the fluorescence spectrum of tryptophan was monitored until the system returned to equilibrium, approximately 4 h. Changes in fluorescence energy and intensity were both related to the position of the amino acid in the bilayer/ water system. We find that tryptophan does not permeate the membrane but actually partitions into the lipid bilayer structure, where it remains at equilibrium. Furthermore, we demonstrated that the concentration of Trp+ within the bilayer at equilibrium is 5 times higher than that of Trp−. Both experiment and simulations suggest that tryptophan resides near the glycerol linkage of the DOPC lipid, where it likely is stabilized by multiple electrostatic and hydrogen bonding interactions in the near-surface region of the membrane.

5.3 METHODS

Vesicles composed of 100 mol% DOPC lipids or a 70:30 mol% ratio of DOPC:Br-PC lipids used for these experiments were formed using the extrusion method described in Section 2.3.2. Vesicles were hydrated with either a citric acid buffer at pH 2.4 or sodium carbonate and sodium bicarbonate buffer at pH 10.3. 10 mM tryptophan solutions were also made in the corresponding buffers, which allowed us to control the charge of tryptophan in solution.

The prepared 30 mM lipid vesicle solutions and 10 mM tryptophan stock solutions (with the same buffer) were mixed in a 1:3 (v/v) ratio. This mixture was allowed to sit for 4-6 hours, at which time tryptophan had reached equilibrium between the bulk solution and interacting with the lipid bilayer vesicles. A 400 μL aliquot of the mixture was then taken and passed through a PD-10 column, once the solution had

completely entered the column, 2100 µL of the appropriate buffer was passed through the column to fill the column's volume. Following the uptake of the excess buffer, 3500 µL of the same buffer was used to elute the column and this elution was collected for fluorescence measurements.

Immediately following column elution fluorescence spectra were collected on the vesicle solution every 10−20 min for 4 h using a Fluorolog3 fluorimeter by exciting at 280 nm and collecting spectra from 300 to 450 nm in 1 nm increments. A 5 mm quartz cuvette (Starna Cells) was used for all samples.

To observe changes in tryptophan's environment over time, all of the fluorescence emission spectra, *F(x)*, were fit to a sum of two Gaussians, I_i, described in equation 5-1 as I_{lip} and I_{wat}

$$F(x) = I_{lip} + I_{wat} = a_{lip}[e^{-\left(\frac{x-b_{lip}}{c_{lip}}\right)^2}] + a_{wat}\left[e^{-\left(\frac{x-b_{wat}}{c_{wat}}\right)^2}\right] \quad \text{(Equation 5-1)}$$

where the subscripts *lip* and *wat* are representative of the environment of tryptophan in the lipid (I_{lip}) and water (I_{wat}) environment, respectively; a is a scaling factor; b_i is the λ_{max} of I_i; c is the variance of I_i; and x is the emission wavelength. These experiments were performed for samples at pH 2.4 and pH 10.3 for solutions with vesicles composed of 100 mol % DOPC and 70:30 mol% DOPC:Br-PC.

5.4 FTIR Phase Transitions

To ensure that all of our vesicle solutions were consistent in size and shape, and that the phospholipids are in the liquid phase at room temperature, we used a rigorous characterization process, described in the Materials and Methods chapter. Because there has been no report on whether the gel-to-liquid phase transition temperature (T_m) of the system changed either as a function of the addition of the Br-PC lipid or by the change in

pH, we used FTIR spectroscopy to ensure that the lipid tails were in the liquid disordered phase at room temperature for all of the samples we used in our experiments.[48] In Figure 5.3, we show FTIR spectra of the $-CH_2$ symmetric stretch at ~2853 cm^{-1} for temperatures ranging from 5 (red) to 60 °C (pink) for vesicles composed of 70:30 DOPC:Br-PC lipids at pH 2.4 and pH 10.3 in panels a and b, respectively. Because pure DOPC lipid vesicles have a known T_m of −20 °C at a neutral pH, we used a smaller temperature range of 5 (red) to 35 °C (pink) for the pure DOPC lipid vesicles at pH 2.4 and 10.3 in panels c and d, respectively. We observed a 0.5 cm^{-1} shift of the $-CH_2$ stretch from 2852.3 to 2852.8 cm^{-1} between 10 and 15 °C for the 70:30 DOPC:Br- PC lipid vesicles at both pH 2.4 and pH 10.3, indicative of a phase transition of the lipid tails. There were no further shifts detected from 15 to 60 °C, and no differences between pH 2.4 and 10.3 were detected. We conclude that at the temperatures at which our experiments were conducted, vesicles composed of both pure DOPC and 70:30 DOPC:Br-PC are in the liquid phase and well mixed.

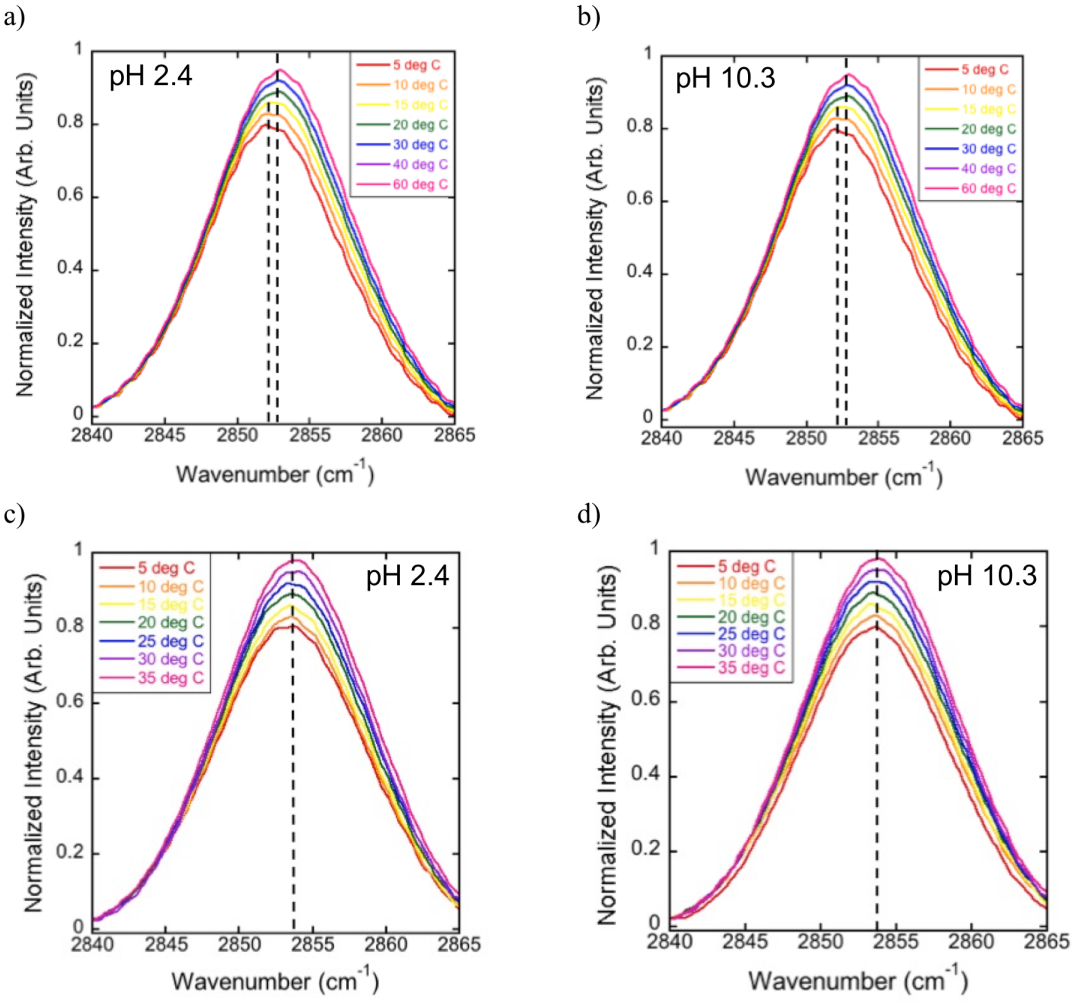

Figure 5.3: Fourier-transformed infrared (FTIR) normalized spectra of the -CH_2 symmetric stretch at ~2853 cm^{-1} for vesicles used in the experiments. Spectra were collected at temperatures ranging from 5 °C (red) to 60 °C (pink) for 70:30 DOPC:Br-PC lipid vesicles and from 5 °C (red) to 35 °C (pink) for pure DOPC lipid vesicles. The dashed black lines illustrate the spectra maxima. **a:** 70:30 DOPC:Br-PC lipid vesicles, pH 2.4; **b:** 70:30 DOPC:Br-PC lipid vesicles, pH 10.3; **c:** pure DOPC lipid vesicles, pH 2.4; **d:** pure DOPC lipid vesicles, pH 10.3

5.5 FLUORESCENCE SPECTROSCOPY

In Figure 5.1, we show the normalized emission spectra of tryptophan dissolved in the two buffers used in this study, pH 2.4 (Trp+, black) and pH 10.3 (Trp−, red). There was a slight difference in fluorescence energy in these two buffers, with tryptophan emitting at 362 nm in the pH 2.4 buffer and at 370 nm in the pH 10.3 buffer. This is important for two reasons. (1) To quantify the extent of charged tryptophan partitioning into the lipid bilayer membrane, it was necessary to prepare a calibration curve for each buffer. More importantly, (2) if tryptophan moved from the lipid interior, characterized by an emission energy near 340 nm (similar to that when dissolved in hexanes in Figure 5.1, orange), this would cause a large decrease in emission energy as tryptophan moved to the hydrophilic, aqueous environment. Therefore, changes in the absolute value of emission energy, as well as intensity, can be used to infer the local environment of each tryptophan at equilibrium and differences in the extent of equilibrium for Trp+ versus Trp−.

To determine a more exact location of tryptophan in the lipid bilayer at the time of elution from the column, we used fluorescence quenching with the Br-PC lipids shown in Figure 5.2, where the Br atoms are located close to the glycerol backbone region without disrupting the structure of the lipid. Representative emission spectra of tryptophan are shown in Figure 5.4, fitted to the sum of two Gaussians, as described by eq 1, at times of 10 min (blue), 1 h (green), and 4 h (red) after the sample was eluted from the size exclusion column for Trp+ (pH 2.4) and Trp− (pH 10.3). Representative raw data are also shown for the 10 min time point (blue dots) to demonstrate that our fitting procedure in eq 1 was able to accurately represent our raw data well. Solid lines depict spectra collected from pure DOPC lipid vesicles, while dashed lines are those of samples that contained 70:30 DOPC:Br-PC lipid vesicles. With our experimental design, 0 min

was defined as the start of the column elution; at this time, the only tryptophan present in the sample was associated in some way with the vesicle in order to be collected by size exclusion chromatography. Although we measured fluorescence spectra up to 24 h after vesicles were removed from the spiked tryptophan solution, no further changes were observed after 4 h, and so we only show data up to 4 h here. It is important to note that the data shown in Figure 5.4 are unnormalized spectra. The amount of tryptophan present in each sample was determined by comparing the 4 h time point data (when the majority of the tryptophan was in the bulk solution) to calibration curves created for Trp+ and Trp− in the respective buffer solutions. Due to the differences in the calibration curves for Trp+ and Trp−, the intensities of the pH 2.4 and pH 10.3 data cannot be directly compared to one another. At the time of column elution, there was 5 times more Trp+ than Trp− in the samples. We will comment on this further in the discussion. There are four observations to address in Figure 5.4: (1) the fluorescence emission spectra of tryptophan red-shift over time, but in ways that are significantly different for Trp+ versus Trp−; (2) the amount of fluorescence quenching of Trp+ at short time points is significantly greater compared to Trp−; (3) the total loss of fluorescence quenching over time is significantly different for Trp+ versus Trp−; and (4) there is an overall loss of fluorescence intensity over time, but to a greater degree for Trp+ compared to Trp−. These observations are discussed below.

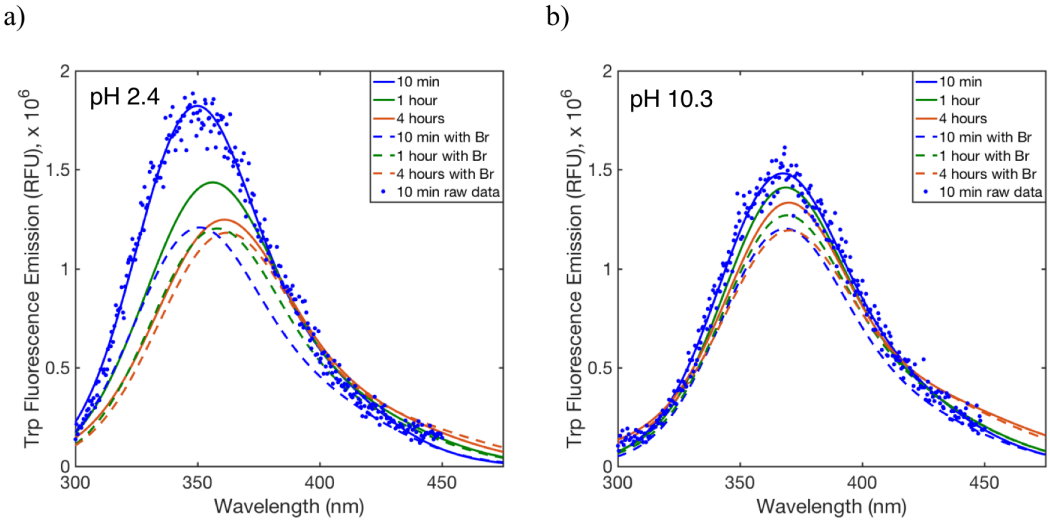

Figure 5.4: Representative spectra from selected time points for DOPC vesicles both with (dashed lines) and without (solid lines) Br-DOPC lipids. Spectra are shown at 10 min (blue), 1 hr (green), and 4 hr (red) after tryptophan-containing vesicles were re-equilibrated in a buffer without tryptophan. Filled circles show representative raw data from the 10 min time point as an example. **a**: Spectra collected at pH 2.4 (Trp+); **b**: Spectra collected at pH 10.3 (Trp-).

Figure 5.4 shows that the emission spectra of both positively and negatively charged tryptophan shifted to lower energy over the 4 h of observation time; however, the shift was significantly larger for Trp+ than Trp−. At pH 2.4 with Trp+ (Figure 5.4a), there was a 12 nm shift in λ_{max} from 350 nm at 10 min to 362 nm at 4 h. In contrast, at pH 10.3 with Trp− (Figure 5.4b), the initial fluorescence energy measured 10 min after column separation was 368 nm, and shifted only to 370 nm over 4 h of observation. The significant blue shift shown by Trp+ 10 min after equilibration compared to Trp− demonstrates that significantly more Trp+ was exposed to a more hydrophobic environment at this initial time point, indicating that the equilibrium position for Trp+ in the tryptophan-spiked buffer was residing inside the membrane bilayer structure. Trp−

was associated with the lipid bilayer at the time of column elution, but the lack of blue-shifting in the emission spectra tells us that it was further from the hydrophobic core and was closer to the water interface. At both pH values, after 4 h, the measured λ_{max} was equal to that of tryptophan in each respective buffer (shown in Figure 5.1), indicating that after 4 h of equilibration in buffer, essentially all tryptophan was solvated in bulk solution rather than associated with the lipid bilayer.

A second observation in Figure 5.4 is that the amount of tryptophan fluorescence quenching in the presence of 30 mol% Br-PC lipids (dashed lines) was significantly different for the positively and negatively charged molecule, with Trp+ showing significantly more quenching when exposed to the Br-PC lipids at short equilibration times. To compare the fluorescence emission spectra of Trp+ and Trp− in the absence and presence of the 30 mol% Br-PC lipids at each time point shown in Figure 5.4, we calculated the percentage of fluorescence quenching by determining λ_{max} for each of the fitted spectra in Figure 5.4, then divided the λ_{max} of F(x) of the 70:30 DOPC:Br-PC vesicle samples by the λ_{max} of F(x) of the pure DOPC vesicle sample from the same pH and time point. As previously stated, there are different amounts of Trp+ and Trp− associated with the vesicles at the time of elution. The calculated percentages of quenching are relative to the amount of Trp+ or Trp− present in the sample at the time of elution. As shown in Figure 5.4 and Table 5.1, when the first time point was collected at 10 min, 34% of the Trp+ contained in the sample was quenched, compared to only 18% of Trp−. This indicates that more Trp+ was present within the structure of the lipid bilayer and near enough to the Br to be quenched, while any Trp− in the sample was located further away from the Br atoms and less significantly affected by the quenching Br atoms. Because only 30 mol% of the lipids were Br-PC (and therefore capable of quenching tryptophan fluorescence), these calculated percentages of quenched

fluorescence of Trp+ and Trp− at each time point represent the lower bound of the actual amount of tryptophan partitioned near enough to the glycerol backbone to interact with the Br. The percentages reported are representative of the population of tryptophan molecules close to the Br atoms. Fluorescence that is not quenched or experiences a lesser degree of quenching is due to tryptophan being further from Br atoms; this is either because tryptophan is in the bulk solution or still buried in the bilayer but further away from the Br-PC lipids laterally or vertically. While the difference in the fluorescence energy of Trp+ and Trp− suggests that Trp+ is more strongly solvated in the low dielectric lipid environment, the greater quenching of Trp+ demonstrates that the positively charged molecule resides closer to the glycerol linkage than Trp−, and thus closer to the quenching Br atoms. However, at the time of elution, Trp− remained associated with the lipid bilayer and therefore capable of passing through the size exclusion column with the vesicle sample. The reduced blue-shifting of Trp− emission spectra and the lower percentage of quenching compared to Trp+ indicates that any Trp− associated with the lipid bilayer at the time of column elution was further away from the Br atoms and, thus, closer to the lipid headgroup/water interface. We will address this further in the discussion when we compare these observations to previously published computational results.

When evaluating the amount of fluorescence of Trp+ and Trp− over time in the presence of 30 mol% Br-PC (Table 5.1), we see almost 100% fluorescence recovery for Trp+ and Trp− over the 4 h of observation. This recovery of fluorescence can be attributed to tryptophan re-equilibrating with the surrounding bulk solution, and thus further away from the Br atoms within the bilayer. There is more Trp+ fluorescence recovery, again indicating that the Trp+ associated with the lipid bilayer at 10 min was closer to the Br residues than the Trp− at 10 min because the quenching capability of Br

is distance dependent. Since there was no tryptophan in the surrounding bulk solution at time 0, the tryptophan that was partitioned in the lipid bilayer exits the membrane for the bulk solution to re-equilibrate.

There was an evident loss in the intensity of λ_{max} over time for both Trp+ and Trp− in pure DOPC vesicles. There was a 32% decrease in the intensity of λ_{max} for low pH (i.e., Trp+, Figure 5.4a, solid lines) and 10% decrease for high pH (i.e., Trp−, Figure 5.4b, solid lines) when comparing the intensities of λ_{max} from 10 min to 4 h. Moreover, by 4 h after elution from the column, almost all of the Trp+ and Trp− was resolvated in the bulk buffered solution. Control experiments of tryptophan fluorescence in solution demonstrated that this loss in fluorescence intensity was not due to photobleaching; rather, the fluorescence quantum yield of tryptophan in aqueous environments was lower than in hydrophobic environments. This observation is indicative of more Trp+ associated with a more hydrophobic environment when the sample was initially eluted from the size exclusion column. In the case of Trp−, there was a significantly smaller change in the fluorescence intensity from 10 min to 4 h after elution. This is indicative of Trp− being in a more hydrophilic environment as soon as it is eluted from the size exclusion column and, thus, associated with the vesicle near the lipid headgroup/water interface. The observed loss in fluorescence intensity further demonstrates the migration of tryptophan from the interfacial region of the lipid bilayer to the bulk aqueous solution.

To summarize, the four observations from Figure 5.4 all show that more Trp+ interacts with the lipid bilayer than Trp− and provide a strong indication that the Trp+ associated with the lipid bilayer is in a hydrophobic environment, close to the glycerol backbone region. The Trp− associated with the lipid bilayer is in a more hydrophilic environment at the time of elution from the columns, indicating Trp− associates with the lipid bilayer closer to the headgroup interfacial region.

The spectra in Figure 5.4 are clearly asymmetric and broadened, and so we further decomposed these spectra into the sum of two Gaussians, I_{lip} and I_{wat} (eq 1) to investigate the red-shifting of the fluorescence maxima over the time course of the experiment and determine what factors contributed to the overall observed red shifts seen in Figure 5.4. Because both the λ_{max} and intensity of each fluorescence peak changes based on local environment, we normalized I_{lip} and I_{wat} to concentrate solely on spectral energy shifts and peak broadening. We set the normalization factor for I_{lip} to 1.5 and I_{wat} to 1, so that the changes in the spectra over time would be clear, and plot this in Figure 5.5. As described above, I_{lip} (i.e., shorter λ_{max}) are representative of tryptophan near the glycerol backbone region of the lipid bilayer, and I_{wat} (i.e., longer λ_{max}) are representative of tryptophan in a hydrophilic environment (bulk water). All spectra are shown for 10 min (blue), 1 h (green), and 4 h (red) after elution from the size exclusion column. As seen in Figure 5.5a,b, I_{lip} experienced a 9 nm red shift for Trp+ over the time course of the experiment, compared to only a 2 nm red shift for Trp− over the same time. This indicates that Trp+ is in a more hydrophobic environment when the sample is eluted from the column, and the majority of the Trp+ leaves the hydrophobic lipid environment to enter the aqueous bulk solution. On the other hand, the smaller observed red shift for Trp− demonstrates that the negatively charged molecule is in a more hydrophilic environment at the time of column elution, and so changes to the chemical environment over the time course of the experiment are small. There was a slight broadening of the I_{wat} spectra for both Trp+ and Trp− that we attributed qualitatively to the greater diversity of environments that hydrated tryptophan experiences after it leaves the polar and zwitterionic headgroup region of the lipid and enters the aqueous bulk solution.

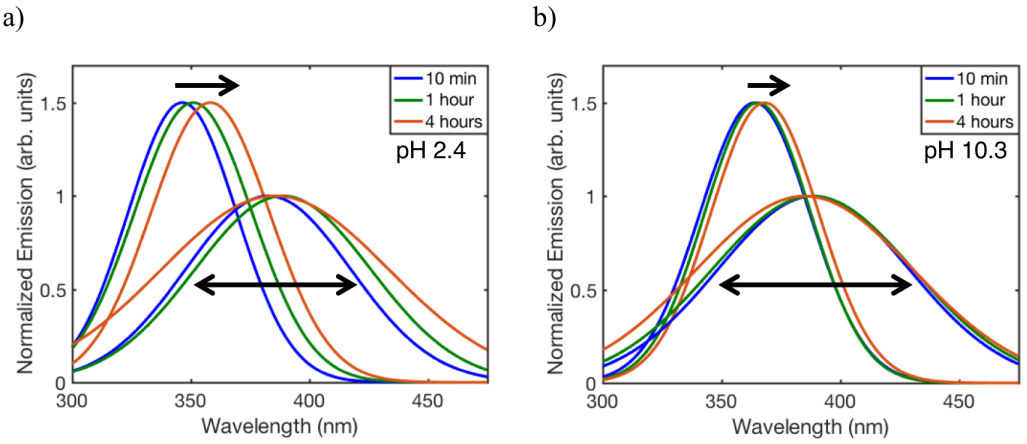

Figure 5.5: Normalized Gaussians I_{lip} (shorter wavelengths) and I_{wat} (longer wavelengths) from selected time points for DOPC vesicles with partitioned charged tryptophan. I_{lip} spectra are normalized to 1.5 maxima and I_{wat} spectra are normalized to maxima of 1 for ease of viewing. All spectra are shown for 10 min (blue), 1 hr (green), and 4 hr (red) after tryptophan-containing vesicles were equilibrated in buffer without tryptophan. Arrows indicate the changes of the spectra over time. **a**: pH 2.4 (Trp+); **b**: pH 10.3 (Trp-).

Because of our sequence of experimental steps, any tryptophan measured in Figures 5.4 and 5.5 must come from molecules that are associated, in some way, with the lipid bilayer vesicles as they are passed through the size exclusion column and into a buffer devoid of any tryptophan. The goal of this report is to determine the extent of tryptophan binding within some portion of the membrane interior, but tryptophan that had completely penetrated both leaflets of the bilayer structure and entered the interior of the vesicle would also travel through the size exclusion column with the vesicle and would be convoluted with fluorescence spectra that we have discussed so far, complicating our analysis. To eliminate this concern, we created tryptophan-containing vesicles by hydrating lipid films in the presence of the tryptophan stock solution, which created vesicles in which the concentration of tryptophan both inside and outside the vesicle was the same. We then performed the same series of experiments described above. We

observed a significantly higher amount of tryptophan present in the solution, a lower degree of quenching, and more tryptophan in a hydrophilic environment after the vesicle was separated from the initial solution by size exclusion chromatography. These observations indicate that more tryptophan was present because it was trapped inside of the vesicles during the column elution. These molecules could not permeate through the hydrophobic core of the lipid membrane, and remained in the interior of the vesicles over the time course of the experiment. The same behavior was observed for Trp+ and Trp− with these experiments.

5.6 MD SIMULATIONS

Previous calculations performed by our collaborator, Dr. Alfredo Cardenas, in which Trp+ and Trp− were simulated at various depths within the DOPC bilayer have demonstrated that there is a significant difference in free energy change, based on charge, when tryptophan enters the DOPC membrane.[21] This is shown in Figure 5.6, where the x-axis represents the distance from the center of the bilayer, and where a DOPC molecule and solvating water molecules are drawn to scale to show their location along the membrane normal. While the PMF for Trp− is only slightly lower than that of solution (~2 kcal mol^{-1}), there is a significant drop in the PMF for Trp+ (~9 kcal mol^{-1}). There is also a significant difference in the location of the minimum PMF between the two molecules. Trp− achieves a minimum free energy very near the membrane−water interface, where it appears to be stabilized by the positively charged choline functional group. However, the minimum free energy position for Trp+ is significantly further into the membrane interior, much closer to the ester linkage that connects the high and low dielectric components of the lipid. At this position, Trp+ is stabilized not just by the negatively charged phosphate group on the lipid but also the electronegative oxygen

atoms of the ester, which can also accept hydrogen bonds from the tryptophan backbone. This difference in equilibrium position of just 6 Å is a remarkable consequence of the molecular structure of the phospholipid forming the two-dimensional bilayer. No matter what charge the tryptophan carries, the PMF rises dramatically as soon as the molecule moves further into the interior of the lipid bilayer, increasing to ~12−22 kcal mol^{-1} higher at the membrane center than in aqueous solution. This indicates that any tryptophan that does reside within the membrane is significantly more likely to exit the vesicle by moving back to the exterior of the vesicle, not through the membrane center and into the other leaflet.

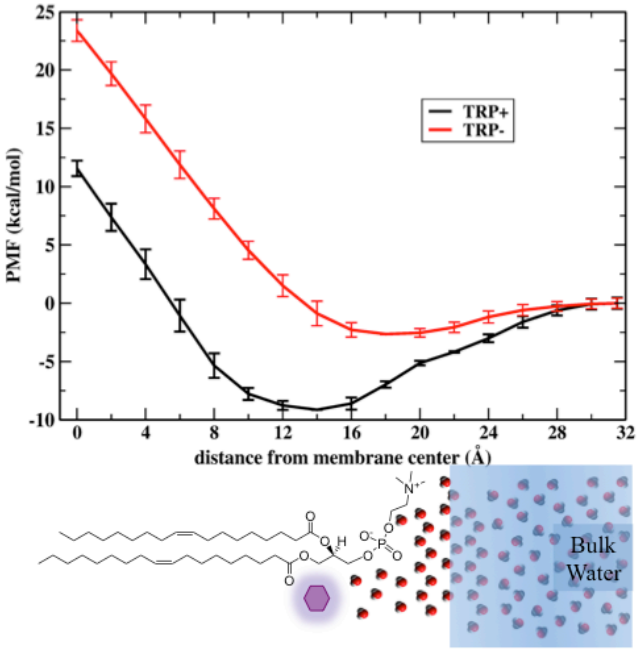

Figure 5.6: Computed free energy profile of Trp+ (black) and Trp- (red) as a function of distance from membrane center. Below the x-axis is a DOPC molecule and magenta hexagon representing the approximate location of Trp+ locations of the lipid structure along the dimensions of the x-axis.

5.7 DISCUSSION

The purpose of this work was to determine the extent to which a charged tryptophan molecule permeates across the lipid bilayer at equilibrium *versus* partitions into the structure of the lipid bilayer at equilibrium. Further, if charged tryptophan does partition into the membrane, our goal was to determine approximately where it resides at equilibrium, which might account for the consistent observation that tryptophan side chains are found at the near-surface region of the membrane in transmembrane proteins. Finally, our goal was to determine any quantitative differences between positively and negatively charged molecules, which might account for the observation that CPPs predominantly carry a positive charge.

Predictions and observations from simulations and experiments discussed in this chapter support one another. The initial fluorescence wavelength of charged tryptophan was significantly lower for Trp+ than Trp− (Figure 5.4), demonstrating that soon after vesicles had been removed from the spiked solution and were equilibrating in the tryptophan-free buffer, Trp+ was deeper into the low dielectric, hydrophobic interior of the membrane than Trp−. These results are confirmed by the greater degree of quenching of Trp+ fluorescence than that of Trp−, resulting from the position of Trp+ closer to the ester linkage (and therefore the quenching Br atoms) than Trp−. Because Trp− fluorescence was actually measured after the vesicles were passed through the size exclusion column, some Trp− was, in fact, closely associated with the vesicle. However, because the fluorescence energy of Trp− was near its value in pH 10.3 buffer, Trp− that moved through the size exclusion column with the vesicle appeared to be weakly associated with the surface region of the membrane near the positively charged choline. This Trp− then quickly dissociated from the vesicle surface, moving even further away from the vesicle, seen in the small decrease in fluorescence quenching in Figure 5.4b.

Furthermore, our experiments find that Trp+ reaches a higher equilibrium concentration than Trp− when partitioning in the lipid bilayer. This is predicted by the more attractive PMF calculated for Trp+ than Trp−, shown in Figure 5.6. Experimentally, this was estimated by determining the amount of tryptophan present in the sample at the time of elution. We determined the amount of Trp+ and Trp− present in the samples after the column elution by comparing the intensity of the 4 h time point spectra (in Figure 5.4) to the calibration curve for each buffer solution. We found 0.38 ± 0.04 mM Trp+ compared to only 0.076 ± 0.007 mM Trp− in solution after 4 h column elution. In other words, at equilibrium, 5 times as much Trp+ partitioned within the lipid bilayer membrane as Trp−. This result qualitatively agrees with the PMF calculations in Figure 5.6.

Previous work in our group experimentally explored Trp+, Trp−, and zwitterionic tryptophan (dissolved in solutions of pH 5.5 and 7.2). We also calculated the PMF of Trp+, Trp−, uncharged tryptophan, and a zwitterionic tryptophan molecule permeating through a DOPC lipid bilayer. We found that the equilibrium concentration and calculated PMF of neutral tryptophan fell between those results for Trp+ and Trp−. Because our long-term interests are focused on the effect of molecular charge on membrane−molecule interactions, we did not investigate zwitterionic tryptophan in the current work. However, on the basis of our earlier work, we hypothesize that this molecule would partition itself in the lipid bilayer in an orientation that would allow the positively charged N-terminus to interact with the glycerol backbone region and the negatively charged C-terminus to interact with the choline group. In this scenario, we expect an equilibrium amount of zwitterionic tryptophan intermediate between Trp+ and Trp−.

The results presented here offer insight into the mechanism by which positively charged CPPs can penetrate a lipid bilayer membrane composed at least in part of zwitterionic phosphatidylcholine. In order to penetrate the lipid bilayer, there must be some initial interaction between the peptide and the bilayer. Although the lipid headgroup is zwitterionic, and can interact in essentially the same way with a molecule carrying either charge, the electronegative ester linkage directly under the headgroup will always favor a positively charged molecule. Moreover, the positively charged choline is more exposed to solvent compared to the phosphate. The phosphate, therefore, motivates the positively charged peptide to permeate more deeply into the membrane. If molecules of either charge can interact in some favorable way with the zwitterionic headgroup, shown in Figure 5.6, then dynamic fluctuations that expose the glycerol backbone to the headgroup region will favorably interact with positively charged molecules and, thus, select the positive charge for interactions deeper within the membrane. On the other hand, negatively charged molecules will be repelled from the negatively charged glycerol backbone region and remain closer to the water interface, where they can interact with the positively charged choline group on the lipid head. While Trp+ is not a large enough molecule to test further mechanisms of how CPPs, which are typically 15−30 amino acids in length, can further travel across the membrane, tryptophan is an ideal test for the role of charge near the lipid headgroup.

5.8 CONCLUSION

In conclusion, we have demonstrated that the charge on a single tryptophan molecule, controlled by solution pH protonation of the terminal groups, controls the propensity of the molecule to partition into a DOPC lipid bilayer membrane. In the presence of Br-PC lipids, we found that more Trp+ fluorescence was quenched compared

to Trp−, meaning Trp+ partitions closer to the glycerol backbone region, while Trp− partitions further away from the glycerol backbone region (closer to the water interface). When the tryptophan-containing phosphocholine lipid vesicles were re-equilibrated with a solution containing no tryptophan, both Trp+ and Trp− returned to the bulk solution and did not permeate through the lipid bilayer.

On the basis of these results, we conclude that independent of its charge, tryptophan partitions in the lipid bilayer and does not permeate through the hydrophobic core of the bilayer at room temperature on the time scale of the experiment. We further conclude that the charge of tryptophan greatly affects the equilibrium reached when it partitions in the lipid bilayer; Trp+ has more favorable interactions with the interfacial region of the lipid bilayer than Trp− and therefore results in a greater amount of Trp+ partitioning in the lipid bilayer compared to Trp−. These results can offer insight into the mechanism by which CPPs are introduced and begin to penetrate lipid bilayers. These findings are consistent with the literature on tryptophan acting as an anchor for trans-membrane proteins, and CPPs being composed of mostly positively charged amino acid residues.

5.9 REFERENCES

1. Deamer, D.; Kuzina S.I.; Mikhailov, A. I.; Maslikova, E. I.; Seleznev, S. A. Origin of Amphiphilic Molecules and Their Role in Primary Structure Formation. *J. Evol. Biochem. Physiol.* **1991,** *27*, 212-217.

2. Deamer, D. W., Role of Amphiphilic Compounds in the Evolution of Membrane Structure on the Early Earth. *Orig. Life Evol. Biosph.* **1986,** *17*, 3-25.

3. Morowitz, H. J.; Heinz, B.; Deamer, D. W. The Chemical Logic of a Minimum Protocell. *Orig. Life Evol. Biosph.* **1988,** *18*, 281-287.

4. Pohorille, A.; Deamer, D. Self-Assembly and Function of Primitive Cell Membranes. *Res. Microbiol.* **2009,** *160*, 449-456.

5. Yang, N. J.; Hinner, M. J. Getting Across the Cell Membrane: An Overview for Small Molecules, Peptides, and Proteins. *Methods Microbiol.* **2015,** *1266*, 29-53.

6. Lipinski, C. A.; Lombardo, F.; Dominy, B. W.; Feeney, P. J., Experimental and Computational Approaches to Estimate Solubility and Permeability in Drug Discovery and Development Settings. *Adv. Drug Delivery Rev.* **1997,** *23*, 3-25.

7. Veber, D. F.; Johnson, S. R.; Cheng, H.-Y.; Smith, B. R.; Ward, K. W.; Kopple, K. D. Molecular Properties That Influence the Oral Bioavailability of Drug Candidates. *J. Med. Chem.* **2002,** *45*, 2615-2623.

8. Guimarães, C. R. W.; Mathiowetz, A. M.; Shalaeva, M.; Goetz, G.; Liras, S. Use of 3D Properties to Characterize Beyond Rule-of-5 Property Space for Passive Permeation. *J. Chem. Inf. Model.* **2012,** *52*, 882-890.

9. Al-Awqati, Q. One Hundred Years of Membrane Permeability: Does Overton Still Rule? *Nat. Cell Biol.* **1999,** *1*, 201-202.

10. Li, L.; Vorobyov, I.; Allen, T. W. The Different Interactions of Lysine and Arginine Side Chains with Lipid Membranes. *J. Phys. Chem. B* **2013,** *117*, 11906-11920.

11. Bemporad, D.; Luttmann, C.; Essex, J. W. Computer Simulation of Small Molecule Permeation across a Lipid Bilayer: Dependence on Bilayer Properties and Solute Volume, Size, and Cross-Sectional Area. *Biophys. J.* **2004,** *87*, 1-13.

12. Chakrabarti, A. C.; Deamer, D. W. Permeability of Lipid Bilayers to Amino Acids and Phosphate. *Biochim. Biophys. Acta, Biomembr.* **1992,** *1111*, 171-177.

13. Wimley, W. C.; White, S. H. Experimentally Determined Hydrophobicity Scale for Proteins at Membrane Interfaces. *Nat. Struct. Biol.* **1996,** *3*, 842.

14. MacCallum, J. L.; Bennett, W. F. D.; Tieleman, D. P. Partitioning of Amino Acid Side Chains into Lipid Bilayers: Results from Computer Simulations and Comparison to Experiment. *J. Gen. Physiol.* **2007,** *129*, 371.

15. Chakrabarti, A. C. Permeability of Membranes to Amino Acids and Modified Amino Acids: Mechanisms Involved in Translocation. *Amino Acids* **1994,** *6*, 213-229.

16. Yesylevskyy, S.; Marrink, S.-J.; Mark, A. E. Alternative Mechanisms for the Interaction of the Cell-Penetrating Peptides Penetratin and the TAT Peptide with Lipid Bilayers. *Biophys. J.* **2009,** *97*, 40-49.

17. Vivès, E.; Schmidt, J.; Pèlegrin, A. Cell-Penetrating and Cell-Targeting Peptides in Drug Delivery. *Biochim. Biophys. Acta, Rev. Cancer* **2008,** *1786*, 126-138.

18. Huang, K.; García, Angel E. Free Energy of Translocating an Arginine-Rich Cell-Penetrating Peptide across a Lipid Bilayer Suggests Pore Formation. *Biophys. J.* **2013,** *104*, 412-420.

19. Herce, H. D.; Garcia, A. E.; Litt, J.; Kane, R. S.; Martin, P.; Enrique, N.; Rebolledo, A.; Milesi, V. Arginine-Rich Peptides Destabilize the Plasma Membrane, Consistent with a Pore Formation Translocation Mechanism of Cell-Penetrating Peptides. *Biophys. J.* **2009,** *97*, 1917-1925.

20. Herce, H. D.; Garcia, A. E. Cell Penetrating Peptides: How Do They Do It? *J. Biol. Phys.* **2007,** *33*, 345-356.

21. Cardenas, A. E.; Shrestha, R.; Webb, L. J.; Elber, R., Membrane Permeation of a Peptide: It is Better to be Positive. *J. Phys. Chem. B* **2015,** *119*, 6412-20.

22. White, S. H.; Wimley, W. C. Membrane Protein Folding and Stability: Physical Principles. *Annu. Rev. Biophys. Biomol. Struct.* **1999,** *28*, 319-365.

23. Killian, J. A.; von Heijne, G. How Proteins Adapt to a Membrane–Water Interface. *Trends Biochem. Sci.* **2000,** *25*, 429-434.

24. Yau, W.-M.; Wimley, W. C.; Gawrisch, K.; White, S. H. The Preference of Tryptophan for Membrane Interfaces. *Biochemistry* **1998,** *37*, 14713-14718.

25. Sanchez, Katheryn M.; Kang, G.; Wu, B.; Kim, Judy E. Tryptophan-Lipid Interactions in Membrane Protein Folding Probed by Ultraviolet Resonance Raman and Fluorescence Spectroscopy. *Biophys. J.* **2011,** *100*, 2121-2130.

26. Granseth, E.; von Heijne, G.; Elofsson, A. A study of the Membrane-Water Interface Region of Membrane Proteins. *J. Mol. Biol.* **2005,** *346*, 377-85.

27. Landolt-Marticorena, C.; Williams, K. A.; Deber, C. M.; Reithmeier, R. A. F. Non-random Distribution of Amino Acids in the Transmembrane Segments of Human Type I Single Span Membrane Proteins. *J. Mol. Biol.* **1993,** *229*, 602-608.

28. Chamberlain, A. K.; Lee, Y.; Kim, S.; Bowie, J. U. Snorkeling Preferences Foster an Amino Acid Composition Bias in Transmembrane Helices. *J. Mol. Biol.* **2004,** *339*, 471-479.

29. Arkin, I. T.; Brunger, A. T. Statistical Analysis of Predicted Transmembrane α-Helices. *Biochim. Biophys. Acta, Protein Struct. Mol. Enzymol.* **1998,** *1429*, 113-128.

30. Jobin, M.-L.; Blanchet, M.; Henry, S.; Chaignepain, S.; Manigand, C.; Castano, S.; Lecomte, S.; Burlina, F.; Sagan, S.; Alves, I. D. The Role of Tryptophans on the Cellular Uptake and Membrane Interaction of Arginine-Rich Cell Penetrating Peptides. *Biochim. Biophys. Acta, Biomembr.* **2015,** *1848*, 593-602.

31. de Jesus, A. J.; Allen, T. W. The Role of Tryptophan Side Chains in Membrane Protein Anchoring and Hydrophobic Mismatch. *Biochim. Biophys. Acta, Biomembr.* **2013,** *1828*, 864-876.

32. Ulmschneider, J. P.; Andersson, M.; Ulmschneider, M. B. Determining Peptide Partitioning Properties via Computer Simulation. *J. Membr. Biol.* **2011,** *239*, 15-26.

33. Ulmschneider, M. B.; Sansom, M. S. P. Amino Acid Distributions in Integral Membrane Protein Structures. *Biochim. Biophys. Acta, Biomembr.* **2001,** *1512*, 1-14.

34. Arseniev A. S.; Barsukov, I. L.; Bystrov, V. F.; Lomize, A. L.; Ovchinnikov Y. A. 1H-NMR Study of Gramicidin A Transmembrane Ion Channel. Head-to-head Right-handed, Single-stranded Helices. *FEBS Lett.* **1985,** *186*, 168-184.

35. Cowan, S. W.; Schirmer, T.; Rummel, G.; Steiert, M.; Ghosh, R.; Pauptit, R. A.; Jansonius, J. N.; Rosenbusch, J. P. Crystal Structures Explain Functional Properties of Two E. Coli Porins. *Nature* **1992,** *358*, 727.

36. Deisenhofer, J.; Michel, H. The Photosynthetic Reaction Centre From the Purple Bacterium Rhodopseudomonas viridis. *EMBO J.* **1989,** *8*, 2149-2170.

37. *Probing Membrane Protein Structure and Dynamics by Fluorescence Spectroscopy. Encyclopedia of Analytical Chemistry [Online];* Wiley & Sons, https://onlinelibrary.wiley.com/doi/abs/10.1002/9780470027318.a9353 (accessed Aug 1, 2018).

38. Lakowicz, J. R. *Principles of Fluorescence Spectroscopy*; Springer: New York, 2006; pp 205-235.

39. Vivian, J. T.; Callis, P. R. Mechanisms of Tryptophan Fluorescence Shifts in Proteins. *Biophys. J.* **2001,** *80*, 2093-2109.

40. Valeur, B.; Weber, G. Resolution of the Fluorescence Excitation Spectrum of Indole into the 1La and 1Lb Excitation Bands. *Photochem. Photobiol.* **1977,** *25*, 441-444.

41. Soni, Smita P.; Adu-Gyamfi, E.; Yong, Sylvia S.; Jee, Clara S.; Stahelin, Robert V. The Ebola Virus Matrix Protein Deeply Penetrates the Plasma Membrane: An Important Step in Viral Egress. *Biophys. J.* **2013,** *104*, 1940-1949.

42. Pfefferkorn, C. M.; Walker, R. L.; He, Y.; Gruschus, J. M.; Lee, J. C. Tryptophan Probes Reveal Residue-Specific Phospholipid Interactions of Apolipoprotein C-III. *Biochim. Biophys. Acta* **2015,** *1848*, 2821-2828.

43. Gable, J. E.; Schlamadinger, D. E.; Cogen, A. L.; Gallo, R. L.; Kim, J. E. Fluorescence and UV Resonance Raman Study of Peptide-Vesicle Interactions of Human Cathelicidin LL-37 and its F6W and F17W Mutants. *Biochemistry* **2009,** *48*, 11264-11272.

44. Lakowicz, J. R. *Principles of Fluorescence Spectroscopy*; Springer: New York, 2006; pp 331-351.

45. Liu, L.-P.; Deber, C. M. Anionic Phospholipids Modulate Peptide Insertion into Membranes. *Biochemistry* **1997,** *36*, 5476-5482.

46. Mishra, V. K.; Palgunachari, M. N. Interaction of Model Class A1, Class A2, and Class Y Amphipathic Helical Peptides with Membranes. *Biochemistry* **1996,** *35*, 11210-11220.

47. Macd̂o, Z. S.; Furquim, T. A.; Ito, A. S. Estimation of Average Depth of Penetration of Melanotropins in Dimyristoylphosphatidylglycerol Vesicles. *Biophys. Chem.* **1996,** *59*, 193-202.

48. Lewis, R. N. A. H.; McElhaney, R. N. Fourier Transform Infrared Spectroscopy in the Study of Lipid Phase Transitions in Model and Biological Membranes: Practical Considerations. In *Methods in Membrane Lipids*, Dopico, A. M., Ed. Humana Press: NJ, 2007; pp 207-227.

Chapter 6: Partitioning of Positively and Negatively Charged Tryptophan Ions in Membranes with Inverted Phospholipid Heads

6.1 Publication Note

Portions of the methods outlined in this section were adapted from the following publication:

1. Cardenas, A. E.; **Anderson, C. M.**; Elber, R.; Webb, L. J. Partition of Positively and Negatively Charged Tryptophan Ions in Membranes with Inverted Phospholipid Heads: Simulations and Experiments. *J. Phys. Chem. B* **2019,** *123,* 3272-3281. [C. M. Anderson performed all experimental measurements, including vesicle formation and infrared and fluorescence spectroscopic measurements. A. E. Cardenas performed all of the molecular dynamics calculations.]

6.2 Introduction

As discussed in Chapter 5, one of the main functions of a cell membrane is to hamper or block the transport of compounds or organelles in and out of the cell. Since transport of selected materials is needed for cell survival, specific protein transporters or channels facilitate the translocation of key substances. Still, some molecules can permeate the membrane via a non-facilitated diffusive mechanism. The cell must counter such a passive permeation and in some cases pumps are introduced to retain concentration gradients.[1] For charged species passive permeation is more difficult compared to uncharged species of otherwise similar properties due to the hydrophobic nature of the lipids. Despite the low-dielectric barrier posed by the membrane, permeation of charged species including lipophilic ions or cell penetrating peptides (CPPs), has been observed experimentally.[2-4]

Simulations have suggested that significant membrane distortions must occur during the permeation of charged molecules.[5-8] These membrane defects enable partial solvation of the permeant during the transport process. A small number of water molecules enter the hydrophobic region forming transient water wires and assisting the translocation of the charged permeant. Moreover, lipid molecules in the membrane bend to facilitate interaction of the head group and glycerol linker with the penetrating charge. These perturbations lower the free energy barrier for permeation compared to the magnitude of that estimated for unperturbed membranes. However, there is a free energy cost to create these defects that opposes permeation of charged molecules.

In previous work in our laboratory,[9] which was discussed in Chapter 5, we used a combination of atomically detailed simulations and experiments to study the insertion of a charged tryptophan through a phosphatidylcholine lipid bilayer, composed of 1,2-dioleoyl-sn-glycero-3-phosphocholine (DOPC). We used low (2.4), neutral (7.2), and high (10.3) pH conditions to control the charge of the tryptophan as positive, zwitterionic, or negative, respectively. Computationally, we simulated the potential of mean force and permeability coefficient with the inhomogeneous solubility-diffusion model.[10-11] The main conclusion of both the experiments and the simulations that we drew at that time was that the positively charged tryptophan permeates faster than the negatively charged and zwitterionic species. We experimentally addressed the difference between permeation across the lipid bilayer and partitioning of both positively and negatively charged tryptophan in DOPC vesicles in the work described in Chapter 5.[12] By adding a fraction of brominated lipids into the vesicles we were able to assess the location of the charged tryptophan species across the bilayer by measuring the tryptophan fluorescence quenching caused by the brominated lipids. Further, we were able to assign tryptophan's emission maxima (λ_{max}) to the local environment of the tryptophan molecules. For

example, a blue shift in the λ_{max} is indicative of a hydrophobic environment and a red shift is indicative of tryptophan being in a more hydrophilic environment. Our results indicated that the positively charged tryptophan (Trp+) is partitioned into the lipid bilayer closer to the glycerol backbone region rather than completely crossing the membrane. On the other hand, negatively charged tryptophan (Trp-) stay mostly at the outer water-membrane interface.

These results were consistent with previous observations about the behavior of cell penetrating peptides that are almost always positively charged.[2-3] It was inconsistent, however, with a theory that ignores local membrane defects and interactions and predicts favorable permeation of negative charges.[13]

To determine how the head group charge orientation affects the partitioning of Trp+ and Trp- we considered the interaction of the same charged species through two different membranes: DOPC and 2-((2,3-bis(oleoyloxy)propyl)dimethylammonio)ethyl ethyl phosphate (DOCPe), where DOCPe has an inverted head group compared to DOPC (Figure 6.1). In DOPC, the phosphate and glycerol groups are negatively charged or polarized, and therefore support the penetration and partitioning of positively charged molecules into the membrane. The glycerol groups are embedded deeper in the membrane compared to the rest of phospholipid head and therefore assist the insertion of cations closer to the hydrophobic core. The positively charged choline groups do not impair the insertion of cations significantly, because they are well screened by the high dielectric solvent (water) and do not penetrate significantly into the membrane. In contrast, the negatively charged molecules, which are attracted to the choline heads at the surface of the DOPC membrane, are repelled by the negatively charged groups when the anions move toward the membrane center. They are, therefore, less likely to be inserted deeply into the membrane.[12]

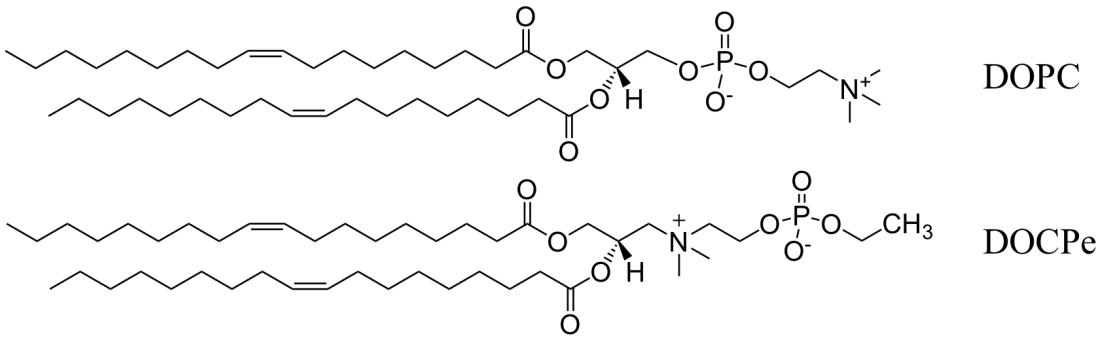

Figure 6.1: A drawing of the two phospholipid molecules that are considered in the present manuscript. DOPC (top) is a phospholipid that is frequently found in biological systems, (2) DOCPe, is a synthetic molecule, not found in biological systems, in which the positions of the choline and the phosphate groups are switched.

DOCPe, the inverted phospholipid we considered for this study, is different because the negative charge of the phosphate groups is well solvated and the contribution of the positively charged choline groups is balanced by the deeper carbonyl groups. Since the carbonyls of the glycerol group remain untouched, the impact of the head switch was not obvious.

Several related studies have been conducted on charged amino acid insertion through different phospholipid membranes.[14-16] Recently, several inverted phosphocholine molecules were synthesized including DOCPe (Figure 6.1),[17] the inverted head group counterpart of DOPC that we used in our previous studies. Liposomic membranes were formed and experiments showed that encapsulated anionic carboxyfluorescein is released 20 times faster from the inverted phosphocholine vesicles than the standard phosphocholine vesicles.[17] However, Perttu et al. did not examine cationic insertion or the permeation of cationic and anionic species with similar shapes. In this work different ions were examined to explore charge selectivity by membrane variations.

Two molecular dynamics simulations studies were performed with inverse head group lipids. The first one compared DLPC and DLCPe lipids[18] and a more recent study considered DPPC and DPCPe membranes.[19] Both studies considered the effects of the head group inversion on the surface binding of sodium, potassium and calcium ions in aqueous solutions. Besides differences in tail size (DOCPe has 18 carbon atoms, *versus* 12 and 16 for DLCPe and DPCPe lipids, respectively), and saturation (both DLCPe and DPCPe are saturated while DOCPe is monounsaturated) in these studies we considered more complex ions that have a side chain with some amphipathic character. The study of a tryptophan is also more relevant to the biological function of charged cell penetrating peptides.

The qualitative partitioning mechanism, summarized above, in which the relative positions and charges of the constituent groups in the phospholipid head determine the efficiency of charge insertion, was discussed in the previous chapter.[12] The model was consistent with the reported experiments and simulations. To further test the model and expand its applicability to the design of new molecules, we examined the phospholipid molecule, DOCPe, which could impact the proposed mechanism.

6.3 METHODS

Vesicles made of DOPC or DOCPe were prepared using the extrusion method, described in Section 2.3.2. The vesicle samples were hydrated with either a citric acid buffer at pH 2.4 or sodium carbonate and sodium bicarbonate buffer at pH 10.3. 10 mM tryptophan solutions were also made in the corresponding buffers, which allowed us to control the charge of tryptophan in solution.

The prepared 30 mM lipid vesicle solutions and 10 mM tryptophan stock solutions (with the same buffer) were mixed in a 1:3 v/v ratio. 400 μL aliquots of the

mixture were taken at various time points from 0 h to 24 h. Each aliquot was immediately passed through a PD-10 column as described in the previous chapter in Section 5.3. The resulting elution was then used for a fluorescence measurement using the plate reader. Fluorescence data collected using this method allowed us to determine the rate at which tryptophan associated with the lipid bilayer.

To determine the depth at which tryptophan penetrated the bilayer, we again mixed the prepared vesicle solutions and tryptophan stock solutions in a 1:3 v/v ratio. The mixture was then allowed to equilibrate for 4-6 hours, which we knew to be well over the equilibration time (from the previously described association rate experiments). A 400 μL aliquot was then taken and passed through a PD-10 column as previously described. A fluorescence spectrum was immediately taken of the elution. Subsequent fluorescence emission spectra were collected every 10-20 min for 4 h; at which point the tryptophan that was associated with the lipid bilayer has re-equilibrated with the surround bulk solution (which was free of tryptophan immediately after the column elution). These fluorescence emission spectra were collected using the Fluorolog-3 fluorimeter, as described in the previous chapter in Section 5.3.

6.4 FLUORESCENCE SPECTROSCOPY

In Figure 6.2 we show the concentration of tryptophan (μM) associated with vesicles composed of DOPC (empty circles) or DOCPe (filled circles) lipid bilayers at various time points from 0-60 minutes. The concentration of tryptophan introduced to the bulk solution was 7.5 mM. It is important to note that the concentrations reported are for the solutions after being passed through the column at various time points. Once the solution is passed through the column the tryptophan outside of the vesicles is removed and we only measure fluorescence for the tryptophan remaining partitioned in the

vesicles. The charge of tryptophan, positive or negative, is controlled by the pH of the buffer solution: positive at a pH of 2.4 (pKa 2.38) and negative at a pH of 10.3 (pKa 9.39). Two conclusions are clear from these data: 1) the partitioning of Trp+ within the DOPC vesicles is about 2.5 times larger than that of the DOCPe lipid vesicles; and 2) the partitioning of the Trp- within both bilayers is about 3.5 times smaller than that of the positively charged species in DOPC bilayers. Both of these results are in qualitative agreement with the simulations discussed in section 6.4. Moreover, the difference of the partitioning in the two membranes for Trp- is much smaller than that for Trp+, again in accord with the simulations.

To determine whether we were observing tryptophan permeating through the lipid vesicles or partitioning into the lipid bilayer, we looked at the change in fluorescence emission energy to determine tryptophan's local environment. We established this as a method to compare the interactions of Trp+ and Trp- with DOPC lipid vesicles in Chapter 5. Because tryptophan's λ_{max} is sensitive to its local environment, we can determine if tryptophan is in a hydrophobic (lipid tail like) or hydrophilic (head group like) environment. Recall, when tryptophan is in a hydrophobic environment such as hexanes, its λ_{max} is ~340 nm; when in an aqueous solution its λ_{max} is ~375 nm.

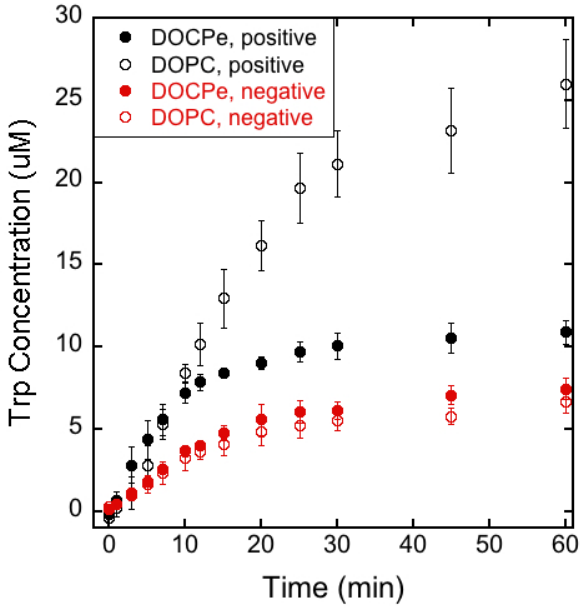

Figure 6.2: Concentration of charged tryptophan associated with DOCPe (filled circles) and DOPC (empty circles) vesicles as a function of time at low pH (positively charged tryptophan, black symbols) and high pH (negatively charged tryptophan, red symbols).

In Figure 6.3 we present the change of the fluorescence emission spectra of both positively and negatively charged tryptophan with DOCPe and DOPC lipid vesicles. At pH 2.4 with Trp+ (Figure 6.3a), we compared the shift of λ_{max} for Trp+ in DOCPe lipid vesicles (solid lines) and Trp+ in DOPC lipid vesicles (dashed lines). There was a 7 nm shift for Trp+ in the DOCPe lipid vesicles from 10 min (λ_{max} = 354 nm) to 4 hours (λ_{max} = 361 nm) after column elution. In contrast, we observed a 12 nm shift for Trp+ in DOPC lipid vesicles from 10 min (λ_{max} = 346 nm) to 4 hours (λ_{max} = 358 nm). At pH 10.3 with Trp- (Figure 6.3b), we again determined the change in λ_{max} for Trp- in DOCPe lipid vesicles (solid lines) and Trp- in DOPC lipid vesicles (dashed lines). In the case of Trp- and DOCPe lipid vesicles, we observed a 3 nm shift from 10 min (λ_{max} = 366 nm) to 4 hours (λ_{max} = 369 nm) after column elution. Similarly, for Trp- and DOPC lipid vesicles,

we observed a 2 nm shift from 10 min (λ_{max} = 368 nm) to 4 hours (λ_{max} = 370 nm) after elution.

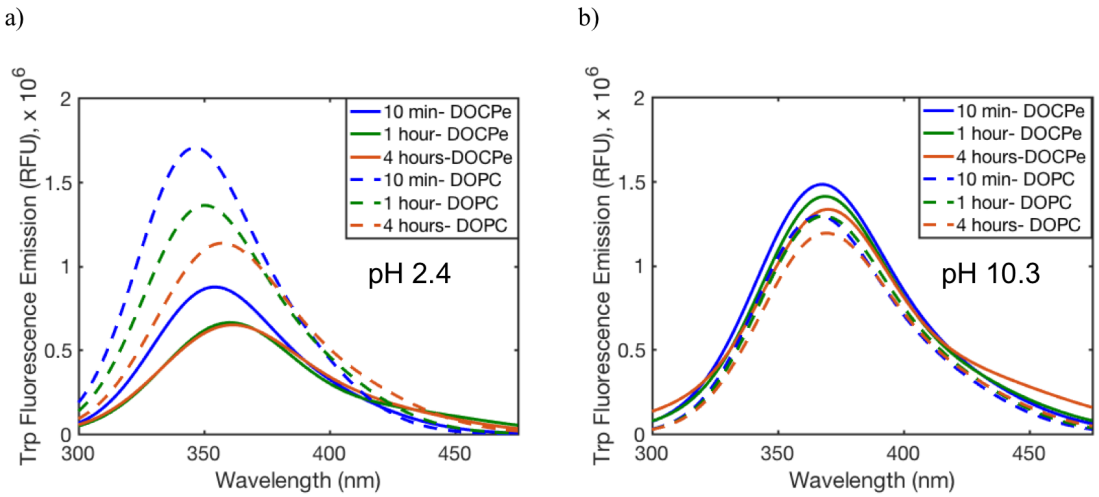

Figure 6.3: Representative spectra from selected time points for tryptophan and DOCPe vesicles (solid lines) and DOPC vesicles (dashed lines). Spectra are shown at 10 min (blue), 1 hr (green), and 4 hr (red) after tryptophan-containing vesicles were re-equilibrated in a buffer without tryptophan. **a**: Spectra collected at pH 2.4 (Trp+); **b**: Spectra collected at pH 10.3 (Trp-).

In the case of Trp+ and DOCPe lipid vesicles, there are two important observations: 1) tryptophan's λ_{max} at 10 minutes after column elution is red shifted compared to that of Trp- and DOPC lipid vesicles; and 2) there is overall a smaller energy shift in λ_{max} from 10 min to 4 hours after column elution for Trp+ in DOCPe lipid vesicles (7 nm) compared to Trp+ in DOPC lipid vesicles (12 nm). From these two observations we can determine that Trp+ is in a more hydrophilic environment when it partitions in the DOCPe lipid bilayer compared to when it partitions in the DOPC lipid bilayer. We associate the red shifted λ_{max} of Trp+ with the DOCPe lipid bilayer at 10 min after elution with Trp+ partitioning closer to the water interface in DOCPe lipid bilayer

compared to the DOPC lipid bilayer. The observed λ_{max} shifts of Trp+ provide further evidence that Trp+ is partitioned in a less hydrophobic environment within the DOCPe bilayer compared to the DOPC bilayer. We are detecting a shift in the λ_{max} because tryptophan is re-equilibrating with the surrounding bulk solution that is absent of any tryptophan after elution. When re-equilibration is reached almost all of the tryptophan present is in bulk water because the ratio of bulk water to lipid vesicle volume is large. Therefore, the greater the shift we detect, the more indicative it is of tryptophan being partitioned in a more hydrophobic environment in the beginning. In the previous chapter we discussed that Trp+ partitioned at or near the glycerol backbone region in the DOPC lipid bilayer; in the case of Trp+ in the DOCPe lipid bilayer, due to the flipped head group charge arrangement, it is more difficult for Trp+ to reach the glycerol backbone region and it instead partitions closer to the head group region. The different location of the partition sites for Trp+ in the two membranes agrees with the simulations (see Section 6.5 MD Simulations).

In the case of Trp- and DOCPe lipid vesicles compared to Trp- and DOPC lipid vesicles, we observed that there are not many significant differences in: 1) tryptophan's λ_{max} at 10 minutes after column elution (366 nm in DOCPe compared to 368 nm in DOPC); and 2) the observed shift in λ_{max} between 10 min and 4 hours after elution (3 nm in DOCPe and 2 nm in DOPC). These observations indicate that the inverse head group does increase the tendency of Trp- to partition in the lipid bilayer, but only slightly. This is also in agreement with the data presented in Figure 6.2, where we show that the amount of Trp- partitioning in the lipid bilayer is 3.5 times less than the amount of Trp+ in DOPC, whether it is a DOCPe or DOPC lipid bilayer. The Trp- present at the time of elution from the column must be partitioned in the lipid bilayer, but it is not as deeply partitioned as Trp+. This is indicated by the small shift in λ_{max} between 10 min and 4

hours after elution for Trp- with DOCPe lipids (3 nm) and DOPC lipids (2 nm) compared to the 7 and 12 nm shifts for Trp+, respectively. The similarity of the partition of Trp- in the two membranes is also in agreement with the simulations results discussed next.

6.5 MD SIMULATIONS

Our collaborator, Dr. Alfredo Cardenas, performed MD simulations and computed free energy profiles on the same system that we investigated experimentally. In Figure 6.4, we show the computed free energy profiles (or the potential of mean force) for four different translocation scenarios that include the two different phospholipid membranes (DOPC and DOCPe), the two different charges (positive and negative tryptophan which we denote by Trp+ and Trp-, respectively), and their combinations. The center of the membrane is at $z=0$, which is also expected to be the position with the highest barrier for the permeation of the charged peptides. The solid black line, which describes translocation of the positively charged tryptophan in the inverted membrane, has the highest barrier at the center of the membrane of more than 25 kcal/mol. Conversely, the lowest central barrier for permeation is the same permeant (Trp+) through the biological phospholipid DOPC. Note however that the free energy profile for Trp+ in DOPC includes a minimum at about 14 Å from the membrane center. If the barrier is measured from the bottom of the well the difference between the two membranes is about 7 kcal mol^{-1}. It is also of interest that the difference in permeation between membranes for the Trp- is much smaller, suggesting that retaining the glycerol groups “as are” in the modified phospholipid impact the permeation significantly.

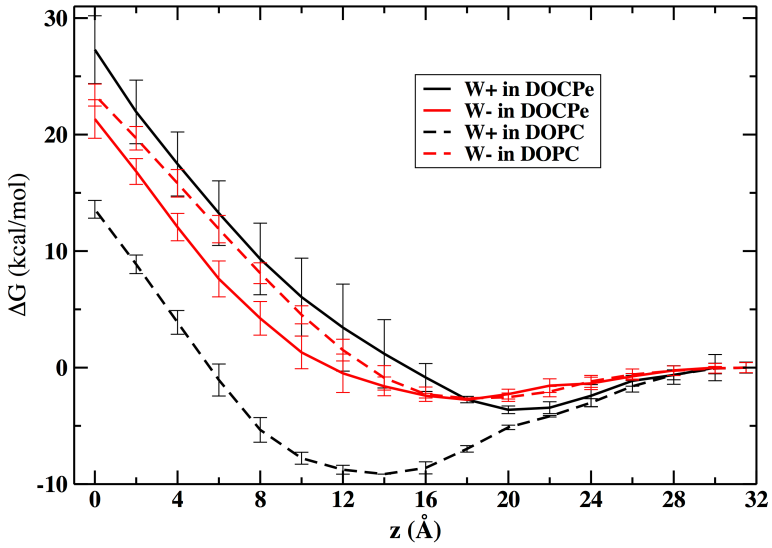

Figure 6.4: Potential of mean force for the permeation of positively (Trp+) and negatively (Trp-) charged tryptophan through a DOCPe membrane (solid lines). For comparison, the results from our previous study with a DOPC membrane are also shown (dashed lines).

The permeation barrier of Trp- in the two membranes is quite similar and is, within the error bars of the simulations, about 2 kcal mol^{-1}. This observation on Trp- suggests that the impact of the phospholipid structure is larger on Trp+ translocation, an observation that is also consistent with the previously discussed experimental findings in Figures 6.2 and 6.3.

Trp+ binds more than Trp- in both membranes with the strongest binding for Trp+ in the DOPC membrane. For the latter, the minimum is located in the glycerol region of the membrane. For the other cases, the minima are located further outside the membrane in the head group region of the bilayer.

We estimated the mean first passage time for penetration of the peptide from the water phase to the membrane center using Eq. (2). The faster time is obtained for Trp+ penetration through DOPC with an estimate of 80 ± 50 h. The times are orders of magnitude larger for the other systems (10^{10}, 10^{6}, and 10^{4} h for Trp+ in DOCPe, and Trp-

in DOPC and DOCPe, respectively). The penetration time ratio (τ(Trp-)/(τ(Trp+)) is about 10^4 for DOPC and 10^{-5} for DOCPe. Therefore, there is an inversion of the preference for complete charge translocation in the membrane with the change from DOPC to DOCPe. However, according to our simulations, a complete permeation should be difficult to detect in any of these systems even for Trp+ in a DOPC membrane. This is since these permeation events require very long times, times that may be longer than the life time of the vesicle.

6.6 DISCUSSION

Results in Figures 6.2-6.4 show significant qualitative agreement between experimental and theoretical investigations of these systems. Both show significant membrane binding of Trp+ when the phospholipid is DOPC, as predicted by the analysis of the mechanism proposed in our previous work.[12] Both simulation and experiment show the weakest binding for Trp- in both DOCPe and DOPC membranes, followed by a slightly stronger binding for Trp+ in the DOCPe. Our experimental results only show surface binding of the charged tryptophan species without membrane crossing. These observations are in agreement with the slow permeation predicted by the simulations.

Given the agreement between experiments and simulations we used the latter to try to understand the differential binding of Trp+ and Trp- in the two membranes.

6.6.1 Bilayer structure and charge distribution explained the observed membrane partition.

Figure 6.5 shows a comparison of the electron density profiles for pure lipid bilayers formed by both DOCPe and DOPC molecules. Figure 6.5a shows that the DOCPe bilayer was denser in the head group/water interface region and less dense at the center of the membrane than the DOPC bilayer. Figure 6.5b shows that the phosphate

distribution in DOCPe was shifted by about 3 Å to the water phase region and it was more spread compared to DOPC. In the inverted lipid membrane, the phosphate groups are increasingly surrounded by water molecules, and therefore are freer to move compared to the DOPC phosphates that are buried deeper in the membrane. The choline distribution is shifted by about 2 Å to the interior of the DOCPe membrane, and is narrower compared to that of the DOPC due to its deeper positioning toward the core. The density distributions for the glycerol groups are similar for both lipids, with slightly less penetration to the interior for the DOCPe membrane.

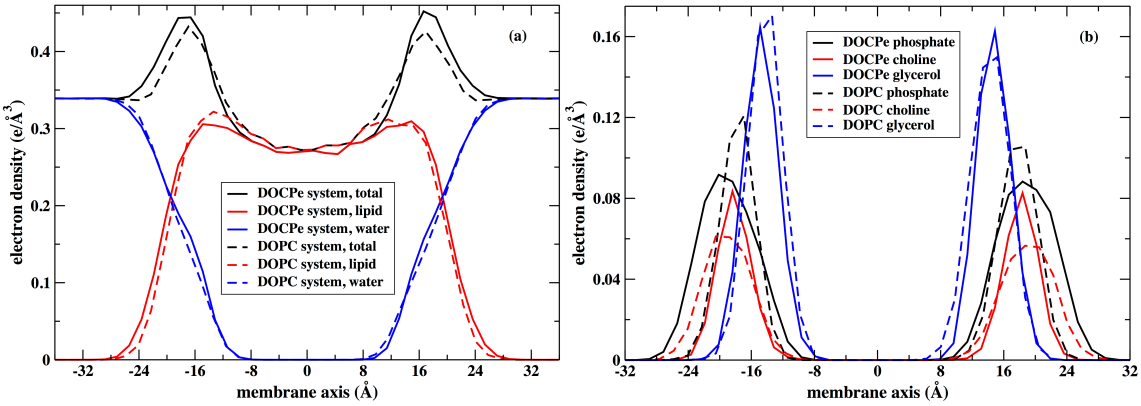

Figure 6.5: Electron density profiles of DOCPe (solid lines) and DOPC (dashed lines) bilayer membranes. They were obtained by averaging the densities of configurations from the last 20 ns of the simulations. Panel (a) shows the total densities of the membranes, along with the individual water and lipid contributions in each case. Panel (b) displays the electron density profiles of the head groups (phosphate and choline) and of the glycerol linkage.

Figure 6.6 displays the charge densities along the membrane axis for the inverted DOCPe and the regular DOPC membranes. The total charge density (panel a) is qualitatively similar for both lipids but the DOCPe membrane shows more prominent peaks and depressions. Panel b demonstrates the inversion of charges due to the exchange of positions of the phosphate and choline groups in the two lipids. However, no such an

inversion occurs for the charge density for glycerol (panel c). The charge density for the glycerol is qualitatively similar for both lipids, showing a positive density on the water side and a negative density inside the membrane (the larger error bars for DOPC indicates that this property did not fully converge in both layers). The charge density of water (panel d) is more complex in the DOCPe membrane, which shows two maxima and one minimum. Conversely the DOPC has only one prominent maximum and one minimum. An explanation at the molecular level for this phenomenon is given in Figure 6.7.

The plot of the orientation of the water dipole with respect to the membrane axis (Figure 6.7a) points to a different and more complex water structure at the DOCPe polar interface compared to the DOPC membrane. For DOPC, the oxygen atoms of the water molecules are located at the interface pointing away from the membrane center. Thus, the water's hydrogen atoms can interact with the phosphate and the glycerol carbonyl oxygen atoms without a change of orientation of the water molecules (Figure 6.7b). In contrast, the plot of the water dipole orientation (Figure 6.7a) shows a positive contribution for DOCPe with the oxygen atoms of the water molecules pointing to the membrane center when they pass the phosphate groups (the hydrogen atoms interacting with the outside phosphate and the oxygen atoms pointing to the positive choline groups). Further penetration inverts this positive contribution when the water's hydrogen atoms point to the membrane center (Figures 6.7 a and c). This variation of water orientations in the DOCPe membrane decreases their influence in driving the insertion of a charged particle deeper inside the membrane. Our observations are similar to those described in Perttu, E. K., et al. and Magarkar, A., et al., but the molecular orientations of water in those previous simulations have additional features, probably due to the larger concentrations of monatomic ions used in those studies.[17-18] Figure 6.7d shows the projections of the P-N vector (the vector from the head group phosphorus to the nitrogen) along the membrane

axis. Interestingly, the distribution for DOCPe is broader, suggesting weaker electrostatic impact on charged insertion compared to the head group in DOPC.

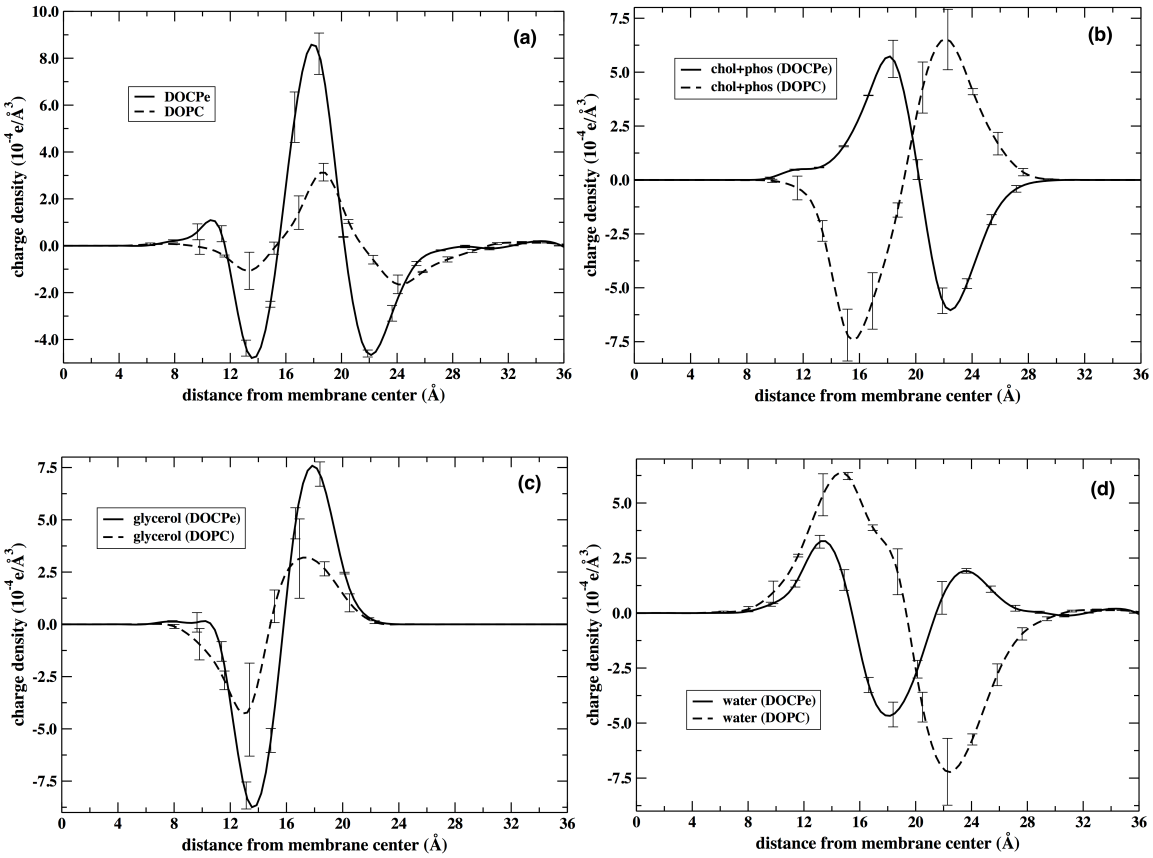

Figure 6.6: The charge density profiles for the DOCPe (solid lines) and DOPC (dashed lines) membranes as a function of the distance from the membrane center, averaged over both leaflets. (a) Total contributions of charges, (b) added contributions of choline and phosphate groups, (c) glycerol and (d) water contributions. Error bars are estimated by computing the charge densities for the two leaflets of the bilayer.

The structural and charge configuration at the head group and glycerol regions in both membranes create an environment that favors the partitioning of Trp+ compared to Trp-. In the case of the DOPC membrane that we considered previously,[12] the presence of two neighboring groups (phosphate and glycerol) that support interaction with Trp+

enhances its membrane partitioning and prevents a deeper insertion of Trp-. In the case of DOCPe, such a synergistic support for a specific charge is attenuated by the less uniform arrangement of membrane charges. In this case, the deeper polar group, glycerol, supports the insertion of Trp+ while its neighboring group, choline, favors interactions with Trp-. Both simulation (Figure 6.4) and experiment (Figure 6.2a) suggest that Trp+ does not reach the glycerol region in DOCPe due to the location of the choline groups, but it only interacts with the external phosphate groups. For Trp-, the similar location of the glycerol groups in both membranes hinders its deeper penetration inside the membrane. Trp- only reaches the head group region in both membranes interacting with the choline groups.

The charge distribution of the DOCPe lipid membrane also modifies the orientational distribution of water molecules, inducing its flip-flop along the membrane axis (Figure 6.7a). This variation, combined with the broader distribution of the P-N dipole vector along the same axis (Figure 6.7d) has the effect of dampening any preference for the partition of a specific charge inside the DOCPe membrane, as we observe in both simulations and experiments.

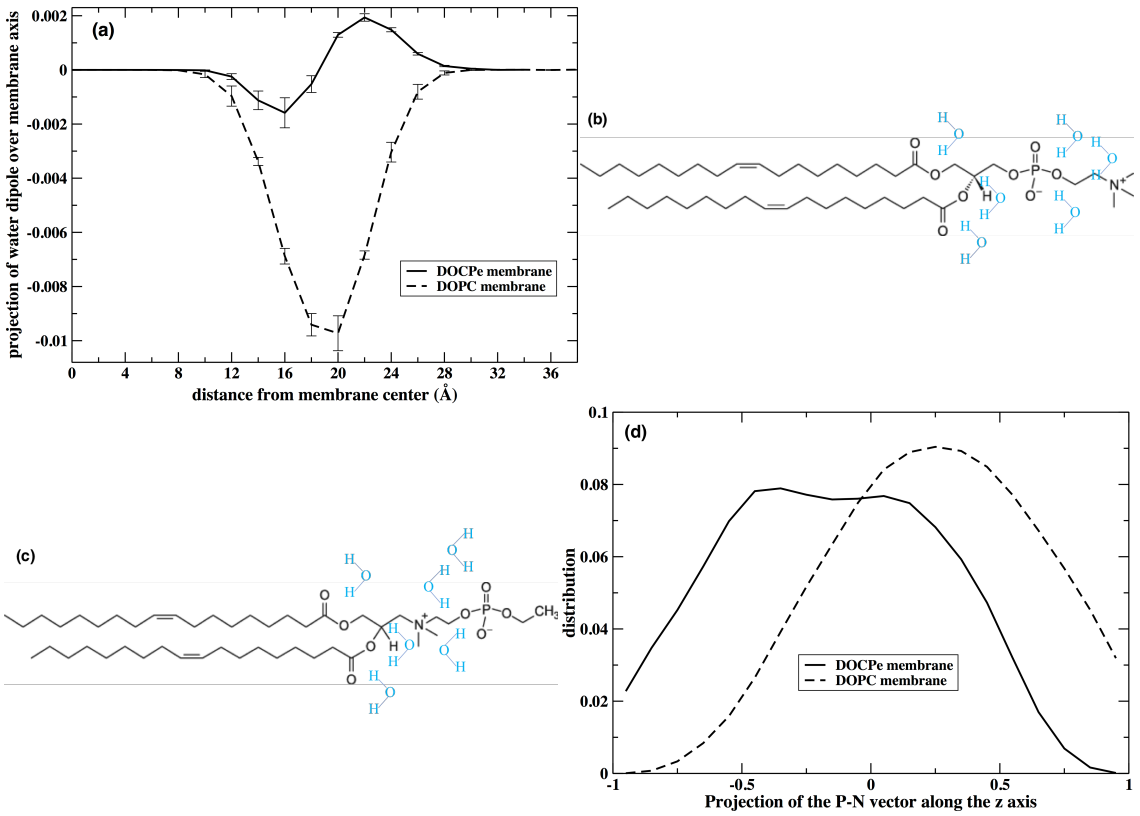

Figure 6.7: (a) The average projection of the water dipole vector along the membrane axis is plotted as a function of the distance of the oxygen water from the membrane center. The projection values are weighted by the normalized population of water molecules along the membrane $P_{water}(z)$, which explains the small values. The sign of the projection indicates the orientation of the oxygen atoms (positive and negative are toward and away from the membrane center, respectively). Cartoon drawings of water molecule orientations in the head group/glycerol region are shown for DOPC (b) and DOCPe (c) membranes. There is a uniform orientation of water in the DOPC membrane, while the orientation changes in the DOCPe membrane. (d) Projection of the P-N vector along the membrane axis for both membranes. The distribution is broader for DOCPe lipids, which decreases the effect of its dipole along the membrane axis.

6.6.2 Why is membrane permeation slow and not observed for these charged species?

Simulations of translocation of charged molecules usually show a high degree of membrane perturbation.[8, 14-15, 20-21] Even the permeation of polar species occurs with

distortion of the bilayer structure of the membrane.[22-24] In the calculations of the PMF (Figure 6.4), large local perturbations are observed when the charged permeants are close to the membrane center (Figure 6.8). The membrane is distorted with some phosphates moving to the membrane interior for Trp+ (Figure 6.8a) and choline groups getting closer to Trp- (Figure 6.8b). To facilitate these interactions of the head groups with the permeant buried inside the membrane's hydrophobic core, the acyl chains need to extend beyond the mid-plane of the membrane and penetrate to the other layer (Figures 6.8 c and d). Deep water insertion is also observed in regions close to the charged terminal of the permeant. These membrane defects and large transversal displacements of lipids are expensive in free energy. An extreme example of membrane distortion is of the flipping of one DOPC lipid from one leaflet to the other which costs about 22 kcal mol^{-1}.[25] When the energy cost is that large, unassisted single charge permeation faces a large barrier and is too slow to be observed. That is the case for the systems considered in this study. Even for the fastest permeant in our simulations, Trp+ permeation through DOPC, the experiment only shows binding of this charge to the membrane. Our simulations also show the strongest binding for this pair.

A recent study of the amino acid sequences of known CPPs showed that efficient permeating peptides have a range of sequence length, charge and amphipathic character.[26] The average median length of residues is 14, and the average peptide charge is +5. They often contain amphipathic or hydrophobic segments. In the case of Trp+, we have a single residue with a single charge (the smallest reported CPP has three residues).[27] The tryptophan side chain gives it some amphipathic character but the size of the indole ring is too small to effectively anchor the charge amino acid deeper at the membrane core. The small size and the corresponding high charge density, and minimal amphipathic properties of Trp+ makes its permeation too slow to be observed

experimentally. For Trp- in DOPC or Trp+ and Trp- in DOCPe, the more unfavorable membrane charge distributions prevent these charges from moving beyond the head group region and make the membrane impermeable to these charges.

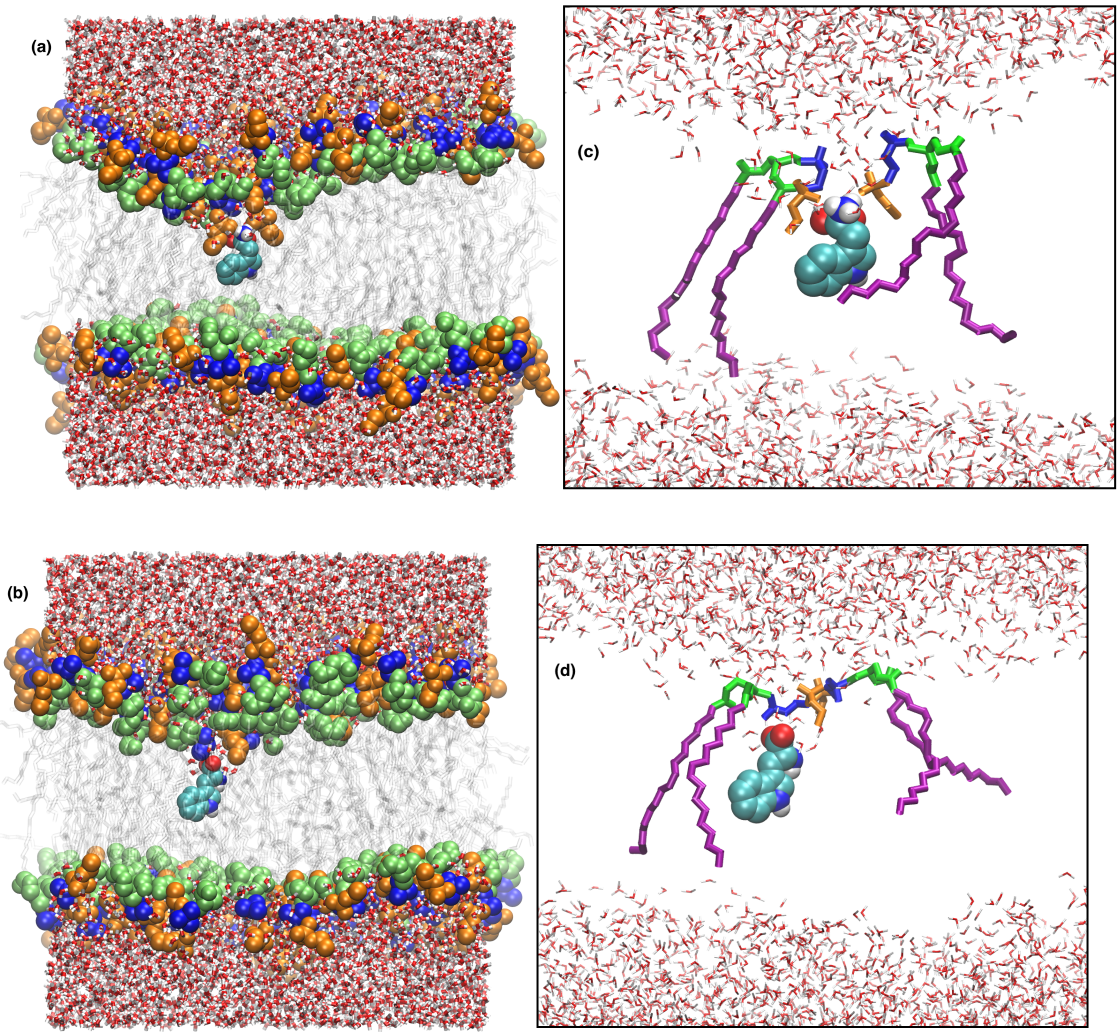

Figure 6.8: Two molecular snapshots extracted from molecular dynamics trajectories when the center of mass of the permeant tryptophan molecule was constrained at the center of the membrane. (a) W+, (b) W-. At panels (a) and (b) we use van der Waals spheres to represent the phosphate (orange), choline (blue), glycerol (green), and charged tryptophan (mostly cyan). Lipids tails are shown as translucent gray lines. Panels (c) and (d) show detailed views of (a) and (b), respectively, displaying the two lipids with head groups closest to the permeant. The color labels are similar to the panels (a) and (b), but the hydrocarbon chains are shown in violet. This figure illustrates the general tendency for large local perturbation (with increased head group and water molecules penetration) when the charged tryptophan is buried in the hydrophobic core of the membrane. The figure indicates that the phospholipid heads are shifted into the middle of the membrane in the presence of a charged permeant at the center.

6.7 CONCLUSION

We present experimental and computational evidence for stronger partitioning of Trp+ than Trp- in both the biological relevant DOPC membrane and its inverted head group counterpart DOCPe membrane. Both experiment and simulation show that the binding of Trp+ to the DOPC is the strongest and it is located at the glycerol region of the membrane, deeper than the preferred partitioning site for Trp+ in DOCPe and for Trp- in both membranes. We explain these results by analyzing the charge distribution of the lipid components in the two membranes that affects also the orientation of water molecules at the membrane interface and the dipole moment in the head group region.

The experimental results show evidence of charge partitioning without permeation. This is also in agreement with our simulations. Permeation times for all cases are too slow to be observed in the corresponding vesicular membranes. We propose that the small size of the charged amino acids (high charge density) and its lack of a large hydrophobic or amphipathic segment, prevents its deeper insertion inside the hydrophobic center with less severe distortions to the structure of the bilayer membrane.

It is expected that the qualitative understanding of this work and our previous work will assist in the design of small peptides with tunable membrane permeation and partitioning capabilities.

6.8 REFERENCES

1. Buch-Pedersen, M. J.; Pedersen, B. P.; Veierskov, B.; Nissen, P.; Palmgren, M. G. Protons and How They are Transported by Proton Pumps. *Pflügers Arch.* **2008,** *457*, 573-579.

2. Vivès, E.; Schmidt, J.; Pèlegrin, A. Cell-Penetrating and Cell-Targeting Peptides in Drug Delivery. *Biochim. Biophys. Acta, Rev. Cancer* **2008,** *1786*, 126-138.

3. Herce, H. D.; Garcia, A. E. Molecular Dynamics Simulations Suggest a Mechanism for Translocation of the Hiv-1 Tat Peptide across Lipid Membranes. *Proc. Natl. Acad. Sci. USA* **2007,** 104, 20805−20810.

4. Pickar, A. D.; Benz, R. Transport of Oppositely Charged Lipophilic Probe Ions in Lipid Bilayer Membranes Having Various Structures. *J. Membr. Biol.* **1978,** *44*, 353-376.

5. Wilson, M. A.; Pohorille, A. Mechanism of Unassisted Ion Transport across Membrane Bilayers. *J. Am. Chem. Soc.* **1996,** *118*, 6580-6587.

6. Tepper, H. L.; Voth, G. A. Mechanisms of Passive Ion Permeation through Lipid Bilayers: Insights from Simulations. *J. Phys. Chem. B* **2006,** *110*, 21327-21337.

7. Khavrutskii, I. V.; Gorfe, A. A.; Lu, B.; McCammon, J. A. Free Energy for the Permeation of Na+ and Cl− Ions and Their Ion-Pair through a Zwitterionic Dimyristoyl Phosphatidylcholine Lipid Bilayer by Umbrella Integration with Harmonic Fourier Beads. *J. Am. Chem. Soc.* **2009,** *131*, 1706-1716.

8. Fathizadeh, A.; Elber, R. Ion Permeation through a Phospholipid Membrane: Transition State, Path Splitting, and Calculation of Permeability. *J. Chem. Theory Comput.* **2019,** *15*, 720-730.

9. Cardenas, A. E.; Shrestha, R.; Webb, L. J.; Elber, R. Membrane Permeation of a Peptide: It Is Better to be Positive. *J. Phys. Chem. B* **2015,** *119*, 6412-6420.

10. Marrink, S. J.; Berendsen, H. J. C. Permeation Process of Small Molecules across Lipid Membranes Studied by Molecular Dynamics Simulations. *J. Phys. Chem.* **1996,** *100*, 16729-16738.

11. Marrink, S.-J.; Berendsen, H. J. C. Simulation of Water Transport Through a Lipid Membrane. *J. Phys. Chem.* **1994,** *98*, 4155-4168.

12. Anderson, C. M.; Cardenas, A.; Elber, R.; Webb, L. J. Preferential Equilibrium Partitioning of Positively Charged Tryptophan into Phosphatidylcholine Bilayer Membranes. *J. Phys. Chem. B* **2019,** *123*, 170-179.

13. Clarke, R. J. The Dipole Potential of Phospholipid Membranes and Methods for its Detection. *Adv. Colloid Interface Sci.* **2001,** *89-90*, 263-281.

14. Li, L.; Vorobyov, I.; Allen, T. W. The Different Interactions of Lysine and Arginine Side Chains with Lipid Membranes. *J. Phys. Chem. B* **2013,** *117*, 11906-11920.

15. Ou, S.; Lucas, T. R.; Zhong, Y.; Bauer, B. A.; Hu, Y.; Patel, S. Free Energetics and the Role of Water in the Permeation of Methyl Guanidinium across the Bilayer–Water Interface: Insights from Molecular Dynamics Simulations Using Charge Equilibration Potentials. *J. Phys. Chem. B* **2013,** *117*, 3578-3592.

16. Bonhenry, D.; Tarek, M.; Dehez, F. Effects of Phospholipid Composition on the Transfer of a Small Cationic Peptide Across a Model Biological Membrane. *J. Chem. Theory Comput.* **2013,** *9*, 5675-5684.

17. Perttu, E. K.; Kohli, A. G.; Szoka, F. C. Inverse-Phosphocholine Lipids: A Remix of a Common Phospholipid. *J. Am. Chem. Soc.* **2012,** *134*, 4485-4488.

18. Magarkar, A.; Róg, T.; Bunker, A. Molecular Dynamics Simulation of Inverse-Phosphocholine Lipids. *J. Phys. Chem. C* **2014,** *118*, 19444-19449.

19. Rezaei Sani, S. M.; Akhavan, M.; Jalili, S. Salt-Induced Effects on Natural and Inverse DPPC Lipid Membranes: Molecular Dynamics Simulation. *Biophys. Chem.* **2018,** *239*, 7-15.

20. Huang, K.; García, Angel E. Free Energy of Translocating an Arginine-Rich Cell-Penetrating Peptide across a Lipid Bilayer Suggests Pore Formation. *Biophys. J.* **2013,** *104*, 412-420.

21. Vorobyov, I.; Olson, T. E.; Kim, J. H.; Koeppe, R. E.; Andersen, O. S.; Allen, T. W. Ion-Induced Defect Permeation of Lipid membranes. *Biophys. J.* **2014,** *106*, 586-597.

22. MacCallum, J. L.; Bennett, W. F. D.; Tieleman, D. P. Distribution of Amino Acids in a Lipid Bilayer from Computer Simulations. *Biophys. J.* **2008,** *94*, 3393-3404.

23. Cardenas, A. E.; Jas, G. S.; DeLeon, K. Y.; Hegefeld, W. A.; Kuczera, K.; Elber, R. Unassisted Transport of N-Acetyl-l-tryptophanamide through Membrane: Experiment and Simulation of Kinetics. *J. Phys. Chem. B* **2012,** *116*, 2739-2750.

24. Wei, C.; Pohorille, A. Sequence-Dependent Interfacial Adsorption and Permeation of Dipeptides across Phospholipid Membranes. *J. Phys. Chem. B* **2017,** *121*, 9859-9867.

25. Sapay, N.; Bennett, W. F. D.; Tieleman, D. P. Thermodynamics of Flip-Flop and Desorption for a Systematic Series of Phosphatidylcholine Lipids. *Soft Matter* **2009,** *5*, 3295-3302.

26. Kauffman, W. B.; Fuselier, T.; He, J.; Wimley, W. C. Mechanism Matters: A Taxonomy of Cell Penetrating Peptides. *Trends Biochem. Sci.* **2015,** *40*, 749-764.

27. Chaudhary, K.; Agrawal, P.; Usmani, S. S.; Singh, S.; Bhalla, S.; Gautam, A.; Raghava, Gajendra P. S. CPPsite 2.0: A Repository of Experimentally Validated Cell-Penetrating Peptides. *Nucleic Acids Res.* **2015,** *44*, D1098-D1103.

Bibliography

1. Cevc, G. Membrane Electrostatics. *Biochim. Biophys. Acta, Rev. Biomembr.* **1990,** *1031*, 311-382.

2. Honig, B. H.; Hubbell, W. L.; Flewelling, R. F. Electrostatic Interactions in Membranes and Proteins. *Annu. Rev. of Biophys. Biophys. Chem.* **1986,** *15*, 163-193.

3. Efimova, S. S.; Ostroumova, O. S. Effect of Dipole Modifiers on the Magnitude of the Dipole Potential of Sterol-Containing Bilayers. *Langmuir* **2012,** *28*, 9908-9914.

4. Haldar, S.; Kanaparthi, R. K.; Samanta, A.; Chattopadhyay, A. Differential Effect of Cholesterol and its Biosynthetic Precursors on Membrane Dipole Potential. *Biophys. J.* **2012,** *102*, 1561-1569.

5. Starke-Peterkovic, T.; Turner, N.; Vitha, M. F.; Waller, M. P.; Hibbs, D. E.; Clarke, R. J. Cholesterol Effect on the Dipole Potential of Lipid Membranes. *Biophys. J.* **2006,** *90*, 4060-70.

6. Schamberger, J.; Clarke, R. J., Hydrophobic Ion Hydration and the Magnitude of the Dipole Potential. *Biophys. J.* **2002,** *82*, 3081-3088.

7. Duffin, R. L.; Garrett, M. P.; Busath, D. D. Modulation of Lipid Bilayer Interfacial Dipole Potential by Phloretin, RH421, and 6-Ketocholestanol as Probed by Gramicidin Channel Conductance. *Langmuir* **2003,** *19*, 3561-3561.

8. Phillips, L. R.; Cole, C. D.; Hendershot, R. J.; Cotten, M.; Cross, T. A.; Busath, D. D. Noncontact Dipole Effects on Channel Permeation. III. Anomalous Proton Conductance Effects in Gramicidin. *Biophys. J.* **1999,** *77*, 2492-2501.

9. Hladky, S. B. The Energy Barriers to Ion Transport by Nonactin Across Thin Lipid Membranes. *Biochim. Biophys. Acta, Biomembr.* **1974,** *352*, 71-85.

10. Bala, S.; Kombrabail, M. H.; Prabhananda, B. S. Effect of Phloretin on Ionophore Mediated Electroneutral Transmembrane Translocations of H+, K+ and Na+ in Phospholipid Vesicles. *Biochim. Biophys. Acta, Biomembr.* **2001,** *1510*, 258-269.

11. Cladera, J.; Martin, I.; Ruysschaert, J.-M.; O'Shea, P. Characterization of the Sequence of Interactions of the Fusion Domain of the Simian Immunodeficiency Virus with Membranes: Role of the Membrane Dipole Potential. *J. Biol. Chem.* **1999,** *274*, 29951-29959.

12. Alakoskela, J. I.; Kinnunen, P. K. Control of a Redox Reaction on Lipid Bilayer Surfaces by Membrane Dipole Potential. *Biophys. J.* **2001,** *80*, 294-304.

13. Maggio, B. Modulation of Phospholipase A2 by Electrostatic Fields and Dipole Potential of Glycosphingolipids in Monolayers. *J. Lipid Res.* **1999,** *40*, 930-939.

14. Alakoskela, J.-M. I.; Söderlund, T.; Holopainen, J. M.; Kinnunen, P. K. J. Dipole Potential and Head-Group Spacing Are Determinants for the Membrane Partitioning of Pregnanolone. *Mol. Pharmacol.* **2004,** *66*, 161-168.

15. Cladera, J.; O'Shea, P. Intramembrane Molecular Dipoles Affect the Membrane Insertion and Folding of a Model Amphiphilic Peptide. *Biophys. J.* **1998,** *74*, 2434-2442.

16. Starke-Peterkovic, T.; Turner, N.; Else, P. L.; Clarke, R. J. Electric Field Strength of Membrane Lipids from Vertebrate Species: Membrane Lipid Composition and Na+-K+-ATPase Molecular Activity. *Am. J. of Physiol. Regul. Integr. Comp. Physiol.* **2005,** *288*, R663-R670.

17. Buzón, V.; Cladera, J. Effect of Cholesterol on the Interaction of the HIV GP41 Fusion Peptide with Model Membranes. Importance of the Membrane Dipole Potential. *Biochemistry* **2006,** *45*, 15768-15775.

18. Shrestha, R.; Cardenas, A. E.; Elber, R.; Webb, L. J. Measurement of the Membrane Dipole Electric Field in DMPC Vesicles Using Vibrational Shifts of p-Cyanophenylalanine and Molecular Dynamics Simulations. *J. Phys. Chem. B* **2015,** *119*, 2869-2876.

19. Hu, W.; Webb, L. J. Direct Measurement of the Membrane Dipole Field in Bicelles Using Vibrational Stark Effect Spectroscopy. *J. Phys. Chem. Lett.* **2011,** *2*, 1925-1930.

20. Fried, S. D.; Boxer, S. G. Measuring Electric Fields and Noncovalent Interactions Using the Vibrational Stark Effect. *Acc. Chem. Res.* **2015,** *48*, 998-1006.

21. Chattopadhyay, A.; Boxer, S. G. Vibrational Stark Effect Spectroscopy. *J. Am. Chem. Soc.* **1995,** *117*, 1449-1450.

22. Park, E. S.; Andrews, S. S.; Hu, R. B.; Boxer, S. G. Vibrational Stark Spectroscopy in Proteins: A Probe and Calibration for Electrostatic Fields. *J. Phys. Chem. B* **1999,** *103*, 9813-9817.

23. Andrews, S. S.; Boxer, S. G. Vibrational Stark Effects of Nitriles I. Methods and Experimental Results. *J. Phys. Chem. A* **2000,** *104*, 11853-11863.

24. Andrews, S. S.; Boxer, S. G. Vibrational Stark Effects of Nitriles II. Physical Origins of Stark Effects from Experiment and Perturbation Models. *J. Phys. Chem. A* **2002,** *106*, 469-477.

25. Yesylevskyy, S.; Marrink, S.-J.; Mark, A. E. Alternative Mechanisms for the Interaction of the Cell-Penetrating Peptides Penetratin and the TAT Peptide with Lipid Bilayers. *Biophys. J.* **2009,** *97*, 40-49.

26. Vivès, E.; Schmidt, J.; Pèlegrin, A. Cell-penetrating and Cell-Targeting Peptides in Drug Delivery. *Biochim. Biophys. Acta, Rev. Cancer* **2008,** *1786*, 126-138.

27. Huang, K.; García, Angel E. Free Energy of Translocating an Arginine-Rich Cell-Penetrating Peptide across a Lipid Bilayer Suggests Pore Formation. *Biophys. J.* **2013,** *104*, 412-420.

28. Herce, H. D.; Garcia, A. E.; Litt, J.; Kane, R. S.; Martin, P.; Enrique, N.; Rebolledo, A.; Milesi, V. Arginine-Rich Peptides Destabilize the Plasma Membrane, Consistent with a Pore Formation Translocation Mechanism of Cell-Penetrating Peptides. *Biophys. J.* **2009,** *97*, 1917-1925.

29. Herce, H. D.; Garcia, A. E. Cell Penetrating Peptides: How Do They Do It? *J. Biol. Phys.* **2007,** *33*, 345-356.

30. Ciobanasu, C.; Siebrasse, J. P.; Kubitscheck, U. Cell-Penetrating HIV1 TAT Peptides Can Generate Pores in Model Membranes. *Biophys. J.* **2010,** *99*, 153-162.

31. Vivian, J. T.; Callis, P. R. Mechanisms of Tryptophan Fluorescence Shifts in Proteins. *Biophys. J.* **2001,** *80*, 2093-2109.

32. Gable, J. E.; Schlamadinger, D. E.; Cogen, A. L.; Gallo, R. L.; Kim, J. E. Fluorescence and UV Resonance Raman Study of Peptide-Vesicle Interactions of Human Cathelicidin LL-37 and its F6W and F17W Mutants. *Biochemistry* **2009,** *48*, 11264-11272.

33. Lakowicz, J. R. *Principles of Fluorescence Spectroscopy*; Springer: New York, 2006; pp 205-235.

34. Lakowicz, J. R. *Principles of Fluorescence Spectroscopy*; Springer: New York, 2006; pp 331-351.

35. Pfefferkorn, C. M.; Walker, R. L.; He, Y.; Gruschus, J. M.; Lee, J. C. Tryptophan Probes Reveal Residue-Specific Phospholipid Interactions of Apolipoprotein C-III. *Biochim. Biophys. Acta, Biomembr.* **2015,** *1848*, 2821-2828.

36. Soni, Smita P.; Adu-Gyamfi, E.; Yong, Sylvia S.; Jee, Clara S.; Stahelin, Robert V. The Ebola Virus Matrix Protein Deeply Penetrates the Plasma Membrane: An Important Step in Viral Egress. *Biophys. J.* **2013,** *104*, 1940-1949.

37. Mishra, V. K.; Palgunachari, M. N. Interaction of Model Class A1, Class A2, and Class Y Amphipathic Helical Peptides with Membranes. *Biochemistry* **1996,** *35*, 11210-11220.

38. Bystrov, V. F. S., Y. E.; Viktorov, A. V.; Barsukov, L. I.; Bergelson, L. D. 31P-NMR Signals From Inner and Outer Surfaces of Phospholipid Membranes. *FEBS Lett.* **1972,** *25*, 337-338.

39. Fröhlich, M.; Brecht, V.; Peschka-Süss, R. Parameters Influencing the Determination of Liposome Lamellarity by 31P-NMR. *Chem. Phys. Lipids* **2001,** *109*, 103-112.

40. Kim, B.-K.; Boika, A.; Kim, J.; Dick, J. E.; Bard, A. J. Characterizing Emulsions by Observation of Single Droplet Collisions—Attoliter Electrochemical Reactors. *J. Am. Chem. Soc.* **2014,** *136*, 4849-4852.

41. Dick, J. E.; Renault, C.; Kim, B.-K.; Bard, A. J. Electrogenerated Chemiluminescence of Common Organic Luminophores in Water Using an Emulsion System. *J. Am. Chem. Soc.* **2014,** *136*, 13546-13549.

42. Dick, J. E.; Renault, C.; Kim, B.-K.; Bard, A. J. Simultaneous Detection of Single Attoliter Droplet Collisions by Electrochemical and Electrogenerated Chemiluminescent Responses. *Angew. Chem., Int. Ed.* **2014,** *53*, 11859-11862.

43. Kim, B.-K.; Kim, J.; Bard, A. J. Electrochemistry of a Single Attoliter Emulsion Droplet in Collisions. *J. Am. Chem. Soc.* **2015,** *137*, 2343-2349.

44. Cheng, W.; Compton, R. G. Oxygen Reduction Mediated by Single Nanodroplets Containing Attomoles of Vitamin B12: Electrocatalytic Nano-Impacts Method. *Angew. Chem., Int. Ed.* **2015,** *54*, 7082-7085.

45. Cheng, W.; Compton, R. G. Investigation of Single-Drug-Encapsulating Liposomes Using the Nano-Impact Method. *Angew. Chem., Int. Ed.* **2014,** *53*, 13928-13930.

46. Dunevall, J.; Fathali, H.; Najafinobar, N.; Lovric, J.; Wigström, J.; Cans, A.-S.; Ewing, A. G. Characterizing the Catecholamine Content of Single Mammalian Vesicles by Collision–Adsorption Events at an Electrode. *J. Am. Chem. Soc.* **2015,** *137*, 4344-4346.

47. Dick, J. E.; Hilterbrand, A. T.; Boika, A.; Upton, J. W.; Bard, A. J. Electrochemical Detection of a Single Cytomegalovirus at an Ultramicroelectrode and Its Antibody Anchoring. *Proc. Natl. Acad. Sci. U. S. A.* **2015,** *112*, 5303.

48. Toh, H. S.; Compton, R. G. Electrochemical Detection of Single Micelles Through 'Nano-Impacts'. *Chemical Science* **2015,** *6*, 5053-5058.

49. Dick, J. E.; Renault, C.; Bard, A. J. Observation of Single-Protein and DNA Macromolecule Collisions on Ultramicroelectrodes. *J. Am. Chem. Soc.* **2015,** *137*, 8376-8379.

50. Keller, C. A.; Kasemo, B. Surface Specific Kinetics of Lipid Vesicle Adsorption Measured with a Quartz Crystal Microbalance. *Biophys. J.* **1998,** *75*, 1397-1402.

51. Dimitrievski, K.; Kasemo, B. Simulations of Lipid Vesicle Adsorption for Different Lipid Mixtures. *Langmuir* **2008,** *24*, 4077-4091.

52. Hellberg, D.; Scholz, F.; Schauer, F.; Weitschies, W. Bursting and Spreading of Liposomes on the Surface of a Static Mercury Drop Electrode. *Electrochem. Commun.* **2002,** *4*, 305-309.

53. Hellberg, D.; Scholz, F.; Schubert, F.; Lovrić, M.; Omanović, D.; Hernández, V. A.; Thede, R. Kinetics of Liposome Adhesion on a Mercury Electrode. *J. Phys. Chem. B* **2005,** *109*, 14715-14726.

54. Agmo Hernández, V.; Scholz, F. Kinetics of the Adhesion of DMPC Liposomes on a Mercury Electrode. Effect of Lamellarity, Phase Composition, Size and Curvature of Liposomes, and Presence of the Pore Forming Peptide Mastoparan X. *Langmuir* **2006,** *22*, 10723-10731.

55. Agmo Hernández, V.; Niessen, J.; Harnisch, F.; Block, S.; Greinacher, A.; Kroemer, H. K.; Helm, C. A.; Scholz, F. The Adhesion and Spreading of Thrombocyte Vesicles on Electrode Surfaces. *Bioelectrochemistry* **2008,** *74*, 210-216.

56. Kannuck, R. M.; Bellama, J. M.; Durst, R. A. Measurement of Liposome-Released Ferrocyanide by a Dual-Function Polymer Modified Electrode. *Anal. Chem.* **1988,** *60*, 142-147.

57. Young, R. C.; Feldberg, S. W. Photoinitiated Mediated Transport of H3O+ and/or OH- Across Glycerol Monooleate Bilayers Doped with Magnesium Octaethylporphyrin. *Biophys. J.* **1979,** *27*, 237-255.

58. Feldberg, S. W.; Armen, G. H.; Bell, J. A.; Chang, C. K.; Wang, C. B. Electron Transport Across Glycerol Monooleate Bilayer Lipid Membranes Facilitated by Magnesium Etiochlorin. *Biophys. J.* **1981,** *34*, 149-163.

59. Koley, D.; Bard, A. J. Triton X-100 Concentration Effects on Membrane Permeability of a Single HeLa Cell by Scanning Electrochemical Microscopy (SECM). *Proc. Natl. Acad. Sci. U. S. A.* **2010,** *107*, 16783.

60. Fontaine, P.; Fauré, M. C.; Muller, F.; Poujade, M.; Micha, J.-S.; Rieutord, F.; Goldmann, M. Unexpected Stability of Phospholipid Langmuir Monolayers Deposited on Triton X-100 Aqueous Solutions. *Langmuir* **2007,** *23*, 12959-12965.

61. le Maire, M.; Champeil, P.; Møller, J. V. Interaction of Membrane Proteins and Lipids with Solubilizing Detergents. *Biochim. Biophys. Acta, Biomembr.* **2000,** *1508*, 86-111.

62. Gennuso, F.; Fernetti, C.; Tirolo, C.; Testa, N.; Episcopo, F.; Caniglia, S.; Morale, M. C.; Ostrow, J. D.; Pascolo, L.; Tiribelli, C.; Marchetti, B. Bilirubin Protects Astrocytes from its own Toxicity by Inducing Up-Regulation and Translocation of Multidrug Resistance-Associated Protein 1 (Mrp1). *Proc. Natl. Acad. Sci. U. S. A.* **2004,** *101*, 2470.

63. Lanyi, J. K. Influence of Electron Transport on the Interaction Between Membrane Lipids and Triton X-100 in Halobacterium Cutirubrum. *Biochemistry* **1973,** *12*, 1433-1438.

64. Kim, J.; Izadyar, A.; Nioradze, N.; Amemiya, S. Nanoscale Mechanism of Molecular Transport through the Nuclear Pore Complex As Studied by Scanning Electrochemical Microscopy. *J. Am. Chem. Soc.* **2013,** *135*, 2321-2329.

65. Kim, J.; Kim, B.-K.; Cho, S. K.; Bard, A. J. Tunneling Ultramicroelectrode: Nanoelectrodes and Nanoparticle Collisions. *J. Am. Chem. Soc.* **2014,** *136*, 8173-8176.

66. Kwon, S. J.; Zhou, H.; Fan, F.-R. F.; Vorobyev, V.; Zhang, B.; Bard, A. J. Stochastic Electrochemistry with Electrocatalytic Nanoparticles at Inert Ultramicroelectrodes—Theory and Experiments. *Phys. Chem. Chem. Phys.* **2011,** *13*, 5394-5402.

67. Boika, A.; Thorgaard, S. N.; Bard, A. J. Monitoring the Electrophoretic Migration and Adsorption of Single Insulating Nanoparticles at Ultramicroelectrodes. *J. Phys. Chem. B* **2013,** *117*, 4371-4380.

68. Einstein, A. Über die von der molekularkinetischen Theorie der Wärme geforderte Bewegung von in ruhenden Flüssigkeiten suspendierten Teilchen. *Ann. Phys.* **1905,** *322*, 549.

69. Kučerka, N.; Kiselev, M. A.; Balgavý, P. Determination of Bilayer Thickness and Lipid Surface Area in Unilamellar Dimyristoylphosphatidylcholine Vesicles from Small-Angle Neutron Scattering Curves: A Comparison of Evaluation Methods. *Eur. Biophys. J.* **2004,** *33*, 328-334.

70. Efimova, S. S.; Ostroumova, O. S. Effect of Dipole Modifiers on the Magnitude of the Dipole Potential of Sterol-Containing Bilayers. *Langmuir* **2012,** *28*, 9908-9914.

71. Haldar, S.; Kanaparthi, R. K.; Samanta, A.; Chattopadhyay, A. Differential Effect of Cholesterol and its Biosynthetic Precursors on Membrane Dipole Potential. *Biophys. J.* **2012,** *102*, 1561-1569.

72. Starke-Peterkovic, T.; Turner, N.; Vitha, M. F.; Waller, M. P.; Hibbs, D. E.; Clarke, R. J. Cholesterol Effect on the Dipole Potential of Lipid Membranes. *Biophys. J.* **2006,** *90*, 4060-4070.

73. Szabo, G. Dual Mechanism for the Action of Cholesterol on Membrane Permeability. *Nature* **1974,** *252*, 47-49.

74. Hofsäss, C.; Lindahl, E.; Edholm, O. Molecular Dynamics Simulations of Phospholipid Bilayers with Cholesterol. *Biophys. J.* **2003,** *84*, 2192-2206.

75. Chiu, S. W.; Jakobsson, E.; Scott, H. L. Combined Monte Carlo and Molecular Dynamics Simulation of Hydrated Dipalmitoyl–Phosphatidylcholine–Cholesterol Lipid Bilayers. *J. Chem. Phys.* **2001,** *114*, 5435-5443.

76. Smondyrev, A. M.; Berkowitz, M. L. Structure of Dipalmitoylphosphatidylcholine/Cholesterol Bilayer at Low and High Cholesterol Concentrations: Molecular Dynamics Simulation. *Biophys. J.* **1999,** *77*, 2075-2089.

77. Gabdoulline, R. R.; Vanderkooi, G.; Zheng, C. Comparison of the Structures of Dimyristoylphosphatidylcholine in the Presence and Absence of Cholesterol by Molecular Dynamics Simulations. *J. Phys. Chem.* **1996,** *100*, 15942-15946.

78. McIntosh, T. J.; Magid, A. D.; Simon, S. A. Cholesterol Modifies the Short-Range Repulsive Interactions Between Phosphatidylcholine Membranes. *Biochemistry* **1989,** *28*, 17-25.

79. Yang, Y.; Mayer, K. M.; Wickremasinghe, N. S.; Hafner, J. H. Probing the Lipid Membrane Dipole Potential by Atomic Force Microscopy. *Biophys. J.* **2008,** *95*, 5193-5199.

80. Franklin, J. C.; Cafiso, D. S. Internal Electrostatic Potentials in Bilayers: Measuring and Controlling Dipole Potentials in Lipid Vesicles. *Biophys. J.* **1993,** *65*, 289-299.

81. Gross, E.; Bedlack, R. S., Jr.; Loew, L. M. Dual-Wavelength Ratiometric Fluorescence Measurement of the Membrane Dipole Potential. *Biophys. J.* **1994,** *67*, 208-216.

82. Smondyrev, A. M.; Berkowitz, M. L. Effects of Oxygenated Sterol on Phospholipid Bilayer Properties: A Molecular Dynamics Simulation. *Chem. Phys. Lipids* **2001,** *112*, 31-39.

83. Hu, W.; Webb, L. J. Direct Measurement of the Membrane Dipole Field in Bicelles Using Vibrational Stark Effect Spectroscopy. *J. Phys. Chem. Lett.* **2011,** *2*, 1925-1930.

84. Shrestha, R.; Cardenas, A. E.; Elber, R.; Webb, L. J. Measurement of the Membrane Dipole Electric Field in DMPC Vesicles Using Vibrational Shifts of p-Cyanophenylalanine and Molecular Dynamics Simulations. *J. Phys. Chem. B* **2015,** *119*, 2869-2876.

85. Andrews, S. S.; Boxer, S. G. Vibrational Stark Effects of Nitriles I. Methods and Experimental Results. *J. Phys. Chem. A* **2000,** *104*, 11853-11863.

86. Andrews, S. S.; Boxer, S. G. Vibrational Stark Effects of Nitriles II. Physical Origins of Stark Effects from Experiment and Perturbation Models. *J. Phys. Chem. A* **2002,** *106*, 469-477.

87. Johansson, A. C. V.; Lindahl, E. Amino-Acid Solvation Structure in Transmembrane Helices from Molecular Dynamics Simulations. *Biophys. J.* **2006,** *91*, 4450-4463.

88. Duffin, R. L.; Garrett, M. P.; Busath, D. D. Modulation of Lipid Bilayer Interfacial Dipole Potential by Phloretin, RH421, and 6-Ketocholestanol as Probed by Gramicidin Channel Conductance. *Langmuir* **2003,** *19*, 3561-3561.

89. Simon, S. A.; McIntosh, T. J.; Magid, A. D.; Needham, D. Modulation of the Interbilayer Hydration Pressure by the Addition of Dipoles at the Hydrocarbon/Water Interface. *Biophys. J.* **1992,** *61*, 786-799.

90. Honig, B. H.; Hubbell, W. L.; Flewelling, R. F. Electrostatic Interactions in Membranes and Proteins. *Annu. Rev. Biophys. Biophys. Chem.* **1986,** *15*, 163-193.

91. Cevc, G. Membrane Electrostatics. *Biochim. Biophys. Acta, Rev. Biomembr.* **1990,** *1031*, 311-382.

92. Kučerka, N.; Nieh, M.-P.; Katsaras, J. Fluid Phase Lipid Areas and Bilayer Thicknesses of Commonly Used Phosphatidylcholines as a Function of Temperature. *Biochim. Biophys. Acta, Biomembr.* **2011,** *1808*, 2761-2771.

93. Khelashvili, G.; Pabst, G.; Harries, D. Cholesterol Orientation and Tilt Modulus in DMPC Bilayers. *J. Phys. Chem. B* **2010,** *114*, 7524-7534.

94. Róg, T.; Pasenkiewicz-Gierula, M. Cholesterol Effects on the Phosphatidylcholine Bilayer Nonpolar Region: A Molecular Simulation Study. *Biophys. J.* **2001,** *81*, 2190-2202.

95. Jedlovszky, P.; Mezei, M. Effect of Cholesterol on the Properties of Phospholipid Membranes. 1. Structural Features. *J. Phys. Chem. B* **2003,** *107*, 5311-5321.

96. Henriksen, J.; Rowat, A. C.; Brief, E.; Hsueh, Y. W.; Thewalt, J. L.; Zuckermann, M. J.; Ipsen, J. H. Universal Behavior of Membranes with Sterols. *Biophys. J.* **2006,** *90*, 1639-1649.

97. Smaby, J. M.; Momsen, M. M.; Brockman, H. L.; Brown, R. E. Phosphatidylcholine Acyl Unsaturation Modulates the Decrease in Interfacial Elasticity Induced by Cholesterol. *Biophys. J.* **1997,** *73*, 1492-1505.

98. Marsh, D. An Interacting Spin Label Study of Lateral Expansion in Dipalmitoyllecithin-Cholesterol Bilayers. *Biochim. Biophys. Acta, Biomembr.* **1974,** *363*, 373-386.

99. Kusumi, A.; Tsuda, M.; Akino, T.; Ohnishi, S.; Terayama, Y. Protein-Phospholipid-Cholesterol Interaction in the Photolysis of Invertebrate Rhodopsin. *Biochemistry* **1983,** *22*, 1165-1170.

100. Mouritsen, O. G.; Jørgensen, K. Dynamical Order and Disorder in Lipid Bilayers. *Chem. Phys. Lipids* **1994,** *73*, 3-25.

101. McConnell, H. M.; Radhakrishnan, A. Condensed Complexes of Cholesterol and Phospholipids. *Biochim. Biophys. Acta, Biomembr.* **2003,** *1610*, 159-173.

102. Rheinstädter, M. C.; Mouritsen, O. G. Small-Scale Structure in Fluid Cholesterol–Lipid Bilayers. *Curr. Opin. Colloid Interface Sci.* **2013,** *18*, 440-447.

103. Buzón, V.; Cladera, J. Effect of Cholesterol on the Interaction of the HIV GP41 Fusion Peptide with Model Membranes. Importance of the Membrane Dipole Potential. *Biochemistry* **2006,** *45*, 15768-15775.

104. Auner, B. G.; O'Neill, M. A.; Valenta, C.; Hadgraft, J. Interaction of Phloretin and 6-Ketocholestanol with DPPC-Liposomes as Phospholipid Model Membranes. *Int. J. Pharm.* **2005,** *294*, 149-155.

105. Deamer, D.; Kuzina S.I.; Mikhailov, A. I.; Maslikova, E. I.; Seleznev, S. A. Origin of Amphiphilic Molecules and Their Role in Primary Structure Formation. *J. Evol. Biochem. Physiol.* **1991,** *27*, 212-217.

106. Deamer, D. W., Role of Amphiphilic Compounds in the Evolution of Membrane Structure on the Early Earth. *Orig. Life Evol. Biosph.* **1986,** *17*, 3-25.

107. Morowitz, H. J.; Heinz, B.; Deamer, D. W. The Chemical Logic of a Minimum Protocell. *Orig. Life Evol. Biosph.* **1988,** *18*, 281-287.

108. Pohorille, A.; Deamer, D. Self-Assembly and Function of Primitive Cell Membranes. *Res. Microbiol.* **2009,** *160*, 449-456.

109. Yang, N. J.; Hinner, M. J. Getting Across the Cell Membrane: An Overview for Small Molecules, Peptides, and Proteins. *Methods Microbiol.* **2015,** *1266*, 29-53.

110. Lipinski, C. A.; Lombardo, F.; Dominy, B. W.; Feeney, P. J., Experimental and Computational Approaches to Estimate Solubility and Permeability in Drug Discovery and Development Settings. *Adv. Drug Delivery Rev.* **1997,** *23*, 3-25.

111. Veber, D. F.; Johnson, S. R.; Cheng, H.-Y.; Smith, B. R.; Ward, K. W.; Kopple, K. D. Molecular Properties That Influence the Oral Bioavailability of Drug Candidates. *J. Med. Chem.* **2002,** *45*, 2615-2623.

112. Guimarães, C. R. W.; Mathiowetz, A. M.; Shalaeva, M.; Goetz, G.; Liras, S. Use of 3D Properties to Characterize Beyond Rule-of-5 Property Space for Passive Permeation. *J. Chem. Inf. Model.* **2012,** *52*, 882-890.

113. Al-Awqati, Q. One Hundred Years of Membrane Permeability: Does Overton Still Rule? *Nat. Cell Biol.* **1999,** *1*, 201-202.

114. Li, L.; Vorobyov, I.; Allen, T. W. The Different Interactions of Lysine and Arginine Side Chains with Lipid Membranes. *J. Phys. Chem. B* **2013,** *117*, 11906-11920.

115. Bemporad, D.; Luttmann, C.; Essex, J. W. Computer Simulation of Small Molecule Permeation across a Lipid Bilayer: Dependence on Bilayer Properties and Solute Volume, Size, and Cross-Sectional Area. *Biophys. J.* **2004,** *87*, 1-13.

116. Chakrabarti, A. C.; Deamer, D. W. Permeability of Lipid Bilayers to Amino Acids and Phosphate. *Biochim. Biophys. Acta, Biomembr.* **1992,** *1111*, 171-177.

117. Wimley, W. C.; White, S. H. Experimentally Determined Hydrophobicity Scale for Proteins at Membrane Interfaces. *Nat. Struct. Biol.* **1996,** *3*, 842.

118. MacCallum, J. L.; Bennett, W. F. D.; Tieleman, D. P. Partitioning of Amino Acid Side Chains into Lipid Bilayers: Results from Computer Simulations and Comparison to Experiment. *J. Gen. Physiol.* **2007,** *129*, 371.

119. Chakrabarti, A. C. Permeability of Membranes to Amino Acids and Modified Amino Acids: Mechanisms Involved in Translocation. *Amino Acids* **1994,** *6*, 213-229.

120. Yesylevskyy, S.; Marrink, S.-J.; Mark, A. E. Alternative Mechanisms for the Interaction of the Cell-Penetrating Peptides Penetratin and the TAT Peptide with Lipid Bilayers. *Biophys. J.* **2009,** *97*, 40-49.

121. Vivès, E.; Schmidt, J.; Pèlegrin, A. Cell-Penetrating and Cell-Targeting Peptides in Drug Delivery. *Biochim. Biophys. Acta, Rev. Cancer* **2008,** *1786*, 126-138.

122. Huang, K.; García, Angel E. Free Energy of Translocating an Arginine-Rich Cell-Penetrating Peptide across a Lipid Bilayer Suggests Pore Formation. *Biophys. J.* **2013,** *104*, 412-420.

123. Herce, H. D.; Garcia, A. E.; Litt, J.; Kane, R. S.; Martin, P.; Enrique, N.; Rebolledo, A.; Milesi, V. Arginine-Rich Peptides Destabilize the Plasma Membrane, Consistent with a Pore Formation Translocation Mechanism of Cell-Penetrating Peptides. *Biophys. J.* **2009,** *97*, 1917-1925.

124. Herce, H. D.; Garcia, A. E. Cell Penetrating Peptides: How Do They Do It? *J. Biol. Phys.* **2007,** *33*, 345-356.

125. Cardenas, A. E.; Shrestha, R.; Webb, L. J.; Elber, R., Membrane Permeation of a Peptide: It is Better to be Positive. *J. Phys. Chem. B* **2015,** *119*, 6412-20.

126. White, S. H.; Wimley, W. C. Membrane Protein Folding and Stability: Physical Principles. *Annu. Rev. Biophys. Biomol. Struct.* **1999,** *28*, 319-365.

127. Killian, J. A.; von Heijne, G. How Proteins Adapt to a Membrane–Water Interface. *Trends Biochem. Sci.* **2000,** *25*, 429-434.

128. Yau, W.-M.; Wimley, W. C.; Gawrisch, K.; White, S. H. The Preference of Tryptophan for Membrane Interfaces. *Biochemistry* **1998,** *37*, 14713-14718.

129. Sanchez, Katheryn M.; Kang, G.; Wu, B.; Kim, Judy E. Tryptophan-Lipid Interactions in Membrane Protein Folding Probed by Ultraviolet Resonance Raman and Fluorescence Spectroscopy. *Biophys. J.* **2011,** *100*, 2121-2130.

130. Granseth, E.; von Heijne, G.; Elofsson, A. A study of the Membrane-Water Interface Region of Membrane Proteins. *J. Mol. Biol.* **2005,** *346*, 377-85.

131. Landolt-Marticorena, C.; Williams, K. A.; Deber, C. M.; Reithmeier, R. A. F. Non-random Distribution of Amino Acids in the Transmembrane Segments of Human Type I Single Span Membrane Proteins. *J. Mol. Biol.* **1993,** *229*, 602-608.

132. Chamberlain, A. K.; Lee, Y.; Kim, S.; Bowie, J. U. Snorkeling Preferences Foster an Amino Acid Composition Bias in Transmembrane Helices. *J. Mol. Biol.* **2004,** *339*, 471-479.

133. Arkin, I. T.; Brunger, A. T. Statistical Analysis of Predicted Transmembrane α-Helices. *Biochim. Biophys. Acta, Protein Struct. Mol. Enzymol.* **1998,** *1429*, 113-128.

134. Jobin, M.-L.; Blanchet, M.; Henry, S.; Chaignepain, S.; Manigand, C.; Castano, S.; Lecomte, S.; Burlina, F.; Sagan, S.; Alves, I. D. The Role of Tryptophans on the Cellular Uptake and Membrane Interaction of Arginine-Rich Cell Penetrating Peptides. *Biochim. Biophys. Acta, Biomembr.* **2015,** *1848*, 593-602.

135. de Jesus, A. J.; Allen, T. W. The Role of Tryptophan Side Chains in Membrane Protein Anchoring and Hydrophobic Mismatch. *Biochim. Biophys. Acta, Biomembr.* **2013,** *1828*, 864-876.

136. Ulmschneider, J. P.; Andersson, M.; Ulmschneider, M. B. Determining Peptide Partitioning Properties via Computer Simulation. *J. Membr. Biol.* **2011,** *239*, 15-26.

137. Ulmschneider, M. B.; Sansom, M. S. P. Amino Acid Distributions in Integral Membrane Protein Structures. *Biochim. Biophys. Acta, Biomembr.* **2001,** *1512*, 1-14.

138. Arseniev A. S.; Barsukov, I. L.; Bystrov, V. F.; Lomize, A. L.; Ovchinnikov Y. A. 1H-NMR Study of Gramicidin A Transmembrane Ion Channel. Head-to-head Right-handed, Single-stranded Helices. *FEBS Lett.* **1985,** *186*, 168-184.

139. Cowan, S. W.; Schirmer, T.; Rummel, G.; Steiert, M.; Ghosh, R.; Pauptit, R. A.; Jansonius, J. N.; Rosenbusch, J. P. Crystal Structures Explain Functional Properties of Two E. Coli Porins. *Nature* **1992,** *358*, 727.

140. Deisenhofer, J.; Michel, H. The Photosynthetic Reaction Centre From the Purple Bacterium Rhodopseudomonas viridis. *EMBO J.* **1989,** *8*, 2149-2170.

141. *Probing Membrane Protein Structure and Dynamics by Fluorescence Spectroscopy. Encyclopedia of Analytical Chemistry [Online];* Wiley & Sons, https://onlinelibrary.wiley.com/doi/abs/10.1002/9780470027318.a9353 (accessed Aug 1, 2018).

142. Lakowicz, J. R. *Principles of Fluorescence Spectroscopy*; Springer: New York, 2006; pp 205-235.

143. Vivian, J. T.; Callis, P. R. Mechanisms of Tryptophan Fluorescence Shifts in Proteins. *Biophys. J.* **2001,** *80*, 2093-2109.

144. Valeur, B.; Weber, G. Resolution of the Fluorescence Excitation Spectrum of Indole into the 1La and 1Lb Excitation Bands. *Photochem. Photobiol.* **1977,** *25*, 441-444.

145. Soni, Smita P.; Adu-Gyamfi, E.; Yong, Sylvia S.; Jee, Clara S.; Stahelin, Robert V. The Ebola Virus Matrix Protein Deeply Penetrates the Plasma Membrane: An Important Step in Viral Egress. *Biophys. J.* **2013,** *104*, 1940-1949.

146. Pfefferkorn, C. M.; Walker, R. L.; He, Y.; Gruschus, J. M.; Lee, J. C. Tryptophan Probes Reveal Residue-Specific Phospholipid Interactions of Apolipoprotein C-III. *Biochim. Biophys. Acta* **2015,** *1848*, 2821-2828.

147. Gable, J. E.; Schlamadinger, D. E.; Cogen, A. L.; Gallo, R. L.; Kim, J. E. Fluorescence and UV Resonance Raman Study of Peptide-Vesicle Interactions of Human Cathelicidin LL-37 and its F6W and F17W Mutants. *Biochemistry* **2009,** *48*, 11264-11272.

148. Lakowicz, J. R. *Principles of Fluorescence Spectroscopy*; Springer: New York, 2006; pp 331-351.

149. Liu, L.-P.; Deber, C. M. Anionic Phospholipids Modulate Peptide Insertion into Membranes. *Biochemistry* **1997,** *36*, 5476-5482.

150. Mishra, V. K.; Palgunachari, M. N. Interaction of Model Class A1, Class A2, and Class Y Amphipathic Helical Peptides with Membranes. *Biochemistry* **1996,** *35*, 11210-11220.

151. Macdo, Z. S.; Furquim, T. A.; Ito, A. S. Estimation of Average Depth of Penetration of Melanotropins in Dimyristoylphosphatidylglycerol Vesicles. *Biophys. Chem.* **1996,** *59*, 193-202.

152. Lewis, R. N. A. H.; McElhaney, R. N. Fourier Transform Infrared Spectroscopy in the Study of Lipid Phase Transitions in Model and Biological Membranes: Practical Considerations. In *Methods in Membrane Lipids*, Dopico, A. M., Ed. Humana Press: NJ, 2007; pp 207-227.

153. Buch-Pedersen, M. J.; Pedersen, B. P.; Veierskov, B.; Nissen, P.; Palmgren, M. G. Protons and How They are Transported by Proton Pumps. *Pflügers Arch.* **2008,** *457*, 573-579.

154. Vivès, E.; Schmidt, J.; Pèlegrin, A. Cell-Penetrating and Cell-Targeting Peptides in Drug Delivery. *Biochim. Biophys. Acta, Rev. Cancer* **2008,** *1786*, 126-138.

155. Herce, H. D.; Garcia, A. E. Molecular Dynamics Simulations Suggest a Mechanism for Translocation of the Hiv-1 Tat Peptide across Lipid Membranes. *Proc. Natl. Acad. Sci. USA* **2007,** 104, 20805−20810.

156. Pickar, A. D.; Benz, R. Transport of Oppositely Charged Lipophilic Probe Ions in Lipid Bilayer Membranes Having Various Structures. *J. Membr. Biol.* **1978,** *44*, 353-376.

157. Wilson, M. A.; Pohorille, A. Mechanism of Unassisted Ion Transport across Membrane Bilayers. *J. Am. Chem. Soc.* **1996,** *118*, 6580-6587.

158. Tepper, H. L.; Voth, G. A. Mechanisms of Passive Ion Permeation through Lipid Bilayers: Insights from Simulations. *J. Phys. Chem. B* **2006,** *110*, 21327-21337.

159. Khavrutskii, I. V.; Gorfe, A. A.; Lu, B.; McCammon, J. A. Free Energy for the Permeation of Na+ and Cl− Ions and Their Ion-Pair through a Zwitterionic Dimyristoyl Phosphatidylcholine Lipid Bilayer by Umbrella Integration with Harmonic Fourier Beads. *J. Am. Chem. Soc.* **2009,** *131*, 1706-1716.

160. Fathizadeh, A.; Elber, R. Ion Permeation through a Phospholipid Membrane: Transition State, Path Splitting, and Calculation of Permeability. *J. Chem. Theory Comput.* **2019,** *15*, 720-730.

161. Cardenas, A. E.; Shrestha, R.; Webb, L. J.; Elber, R. Membrane Permeation of a Peptide: It Is Better to be Positive. *J. Phys. Chem. B* **2015,** *119*, 6412-6420.

162. Marrink, S. J.; Berendsen, H. J. C. Permeation Process of Small Molecules across Lipid Membranes Studied by Molecular Dynamics Simulations. *J. Phys. Chem.* **1996,** *100*, 16729-16738.

163. Marrink, S.-J.; Berendsen, H. J. C. Simulation of Water Transport Through a Lipid Membrane. *J. Phys. Chem.* **1994,** *98*, 4155-4168.

164. Anderson, C. M.; Cardenas, A.; Elber, R.; Webb, L. J. Preferential Equilibrium Partitioning of Positively Charged Tryptophan into Phosphatidylcholine Bilayer Membranes. *J. Phys. Chem. B* **2019,** *123*, 170-179.

165. Clarke, R. J. The Dipole Potential of Phospholipid Membranes and Methods for its Detection. *Adv. Colloid Interface Sci.* **2001,** *89-90*, 263-281.

166. Li, L.; Vorobyov, I.; Allen, T. W. The Different Interactions of Lysine and Arginine Side Chains with Lipid Membranes. *J. Phys. Chem. B* **2013,** *117*, 11906-11920.

167. Ou, S.; Lucas, T. R.; Zhong, Y.; Bauer, B. A.; Hu, Y.; Patel, S. Free Energetics and the Role of Water in the Permeation of Methyl Guanidinium across the Bilayer–Water Interface: Insights from Molecular Dynamics Simulations Using Charge Equilibration Potentials. *J. Phys. Chem. B* **2013,** *117*, 3578-3592.

168. Bonhenry, D.; Tarek, M.; Dehez, F. Effects of Phospholipid Composition on the Transfer of a Small Cationic Peptide Across a Model Biological Membrane. *J. Chem. Theory Comput.* **2013,** *9*, 5675-5684.

169. Perttu, E. K.; Kohli, A. G.; Szoka, F. C. Inverse-Phosphocholine Lipids: A Remix of a Common Phospholipid. *J. Am. Chem. Soc.* **2012,** *134*, 4485-4488.

170. Magarkar, A.; Róg, T.; Bunker, A. Molecular Dynamics Simulation of Inverse-Phosphocholine Lipids. *J. Phys. Chem. C* **2014,** *118*, 19444-19449.

171. Rezaei Sani, S. M.; Akhavan, M.; Jalili, S. Salt-Induced Effects on Natural and Inverse DPPC Lipid Membranes: Molecular Dynamics Simulation. *Biophys. Chem.* **2018,** *239*, 7-15.

172. Huang, K.; García, Angel E. Free Energy of Translocating an Arginine-Rich Cell-Penetrating Peptide across a Lipid Bilayer Suggests Pore Formation. *Biophys. J.* **2013,** *104*, 412-420.

173. Vorobyov, I.; Olson, T. E.; Kim, J. H.; Koeppe, R. E.; Andersen, O. S.; Allen, T. W. Ion-Induced Defect Permeation of Lipid membranes. *Biophys. J.* **2014,** *106*, 586-597.

174. MacCallum, J. L.; Bennett, W. F. D.; Tieleman, D. P. Distribution of Amino Acids in a Lipid Bilayer from Computer Simulations. *Biophys. J.* **2008,** *94*, 3393-3404.

175. Cardenas, A. E.; Jas, G. S.; DeLeon, K. Y.; Hegefeld, W. A.; Kuczera, K.; Elber, R. Unassisted Transport of N-Acetyl-l-tryptophanamide through Membrane: Experiment and Simulation of Kinetics. *J. Phys. Chem. B* **2012,** *116*, 2739-2750.

176. Wei, C.; Pohorille, A. Sequence-Dependent Interfacial Adsorption and Permeation of Dipeptides across Phospholipid Membranes. *J. Phys. Chem. B* **2017,** *121*, 9859-9867.

177. Sapay, N.; Bennett, W. F. D.; Tieleman, D. P. Thermodynamics of Flip-Flop and Desorption for a Systematic Series of Phosphatidylcholine Lipids. *Soft Matter* **2009,** *5*, 3295-3302.

178. Kauffman, W. B.; Fuselier, T.; He, J.; Wimley, W. C. Mechanism Matters: A Taxonomy of Cell Penetrating Peptides. *Trends Biochem. Sci.* **2015,** *40*, 749-764.

179. Chaudhary, K.; Agrawal, P.; Usmani, S. S.; Singh, S.; Bhalla, S.; Gautam, A.; Raghava, Gajendra P. S. CPPsite 2.0: A Repository of Experimentally Validated Cell-Penetrating Peptides. *Nucleic Acids Res.* **2015,** *44*, D1098-D1103.

Vita

Cari Michelle Anderson was born in Austin, TX and grew up in Pennsylvania. She graduated from North Penn High School in Lansdale, PA. She then completed her Bachelors of Science in Chemistry at Iona College, where she also played softball for the Iona College Gaels. Following her undergraduate career in 2013, she started graduate school at The University of Texas at Austin and worked under Dr. Lauren J. Webb.

Permanent email: carianderson.2345@gmail.com

This dissertation was typed by Cari Michelle Anderson.